Hydrogen isotopes transport in liquid metals under steady state plasma bombardment

BI HAILIN

Doctor of Philosophy

Department of Fusion Science
School of Physical Sciences
SOKENDAI (The Graduate University for Advanced Studies)

Hydrogen isotopes transport in liquid metals under steady state plasma bombardment

BI HAILIN

Doctor of Philosophy

Supervisor: Prof. Yoshi Hirooka

Department of Fusion Science

School of Physical Sciences

The Graduate University for Advanced Studies

(SOKENDAI)

2017

Contents

Abstract

It has been widely recognized that solid plasma-facing components (PFCs) would suffer from erosion and cracking when they are subjected to high power loads and particle fluxes in fusion devices. As a possible solution, the use of liquid metals for PFCs has been proposed because of their self-cooling and self-healing properties. At present, lithium, tin and gallium are the possible candidates. The liquid lithium covered divertor was tested in NSTX, and a continuously flowing liquid lithium limiter with a loop was performed in EAST, both of which have resulted in improved plasma performance. Free-falling liquid gallium drops have been tested on the T–3 M and ISTTOK tokamaks, where no severe effects on the main plasma parameters have been observed. In this PhD thesis research, one of the technical issues related to hydrogen isotopes transport in liquid metals has been studied extensively.

The understanding of hydrogen isotopes properties in liquid metals is essential for studying particle control in the edge plasma. And to evaluate liquid metals as the PFCs in a fusion reactor, the interactions between plasma and liquid metals should be studied experimentally. However, the information on this subject is far from adequate. This PhD thesis research is intended to provide the understanding of the mechanism of hydrogen transport in liquid metals under plasma bombardment, and to establish a database on hydrogen transport parameters such as diffusivity, recombination coefficient, solubility and retention for liquid metals, and to investigate the natural and forced convection effects, if any, on the hydrogen transport behavior in liquid metals.

To evaluate hydrogen isotopes transport parameters in liquid metals, plasma-driven permeation(PDP) experiments have been conducted in a steady state laboratory-scale linear plasma device: VEHICLE-1. In the PDP experiments, the hydrogen permeation flux is measured by a quadrupole mass spectrometer (QMS) in the downstream side. The electron temperature is typically T_e~3eV and the plasma density is n~$10^{16}m^{-3}$. The particle bombarding flux is Γ~$10^{20}m^{-2}s^{-1}$, and the bombarding energy is controlled by a negative bias voltage applied on the target. An innovative technique employing surface tension to hold a liquid metal using a mesh sheet has been proposed and implemented in

the PDP experiments. A liquid metal sample is fixed in such a way that the upstream surface is exposed to hydrogen plasma, while the downstream side is exposed to an ultrahigh vacuum (10^{-6}-10^{-5} Pa) chamber. Using this technique, the upstream chamber and downstream chamber are separated by the liquid metal on the mesh. A resistive heater is set beneath the mesh sheet to control the temperature of the liquid metal. The melting point of GaInSn alloy is 10.5°C, which means that it is a liquid at room temperature. In the present work, this alloy is chosen as a surrogate for gallium, tin and lithium.

For lithium, hydrogen and deuterium PDP experiments through a 2mm deep lithium membrane have been conducted from 323^{o}C to 402^{o}C, and steady state PDP fluxes have been obtained. From the H-Li phase diagram, it is derived that lithium would transform from α_{liq} phase to $\alpha_{liq}+\beta_{sol}$ phase during PDP. And the dissolved hydrogen concentration remains unchanged even after passing the phase boundary C_s. As a result, the hydrogen and deuterium recombination coefficient for lithium has been obtained for the first time. For GaInSn, hydrogen PDP experiments have been conducted with 2 mm deep GaInSn from 330°C to 437 °C. Deuterium PDP experiments have been conducted with 2 mm and 4 mm deep GaInSn from 280°C to 496 °C. The PDP data show depth effects, suggesting that hydrogen isotopes PDP through liquid GaInSn are diffusion-limited. Hydrogen and deuterium diffusivity and recombination coefficient have been successfully measured for GaInSn. Deuterium retention in GaInSn after PDP has been measured by (thermal desorption spectrometer) TDS. A one-dimension diffusion code: DIFFUSE has been utilized to simulate the experiments by using the measured parameters. The modeling results are consistent with the experimental data. Using the same method for GaInSn, hydrogen isotopes diffusivity and recombinantion coefficient for pure liquid Ga and Sn have been obtained. The deuterium dynamic and static retentions for liquid Ga and Sn have also been evaluated and compared.

Natural convection is a phenomenon commonly present in liquids under thermal expansion induced density variation. In order to investigate natural convection effects on hydrogen PDP, two cases (A, B) of experiment have been prepared in VEHICLE-1. For Case A, the depth of liquid GaInSn is 15mm, and natural convection is supposed to take place judged from the Rayleigh number; For the Case B, a convection preventing

mesh(CPM) is set in the middle of the liquid GaInSn to reduce the effective depth of the liquid, and natural convection is not supposed to take place. The natural convection motion and particle transport behavior for both cases have been simulated with a finite element analysis software COMSOL by solving the Navier-Stokes equations, heat transfer equation, and mass balance equations. The simulation results predict that natural convection only takes place for case a, and particle transport is much faster under natural convection. Deuterium PDP experiments have been conducted for both cases. In Case A, the deuterium permeation flux rapidly increases to a quasi-steady state level as the plasma bombardment starts. In Case B, the permeation flux gradually increases to a steady state level, which is about one order of magnitude lower than that in Case A. The different PDP behavior in these two cases indicates that deuterium permeation through the liquid can be intensely enhanced by the natural convection.

JxB-forced convection effects on hydrogen isotopes recycling have been investigated. From the study of the natural convection effect, it has been found that convection could enhance particle transport and heat transfer in a liquid. However, natural convection may not take place in a liquid divertor situation, where the liquid is warmer at the top. To get actively controlled convection in a liquid divetor, JxB-forced convection has been proposed by M. Shimada et al. In this concept, electrodes are immersed in the liquid and DC currents are applied among the electrodes. Taking advantage of the toroidal magnetic field, a JxB-force could be produced to convect the liquid. In our work, this concept has been demonstrated with a mini JxB setup installed in VEHICLE-1 by using liquid GaInSn. Liquid GaInSn is put in a stainless steel cup with an inner diameter of 50mm. The depth of the liquid metal is set to 13mm. A central electrode made of stainless steel is isolated from the sidewall by a ceramic ring. DC currents (0-100A) are applied between the central electrode and the sidewall. A “water wheel” made of stainless steel is installed on the central electrode as an indicator for the motion of the liquid metal during plasma operation. And visible spectroscopy measurements are performed, taking the intensity of the Hα (Dα) signal as the indication of hydrogen (deuterium) recycling from the liquid metal. Simulations of particle transport in the liquid metal under JxB-forced convection have been performed by COMSOL. The modeling results indicate that particle transport in liquid under JxB-forced convection is much faster than that in static liquid. And with

higher DC currents, more particles are retained in the liquid with less particle recycling from the liquid. In the experiments, it has been found that the flow speed of the liquid increases as the DC currents increases. And hydrogen (deuterium) recycling is reduced when the JxB-force is applied in the liquid. Liquid flow speed effects on the recycling have also been observed, which are in agreement with the simulation results.

This PhD thesis work has established some fundamental knowledge database for the applications of liquid metals as plasma facing components. Using forced convection in the liquid to enhance the particle transport and heat transfer can be a possible idea for the engineering design. Using the hydrogen transport parameters, it is possible to calculate hydrogen isotopes dynamic retention in the liquid PFCs, and hydrogen isotopes recycling flux back to the edge plasma. More efforts are still required to investigate hydrogen isotopes transport behavior in liquid metals under reactor relevant conditions. Experimental proof of enhanced heat transfer by convection also warrants further investigation.

Acknowledgement

Foremost, I would like to express my sincere gratitude to my supervisor Prof. Yoshi Hirooka, for his insightful guidance in the past three years. I am deeply grateful to have the opportunity to learn from him. I will cherish all the moments we worked together and all the fun we had together.

My deeply grateful also goes to Dr. Naoko Ashikawa and Dr. Juro Yagi, for their guidance and supports on my experiments.

I want to express my gratitude to the rest of my thesis committee: Prof. Byron Peterson, Prof. Michiya Shimada, Prof. Yousuke Nakashima, and Prof. Teruya Tanaka for their insightful comments, suggestions and questions, which are extremely important to improve my thesis.

I am very grateful to Prof. Takeo Muroga, Prof. Akio Sagara, Prof. Izumi Murakami, Prof. Junichi Miyazawa, Prof. Nagato Yanagi, Prof. Nagato Yanagi, Prof. Masahiro Kobayashi, Prof. Daiji Kato and Ms. Shihomi Kato for their helps and caring during my study in the National Institute for Fusion Science.

A special thanks goes to Prof. Jiansheng Hu, for his encouragements and supports for this oversea PhD study.

I would like to express my deeply gratitude to my friends, Yue Xue, Haishan Zhou, Hongming Zhang, Shuyu Dai, Haiying Fu, Shaofei Geng, Hao Wang, Xiang Ji, Gaowei Zhang, Yang Liu, Jie Huang, Bo Huang, Xiaodi Du, Xianli Huang, Neng Pu, Theerasarn Pianpanit, Botz Huang, Ippei Watanabe, Junki Morimoto, Norihiro Ikemoto and Gaku Yamazaki, for their encouragements and helps. The wonderful time with you in Japan will be a precious memory in my life.

I dedicate this thesis to

my parents and my wife, Bei.

I love you all.

Chapter 1 Introduction

1.1. Nuclear fusion

Nuclear fusion is a reaction in which atomic nuclei with lower mass collide to form a new type of atomic nucleus, accompanied by a release or absorption of energy. The primary energy source for stars is hydrogen fusion, which is also considered to be one of the most promising candidate options to provide safe, environmentally friendly and economical energy for human beings [1-3]. Of all the possible fusion reactions the deuterium-tritium (D-T) reaction is the most attractive one because tritium and deuterium can react at relatively low energy, generating α-particle (He), neutron (n) and a huge amount of energy [1]:

$$ {}_{1}^{2}\mathrm{D} + {}_{1}^{3}\mathrm{T} \rightarrow {}_{2}^{4}\mathrm{He}\,(3.5\,\mathrm{MeV}) + {}_{0}^{1}\mathrm{n}\,(14.1\,\mathrm{MeV}), \tag{1.1} $$

where the energies shown are kinetic energies of the reaction products. In a fusion plasma, the energy carried by the α-particle can be transferred to the plasma by collision so that the confined plasma can be persistently heated. Lawson [4] showed that a fusion plasma would burn to self-sustaining (ignition) if the product of energy confinement time τ_E [s] and plasma density n [m^{-3}] exceeded a given threshold for a fixed plasma temperature T [keV]. Because τ_E itself is a function of temperature, the ignition condition is more usually expressed as:

$$ n \cdot T \cdot \tau_{\mathrm{E}} > \sim 5 \times 10^{21}\ \mathrm{m}^{-3} \cdot \mathrm{keV} \cdot \mathrm{s}, \tag{1.2} $$

i.e., to achieve ignition, the high-temperature, high-density plasma must be confined in a relatively long time. In a star, the plasma is confined by the force of gravity due to the huge amount of matter. On the earth, two leading ideas are proposed to obtain usable energy from fusion reactions: magnetic confinement fusion (MCF) and inertial confinement fusion (ICF).

In MCF systems, the plasma is held by magnetic field in desired configurations. The core plasma density is kept at ~10^{20} m^{-3} for several seconds of confinement time to fulfill

Eq. (1.2). From 1950's, various ideas of MCF have been proposed, among which tokamaks and stellarators are considered to be the most promising concepts to yield commercial fusion reactors. Many large or medium size MCF devices have been built, e.g., JET [5], JT-60[6], LHD [7], DIII-D [8], ASDEX-U [9], EAST [10], KSTAR [11] and QUEST [12]. Shown in Fig.1.1 is the International Thermonuclear Experimental Reactor (ITER) [13], which is under construction in Cadarache, France. ITER is planned to be the first experimental reactor to demonstrate extended burning of D-T plasmas at a few hundred MWs of fusion power and technology essential to a reactor in an integrated system, and to test nuclear components required to utilize fusion energy for practical purposes [14].

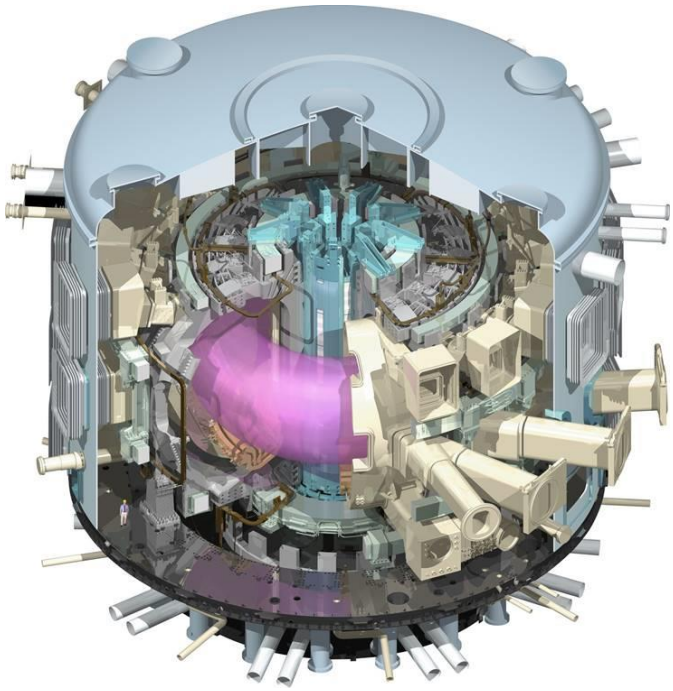

Figure 1.1 Design of ITER tokamak [13].

The MCF device beyond ITER will aim to demonstrate electricity production (DEMO reactor). SlimCS [15], PPCS-A to PPCS-D [16] and ARIES-AT [17] are several examples for tokamak type DEMO concepts. Stellarator type reactor concepts have also been proposed, for example the Force-Free Helical Reactor (FFHR) series concepts being developed by National Institute for Fusion Science in Japan [18]. Recently, some researchers suggested that a test reactor between ITER and DEMO may be necessary in

the roadmap to the realization of fusion energy. These concepts include the China Fusion Engineering Test Reactor (CFETR) [19] and the Fusion Nuclear Science Facility (FNSF) [20], which aim to provide an integrated, continuous fusion nuclear environment that can be used to investigate plasma material interactions, tritium fuel management, and power extraction, etc [20].

In contrast to MCF, ICF goes a different way to fulfill the Lawson Criterion. Fuel targets containing a mixture of deuterium and tritium are heated and compressed by high-energy laser lights or laser-produced X-rays to generate high temperature, high density plasmas. For the ICF plasmas, the density is usually larger than ~10^{31} m^{-3} while the confinement time is shorter than 10^{-10} s [21]. At present, the largest and most energetic ICF device built is the National Ignition Facility (NIF) located at the Lawrence Livermore National Laboratory in Livermore, USA [22]. Recently a fuel capsule gave off more energy than was applied to it in NIF, which is an important milestone towards commercialization of ICF [23].

Overall, considerable progress has been achieved for both MCF and ICF in the last 50 years, but a lot of physics and technical issues are still needed to be addressed to realize fusion energy as a power source. This thesis mainly makes a contribution to the MCF research in the areas of plasma-wall interaction.

1.2 Plasma-wall interaction

1.2.1 The plasma sheath

For a plasma in contact with a solid surface, the electron thermal velocity is larger than that of the ions by the square root of the mass ratio. At the interface between the solid and the plasma, a thin net-charge layer called the Debye sheath develops spontaneously. The electric field in this sheath equalises the electron and ion flows by decreasing the electron flow and enhancing the ion flow. And the plasma flow velocity to the surface is around the sound speed. The most important practical consequence of the formation of a sheath is that it mediates the flow of particles and energy out of the plasma to the solid surface. The width of the Debye sheath is several Debye lengths. The Debye length λ_D is given [1]:

$$\lambda_D = \left(\frac{\varepsilon_0 T}{ne^2}\right)^{1/2}$$
$$= 2.35 \times 10^5 \left(\frac{T}{n}\right)^{1/2} \text{ m}, \quad T \text{ in keV}. \tag{1.3}$$

where n is the plasma density and T is the plasma temperature. Following the Debye sheath, a small electric field, the presheath, extends more deeply into the plasma. Shown in Figure 1.2 is the spatial variation of electric potential, ion velocity, and the ion and electron densities.

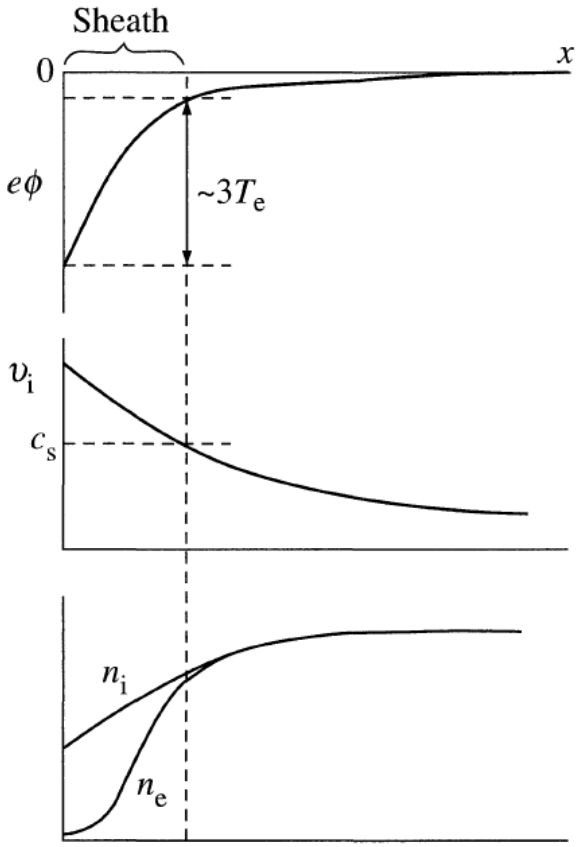

Figure 1.2 Typical spatial variation of the electric potential, ion velocity and the ion and electron densities across the plasma sheath [1].

The electric potential is described by Poisson's equation [1]:

$$\frac{\mathrm{d}^2\phi}{\mathrm{d}x^2} = \frac{e}{\varepsilon_\mathrm{o}}(n_e - n_\mathrm{i}) \tag{1.4}$$

where n_e and n_i are the electron and ion densities. Defining the potential to be zero at the sheath edge the electrons take up a Boltzmann distribution given by:

$$n_e = n_\mathrm{o} \exp \frac{e\phi}{T_\mathrm{e}} \tag{1.5}$$

$$n_\mathrm{i} = n_\mathrm{o} \left(\frac{\frac{1}{2} m_i v_\mathrm{o}^2}{\frac{1}{2} m_i v_\mathrm{o}^2 - e\phi} \right)^{1/2} \tag{1.6}$$

where v_0 is the velocity with which the ions enter the sheath; n_0 is the plasma density outside the sheath. The particle flux density Γ to a surface is given by [1]:

$$\Gamma = n_0 v_0 \approx \tfrac{1}{2} n_0 [k(T_e + T_i)/m_i]^{1/2} \tag{1.7}$$

Where T_e is the eletron temperature; T_i is the ion temperature; n_0 is the plasma density.

The power flux from the plasma to the surface is determined by the thermal energy of the ions and electrons, and the energy due to the acceleration/deceleration of ions/electrons in the sheath. For ions reaching the surface, their energy distribution is very approximately an accelerated and truncated Maxwellian. For electrons reaching the surface, their energy distribution remains Maxwellian but with a reduced density. The energy of ions or electrons transported to a surface by a Maxwellian distribution is *2T* per particle. Thus the total power flux from the plasma to the surface, *P*, is given by [1]:

$$P = n_\mathrm{e} c_\mathrm{s} T_\mathrm{e} \left[\frac{2T_\mathrm{i}}{T_\mathrm{e}} + \frac{2}{1-\delta} + \frac{1}{2} \ln \left(\frac{(1-\delta)^2 m_\mathrm{i}/m_\mathrm{e}}{2\pi(1 + T_\mathrm{i}/T_\mathrm{e})} \right) \right] \tag{1.8}$$

Conveniently, Eq.1.8 can be written：

$$\mathrm{P} = \gamma \Gamma T_e \tag{1.9}$$

where Γ is the ion flux density and γ is the sheath power transmission factor [24]:

$$\gamma \approx \frac{2.5T_i}{T_e} + \frac{2}{1-\delta_e} - 0.5\ln\left[\left(2\pi\frac{m_e}{m_i}\right)\left(1+\frac{T_i}{T_e}\right)(1-\delta_e)^{-2}\right] \tag{1.10}$$

The sheath heat transmission coefficient γ has been plotted as a function of T_i/T_e [24].

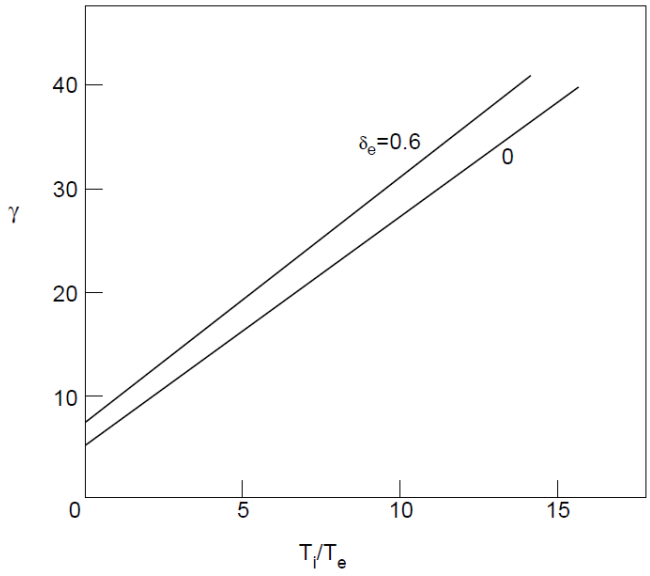

Figure 1.3 The sheath heat transmission coefficient γ as a function of T_i/T_e and secondary emission coefficient δ_e for D^+ ions [24].

1.2.2 The scrape-off layer (SOL) and divertor

For plasma in a magnetic fusion device, it is confined within a restricted volume, with the boundary determined by the Last Closed Flux Surface (LCFS). The shape of the LCFS is determined by the magnetic field due to external conductors and by currents flowing in the plasma. The position of the last closed flux surface may be interrupted by a solid surface, which is called a limiter. Alternatively, the shape of the LCFS may be determined entirely by the magnetic fields, so that the plasma flows towards and eventually interacts with a solid surface far away from the core plasma. This is the basic geometry of a divertor. Shown in Fig.1.4 is a schematic diagram of the cross section of a tokamak with the limiter configuration and the divertor configuration. For the limiter configuration, the plasma comes in contact with a solid surface, which is close to the plasma, and consequently neutral impurity atoms released from the surface can enter

directly in the confined plasma. While for the divertor configuration, the plasma surface interactions are remote from the confined plasma [1].

The particles impact on the surface can cause erosion by sputtering, desorption, and other mechanisms. The particle flow to the surface is primarily due to diffusion from the plasma core into the boundary region or to ionization of neutrals in the boundary plasma. In the boundary layer, as shown in Fig.1.4, the plasma flows along the scrape-off layer and then interacts with the solid surface. Some crossfield transport to the wall, due to turbulence, also occurs. Ions incident on these surfaces may then be neutralized and backscattered or released in other ways to re-enter the plasma. This process is known as recycling. In addition, the flux of plasma particles and radiation may release gas which was previously adsorbed on the surface. When a neutral atom from the surface arrives in the plasma, it is excited and ionized by collisions with electrons.

Next step burning plasma experiments, such as ITER, will have larger steady power and particle fluxes onto divertor and main-chamber surfaces. Together with the longer pulses, this can cause a significantly larger erosion of these components than in present experiments both during steady-state plasma conditions and, particularly, during edge localized modes (ELMs) and disruptions. These critical technical issues, will affect the successful development of magnetic fusion energy.

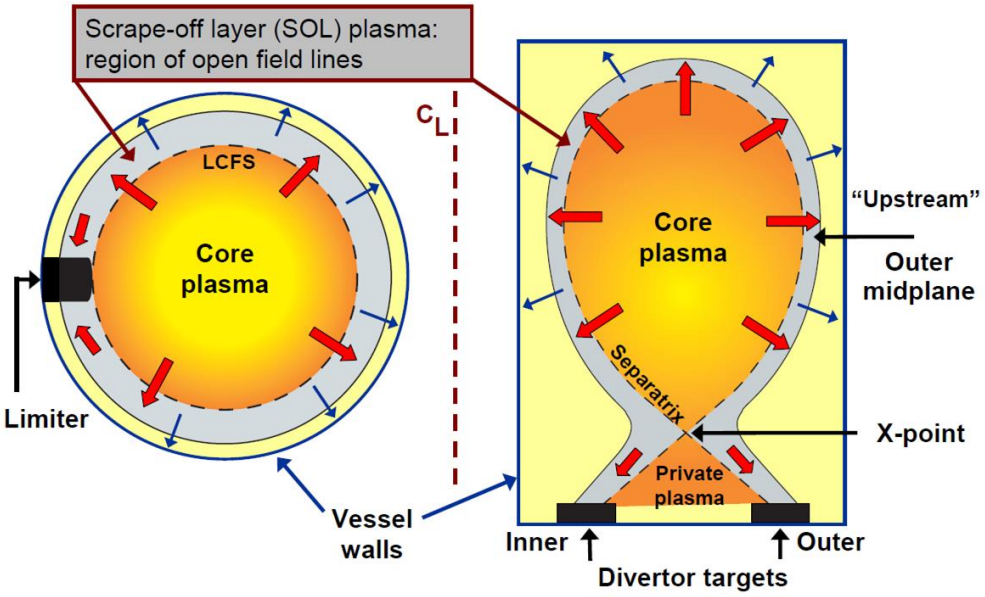

Figure1.4 Schematic diagram of poloidal flux surface in a tokamak (a) with a limiter and (b) with a poloidal divertor. The toroidal field is normal to the page [25].

1.2.3 Power handling issues

The current design of ITER-PFC, i.e. divertor, employs tungsten as the plasma-facing material, brazed on a copper alloy heat sink to be actively cooled by water. This metal-brazed structure is expected to withstand steady state heat loads up to 10-20MW/m^2 at temperatures around 1000^{o}C, and also to survive sputter erosion by D, T and He, perhaps at particle fluxes up to the order of 10^{23} ions/m^2/s [26], over an extended period of time.

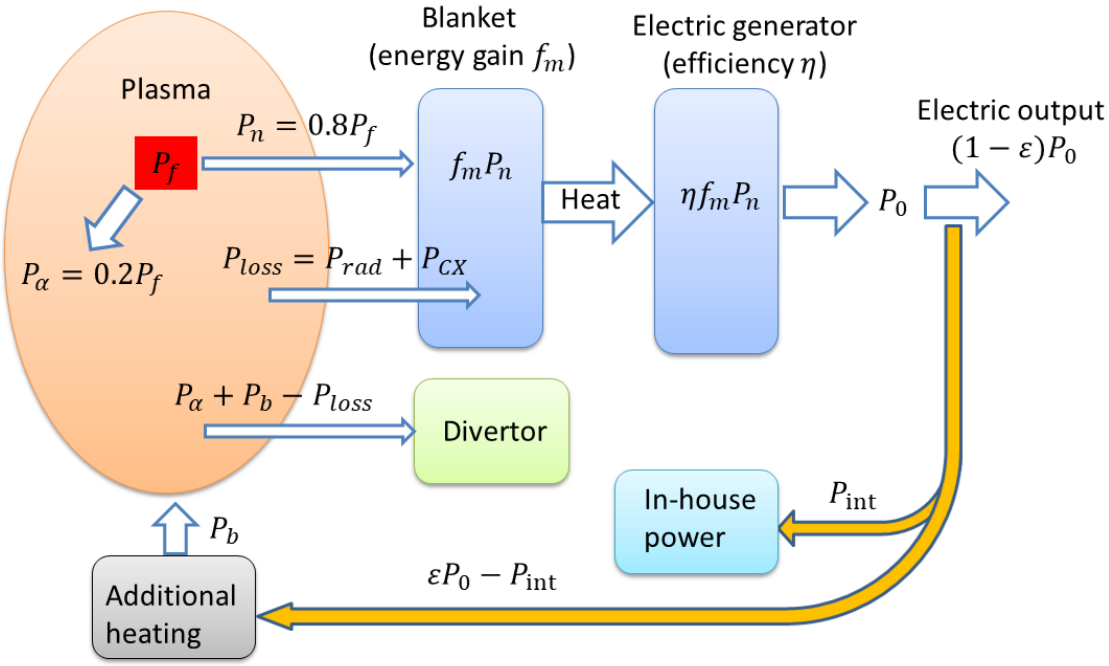

Figure 1.5 Power flow in fusion reactor

Figure 1.5 shows the power flow in a fusion reactor. For the case of ITER, addition heating power P_b =50MW; fusion power P_f =500 MW (Q=10); $P_{loss}(Bremsstrahlung) \approx 66$MW[1]. The total power to divertor :

$$P_d = P_\alpha + P_b - P_{loss} = 0.2 \times 500 + 50 - 66 = 84\ MW \qquad (1.11)$$

The plasma wetted area on the divertor plate [25]:

$$S \approx R \times \lambda_q \times \text{geometry factors} \approx 1.2\ m^2 \quad [\lambda_q = 1mm] \qquad (1.12)$$

As to the heat loads, much attention has recently been directed towards the power deposition profile on the divertor plate. The ITER divertor plasma footprint used to be

estimated to be ~5mm wide up until recently, but now is only ~1mm wide [27], as shown in Figure 1.6, which means that the heat load could be as large as 50-100MW/m^2. One predicts that the divertor heat load would be even higher for a DEMO reactor in which the core plasma will be heated with much more power. Although high particle fluxes might naturally lead to the detached condition, reducing the heat load to some extent, the effect of plasma detachment on core plasma confinement is not clear yet.

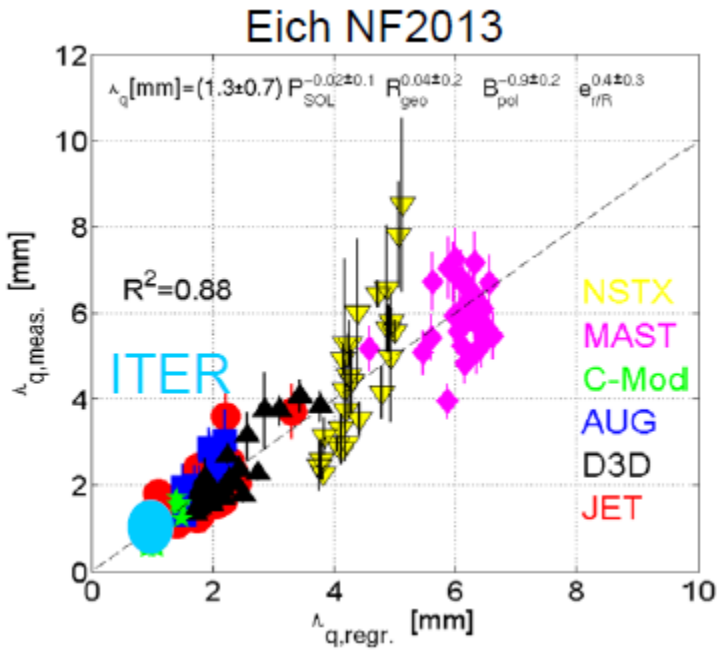

Figure 1.6 Divertor power deposition width database for ITER and other existing fusion devices [27].

For power plants to be built after the DEMO reactor, the use of reduced activation ferritic/martensitic steel (RAFMS) alloys will be enforced from the local radiation safety point of view. Unfortunately, the thermal conductivities of these RAFMS alloys are typically about one third of those of copper alloys. It is thus unlikely that metal-brazed structure PFCs are employed for exhaust power and particle handling in fusion power reactors.

In addition to these technical issues, the mechanical properties of tungsten materials, produced either by produced either by powder metallurgy (PM) or chemical vapor deposition (CVD), are extremely difficult to control from the reactor operation point of

view. The ductile-brittle transition temperature (DBTT) of pure tungsten has been reported to be around 400^{o}C [28]. As opposed to this, the DBTTs of widely used engineering metals such as stainless steel are typically below 0^{o}C. This means that when the temperature of divertor plates goes across DBTT during reactor power ramp up and down, tungsten will most likely suffer from cracking. Shown in Figure 1.7 as an example of DBTT effects are the surface morphologies of PM and CVD tungsten after a number of heat cycles, crossing the DBTT to reach the maximum temperatures of ~1300^{o}C.

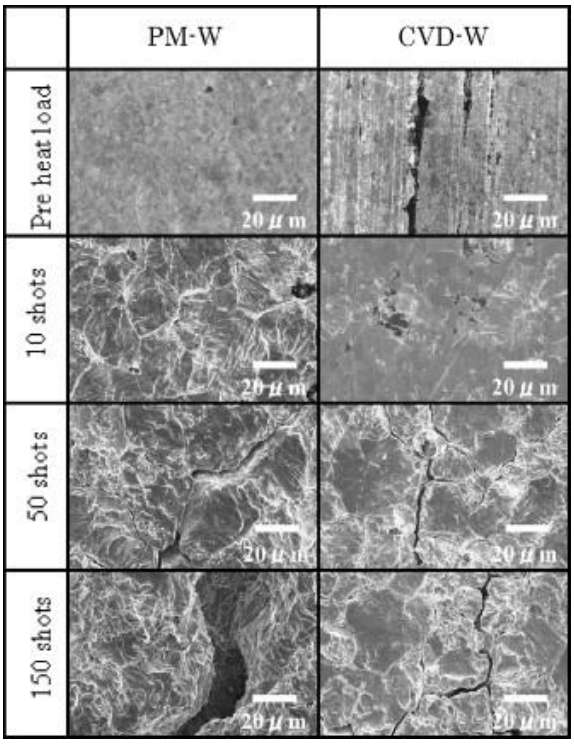

Figure 1.7 SEM micrographs of the surface of CVD-W/Mo (surface temperature: 1250–1300°C) and PM-W (surface temperature: 1280–1380°C) after heat load tests at a heat flux of 50 MW/m^2, 30s [28].

Importantly, depending up on their depths, these DBTT-cracks can extend to affect the brazed joint and act as a sink to tritium co-deposited with impurities. Furthermore, it has been reported that the DBTT of tungsten can be raised by neutron irradiation [29] and perhaps by hydrogen implantation as well, resulting in the formation of microscopic voids [30], all of which would endanger the mechanical integrity of metal-metal brazing.

To lower the DBTT of tungsten, efforts have been devoted, for example, by alloying with other refractory metals such as rhenium. Unfortunately, most of these tungsten alloys exhibit increased induced radioactivity and also reduced mechanical strength [31]. From this point of view, tungsten is not the best choice for the divertor, not just in power reactors but perhaps in ITER as well. These approaches, however, have not yet led to a fully acceptable solution and the design of the divertor remains one of the most difficult problems in the path of fusion power development. These arguments point to a need for the development of innovative PFC concepts.

1.2.4 Particle handling issues

Turning to the issues with particle control, the use of limiters and/or pumped limiters as PFCs was in common with most of the confinement experiments up to 1980s, including those in TFTR. On the other hand, it is also true that limited plasmas can easily be deteriorated by "cold" neutral particles recycling from these PFCs. Nowadays, divertors and pumped divertors are widely used as the PFCs in most of the confinement devices.

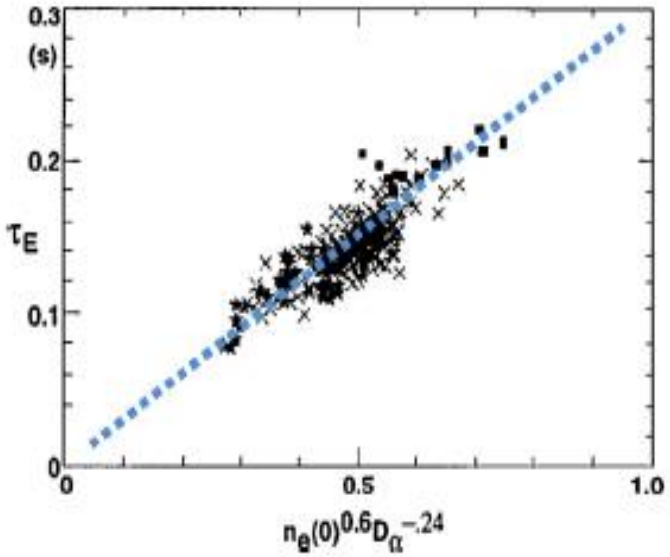

Figure 1.8 Energy confinement time database from TFTR [32]. The dotted line is drawn for the sake of eye guiding. Data include supershots with lithium coatings on the inner bumper limiter.

It was demonstrated that the detrimental effect of particle recycling can be controlled by wall conditioning for the first time in TFTR nearly three decades ago, leading to improved confinement discharges referred to as “Supershots”[32]. Shown in Figure 1.8 is the energy confinement time scaled with the edge plasma density, data taken from these supershots. The implication one finds from this database is that for the same central density ($n_e(0)$), the lower the edge plasma density goes ($D\alpha$), the longer the energy confinement time (τ_E) becomes. Interestingly, though, the physical mechanism of supershot confinement via reduced particle recycling has not yet been understood.

Ever since the discovery of supershot confinement, a variety of wall conditioning techniques to reduce particle recycling have been applied in a number of confinement devices. Among all these techniques, lithium coatings over PFCs have so far been found to be the most effective in improving core plasma confinement. Li coatings have been routinely put down on PFCs in NSTX [33] and EAST [34] to improve core plasma performance.

By definition, any coatings have a finite thickness and thus will eventually be saturated with implanted hydrogenic species and/or gettered impurities, which necessitates the shutdown of plasma operation for re-conditioning. Needless to say, this is not acceptable from the point of view of operating steady state magnetic fusion power reactors. Also, these coatings cannot take any heat fluxes, exceeding $50MW/m^2$, which thus leads us to the use of flowing liquid metals as plasma-facing materials, perhaps as in the “liquid metal waterfall” concept proposed several decades ago [35]. It is clear that one has to take into account all the complications that arise from electromagnetic effects on flowing liquid metals in a magnetic fusion environment.

1.3. The application of liquid metals for PFCs

1.3.1 The advantage of liquid metals

At present, lithium, tin and gallium and their alloys are the possible candidates for liquid PFCs. Shown in Table 1.1 is the melting point and the atomic number of some metals. Liquid metal PFCs have some potential advantages over solid PFCs:

- Very high steady, and transient heat exhaust: 50 MW/m^2 exhausted from electron beam heating; also pulsed 60 MJ/m^2 in 1 μsec [37].
- Tolerable erosion from a PFC perspective: self-healing surfaces.
- No dust generation.
- Eroded chamber material from the main chamber that was transported to the divertor could be removed via liquid flow (with solid PFCs, this is referred to as 'slag') [38].
- Neutron/dpa tolerance; note that the underlying substrate would still have neutron-induced modifications.
- Substrates below LM are protected from plasma-material interactions.
- Liquid lithium specifically offers access to low recycling, high confinement regimes in certain surface temperature ranges.

Table 1.1 The properties of some metals [36]

	Li	**Ga**	**In**	**Sn**	**$Ga_{67}In_{20.5}Sn_{12.5}$**	**W**	**Ti**
Melting point(^oC)	180.5	29.8	157	231.9	10.5	3422	1668
Atomic number Z	3	31	49	50	(37)	74	22

1.3.2 Liquid surface experiments in confinement devices.

The liquid metal divertor was first proposed in the UWMAK-1 Design Report [39], mainly to provide strong particle pumping with free-falling liquid lithium. A free-falling liquid gallium curtain was tested on the T-3M tokamak [40, 41] and a lithium capillary pore system was tested in the T-11M tokamak [41]. The liquid wall idea evolved during the APEX study into a number of concepts based on: (a) using liquid metals (Li or Sn–Li) or a molten salt (Flibe) as the working liquid [42]. Shown in Table 1.2 is a brief review of liquid surface experiments in confinement devices[43].

Exploitation of the beneficial effects of Li has become a significant part of PPPL's mission after its successful use in TFTR. NSTX is a spherical torus that began operation

in 1999 and utilized much of the infrastructure from TFTR. NSTX evaporated Li onto graphite PFCs as a wall-conditioning technique beginning in 2006, developed the LITERs (Li Evaporators) for this purpose and demonstrated improved plasma performance [33]. For the final run campaign in 2010, NSTX had a large area, heated, liquid Li divertor or LLD, as shown in Figure 1.9 [44]. Graphite tiles with diagnostics and other instrumentation separated its 4 segments. Two LITERs evaporated Li onto the porous Mo layer on the surface of the LLD. The surface has a thin SS liner, bonded to a 22 mm-thick copper substrate with embedded electric heaters. Impurity emission from the divertor suggests that the plasma is interacting with oxygen-contaminated lithium whether diverted on the LLD or not. A database of LLD discharges is analysed to consider whether there is a net effect on the discharges over the range of total deposited lithium in the machine. Examination of H-97L indicates that performance was constant throughout the run, consistent with the hypothesis that it is the quality of the surface layers of the lithium that impact performance. The accumulation of impurities suggests a fully flowing liquid lithium system to obtain a steady-state PFC on timescales relevant to NSTX.

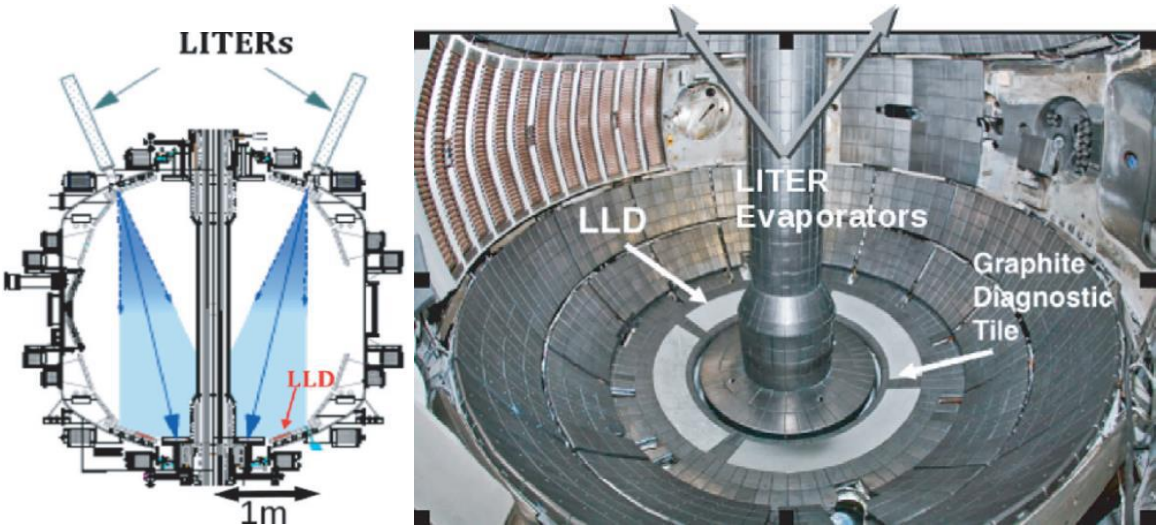

Figure 1.9 The Liquid Lithium Divertor in NSTX [44].

The institute of plasma physics in China (ASIPP) has had a long-term program on the Li application for PFCs on two superconducting tokamaks. One device was HT-7 (shut down in 2012) and the other is EAST. The ultimate aim of the Li program at ASIPP is to realize a large-area flowing liquid Li divertor on EAST. A continuously flowing liquid Li limiter based on the concept of a thin flowing film, has been successfully designed and tested in the EAST device, as shown in Figure 1.10. The experiment has confirmed that the liquid Li can be driven by built-in DC EM pumps to form a recirculating, closed loop system for fusion devices. Further, it is also found the flow rate of liquid Li could be controlled by adjusting the DC current. By using the FLiLi limiter, a modest improvement of plasma performance was obtained, as indicated by reduced core impurity radiation and hydrogen recycling [45,46].

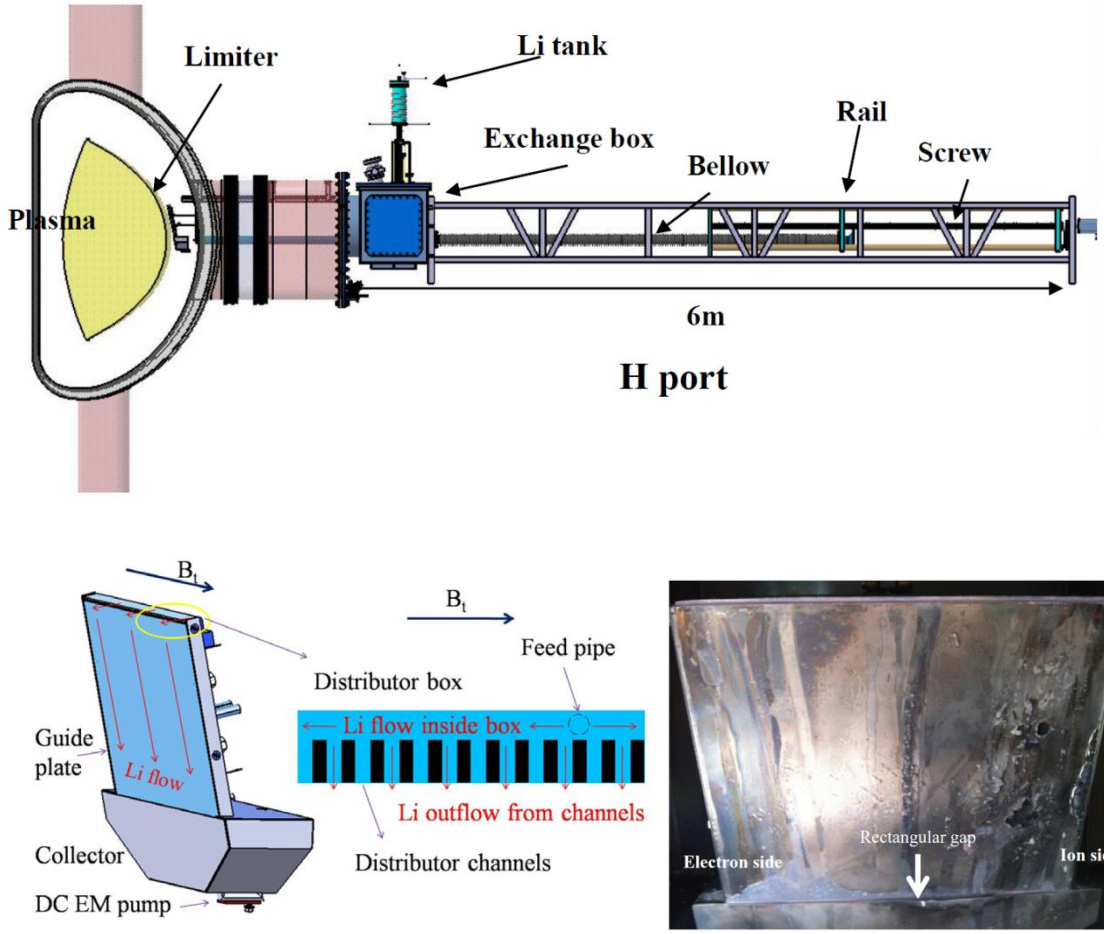

Figure 1.10 (a) Overall structure diagram of the flowing Li limiter system on EAST. (b**)** The sketch of the FLiLi limiter and Li distributor. (c) The picture of the FLiLi limiter surface taken in the airafter the campaign of EAST [45].

Spontaneous thermoelectric magnetohydrodynamic (TEMHD) flow was observed, indicating that the thermoelectric effect causes a current to develop between a liquid metal and a container wall, which exerts the Lorentz force in the presence of magnetic field [47]. Proof-of-principle experiments on the TEMHD-divertor concept have successfully been conducted both in a laboratory facility [48] and a confinement facility HT-7 [49, 50], as shown in Figure 1.11. Full exploitation of TEMHD could enhance the heat handling capability of the divertor, but active control of the flow would be desirable and even essential for the controllability of divertor capabilities. More recently, another innovative divertor concept has been proposed, referred to as ACLMD for the actively convected liquid metal divertor, which will be shown in detail in Chapter 6.

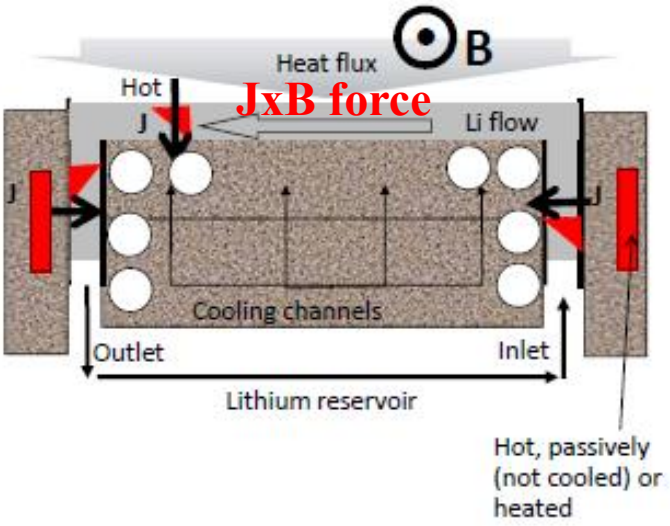

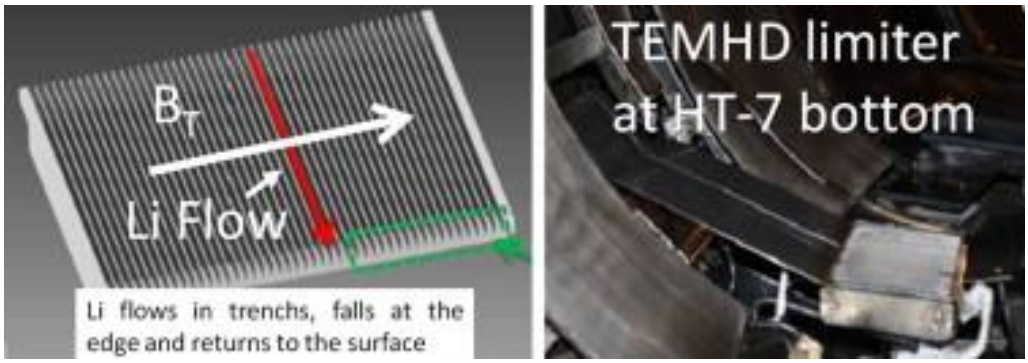

Figure 1.11(a) The Lithium/Metal Infused Trenches (LiMITs) concept, which utilizes the thermoelectric magnetohydrodynamic (TEMHD) driven flowing the liquid metal.(b) Proof-of-Principle experiment in HT-7 [49].

Table 1.2 Liquid surface experiments in confinement devices [43].

Large area or flowing liquid Li, Sn, Sn-Li or Ga PFCs	Capillary pore system (CPS) PFCs
LTX , the only device with a **full liquid Li wall**, has extremely encouraging results on confinement. **HT-7** deployed **2 flowing Li modules** developed by US researchers plus other ways to expose liquid Li to plasmas. Free Li surfaces produced high Li emission and many shots disrupted likely from J ×B forces dislodging Li. **NSTX** operated with the **Liquid Li Divertor** (LLD) and coated it using two previously developed LITER Li evaporators. The upgraded **NSTX-U** started operation in 2016. **CDXU**, the 1st tokamak with a **large area of liquid Li** , used heated SS trays as a floor limiter filled from an injector nozzle. Earlier experiments had a mesh-covered rail limiter fed with Li by a tube. **T-3** and **T-11** used liquid Ga early in the Russian program. Researchers used **flowing Ga limiters**, attempted a **flowing sheet of Ga** , and successful tests in **T-3 M** compared the impurity influx of a **Ga droplet limiter** with that from a graphite limiter. **ISTTOK** , with a **free surface jet of Ga** , showed trapping of H and saturation of the effect, but also hydrocarbons and hydroxides in the near surface region.	**T-11M** and **T-10** operated with **CPS-LLLs (liquid Li limiters)** , extracted H and D and Li with cryogenic targets without venting chamber, and collected ~60 mg Li in 200 regular shots. **T-15** plans. **FTU** had improved plasma performance with a rail type **CPS-LLL** built in a Russian collaboration with ENEA-Frascati. **HT-7** operation with modular **CPS-LLL**, developed by Russian researchers, improved the retention of Li on its surface in comparison with free surface in HT-7 noted above **TJ-II** utilized a **CPS-LLL** with positive or negative bias and had devoted experiments on recycling, and also exposed **SnLi** . **KTM** has an uncooled module. Tests on a **CPS module** with Na-K confirmed reliable operation over temperature range of 20–200 °C. **Lithitization, R&D with Sn or Ga** REFS **NSTX** operated with the **Liquid Li Divertor** (LLD) and coated it using two previously developed LITER Li evaporators. The upgraded **NSTX-U** is starting operation in 2015–16. Injected **Li droplets** in **TFTR's** plasma edge achieved "Supershots". **Li pellets** and **Li spray** in **DIII-D** resulted in enhanced confinement correlated with recycling. Motion of **liquid Li** was observed using the DIII-D DiMES probe. Researchers at **EAST** used **Li injection** for ELM control and various methods to expose liquid Li to the plasma. Researchers at **TJ-II** studied the combined effects of Li evaporated onto walls and boronization. **Lithitization** enabled routine operation using 2 neutral beams, clear transitions to H-mode and doubled confinement times. Experiments in **TJ-II** and in **ISSTOK** also exposed **SnLi**. Experiments in **RFX–mod** studied control of electron density using **Li evaporation** to cover the graphite wall before the discharges or injection of single or multi-pellets. The extensive Russian program on liquid surfaces has included analysis of **Li droplet deformation**, lab experiments with **Ga waterfalls**, testing of **droplet flow** and a **flowing Ga sheet**, and measuring the s**puttering of Ga**. R&D in Latvia tested the **suppression of splashing** in a 1T magnetic field. **Li dust** injected in **T-10**. **Liquid Sn** was exposed to **ASDEX-U** plasma to observe wetting and motion.

1.4. Hydrogen isotopes transport parameters in liquid metals

The proper design of a fusion reactor is not possible unless there is an understanding of the hydrogen isotope retention and recycling for the plasma-facing components. From the tritium inventory point of view, it is absolutely necessary to understand the short-term and long-term hydrogen isotopes retention characteristics of the individual materials used for the first wall and divertor. From the plasma density and fueling point of view, it is necessary to understand the recycling characteristics of these materials. At present, lithium, tin and gallium and their alloys are the possible candidates for liquid PFCs. R.A. Causey has reviewed the hydrogen isotopes transport parameters for lithium, tin, and gallium [51]. Some updated data are contained and discussed below.

1.4.1. Diffusivity

Moriyama et al. [52] used a capillary method to determine the diffusivity of tritium in liquid lithium. Their experiments determined the diffusivity to be given by $D=8.56\times10^{-12}$ T/μ m^2/s, where T is the absolute temperature and μ is the viscosity of the liquid lithium. The authors quoted Shpil'rain et al. [53] for the viscosity, μ, of lithium to be given by $\log\mu = 1.4936-0.7368\log T+ 109.95/T$. Buxbaum and Johnson [54] also measured the diffusivity of tritium in liquid lithium. Their values were slightly lower (about a factor of 4) than those measured by Moriyama et al. [52], but had the same slope. Alire [55] examined the diffusivity and solubility of hydrogen in liquid lithium by examining the consumption of hydrogen in lithium and the Nb/Zr container in which it was held. This experiment, which required corrections for the transport through the container, determined that the diffusivity of hydrogen in lithium between 898 and 1178 K to be $D=1.3\times10^{-3}$ exp(-1.09eV/kT) m^2/s. These results are in strong contrast (much higher activation energy) to the results of Moriyama et al. and Buxbaum and Johnson. It is almost certain that the diffusivity through the container and release from the container surface into the lithium strongly affected the results. It should be noted that the values determined by Moriyama et al. and Buxbaum and Johnson for the diffusivity are much higher than those for solids. The diffusivity lies close to 10^{-8} m^2/s for all temperatures between the melting point and 1000 K. The high mobility is significant in that it makes it almost impossible to achieve highly localized tritium concentrations in the liquid metal.

Even at fluxes of 1 A/cm^2, the tritium concentration at the end of range cannot rise above about 2% (based on calculations using the TMAP [56] computer code). The limited concentration should reduce the rate of production of lithium hydride (which only forms when the hydrogen concentration exceeds a few atomic percent), and reduce the chance of bubble formation in the liquid. However, the recent hydrogen diffusivity data measured by Fukada et al [57] show several orders of magnitude lower than those measured by Moriyama et al, as shown in Figure 1.12. Hydrogen diffusivity in liquid lithium was measured by gas-driven permeation(GDP) experiment in the temperature range from 500 to 650^{o}C. Fukada got the diffusivities based on the assumption that the surface reaction rate k_f is large, and GDP through liquid lithium is diffusion limited.

There appear to be no data available on the diffusivity of hydrogen in tin or gallium. An approximation for the diffusivity is given by Cussler [58] who generalized that the diffusivity of any solute in any liquid solvent is constant at approximately 7×10^{-10} m^2/s. This value is lower by a little less than an order of magnitude than the values reported in the above paragraph for liquid lithium, and should serve as an approximation until additional experiments are performed.

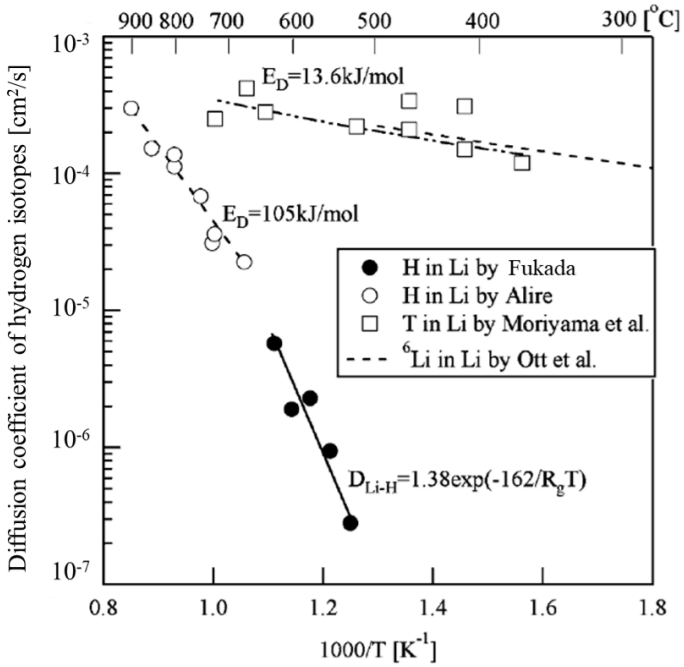

Figure 1.11 Hydrogen isotopes diffusivity in liquid lithium [57].

1.4.2. Solubility

For a phase diagram of the Li–LiH system, the reader is referred to Hoch [59]. Basically, at higher temperatures there is a single liquid present which disproportionates into two liquids (Li and LiH). Above 454 K but below 958 K, there is a two phase region composed of liquid lithium and solid lithium hydride. Examination of the phase diagram leads to the conclusion that very large amounts of hydrogen can be incorporated into a layer of liquid lithium. The implications of the large capacity to the behavior of plasma wall interactions in a fusion reactor are demonstrated in the next section on ion implantation. Several researchers have determined the solubility of hydrogen isotopes in liquid lithium. Katsuta et al. [60] determined the inverse of the solubility to be given by the expression $K_s=3.8\times10^{-3}\exp(0.46\text{eV/kT})$ $(\text{H/Li})/\text{atm}^{0.5}$ from about 700 K up to about 900 K. Veleckis et al. [61] also determined the solubility of hydrogen in liquid lithium. For temperatures between 993 and 1176 K, their expression for the solubility is given by $K_s=1.5\times10^{-3}\exp(0.53\text{eV/kT})$ $(\text{H/Li})/\text{atm}^{0.5}$.

Iwase [62] reported very low hydrogen solubilities for tin. The solubility varied from 0.47×10^{-4} H/Sn at 673 K up to 1.54×10^{-4} H/Sn at 1278 K. Even though no definitive data are available on the hydrogen solubility in gallium, Mueller et al. [63] compare it to boron and indium to conclude that the solubility is negligible. Gallium forms a hydride, but it is only formed in special conditions in the laboratory.

1.4.3. Ion implantation

Erents et al. [64] used a mass analyzed 18 keV deuteron beam to examine the interaction of energetic hydrogen isotope ions with solid and liquid lithium. While conflicting results were obtained for the solid phase, the liquid phase with a clean surface resulted in 97% retention of the implanted deuterium for ion fluxes between 2.5×10^{18} and 2.5×10^{19} ions/m^2s. The fractional retention was seen to drop as temperatures exceeded 680 K. Baldwin and Doerner [65] have reported deuterium retention measurements showing almost 100% retention of all implanted deuterium even at the extremely high fluxes possible using the linear plasma device PISCES.

1.5 Objectives of this work

The design of a fusion reactor requires an understanding of the hydrogen isotope (protium, deuterium, and tritium) retention and recycling that will occur during operation. Retention of the hydrogen isotopes is particularly important if the isotope is tritium. Retention of large quantities of tritium in the reactor plasma facing components increases the fuel costs of the reactor and presents a safety concern. Recycling is the rate of return of the cold hydrogen to the plasma, controlling the fueling rate and affecting the plasma performance. The understanding of hydrogen transport properties in liquid metals is essential for studying retention and recycling. This PhD thesis research aims:

- To understand the mechanism of hydrogen isotopes transport in liquid metals under plasma bombardment.
- To establish a database on transport parameters (diffusivity, recombination coefficient, solubility) and dynamic/static retention of hydrogen isotopes for designing liquid metal PFCs for fusion power reactors.
- To investigate the natural and forced convection effects, if any, on the hydrogen transport behavior in liquid metals.

1.6 Outline of the thesis

The thesis is arranged as follows: after this introduction, some theories and models on hydrogen isotopes transport in liquid metals will be briefly reviewed in Chapter 2. In chapter 3, the experimental setups in a laboratory-scale steady-state plasma device: VEHICLE-1 for plasma-driven permeation will be shown in detail. Shown in Figure 1.12 is the research procedure chart. In Chapter 4, studies on hydrogen isotopes (H/D) plasma-driven permeation through solid Ti and liquid metals including Li, GaInSn and Ga will be presented. The simulation and experimental results on deuterium transport in liquid GaInSn under natural convevction will be shown in Chapter 5. The simulation and experimental results on particle recycling from liquid GaInSn under J×B-forced convection will be presented in Chapter 6, followed by a summary of the whole thesis in Chapter 7.

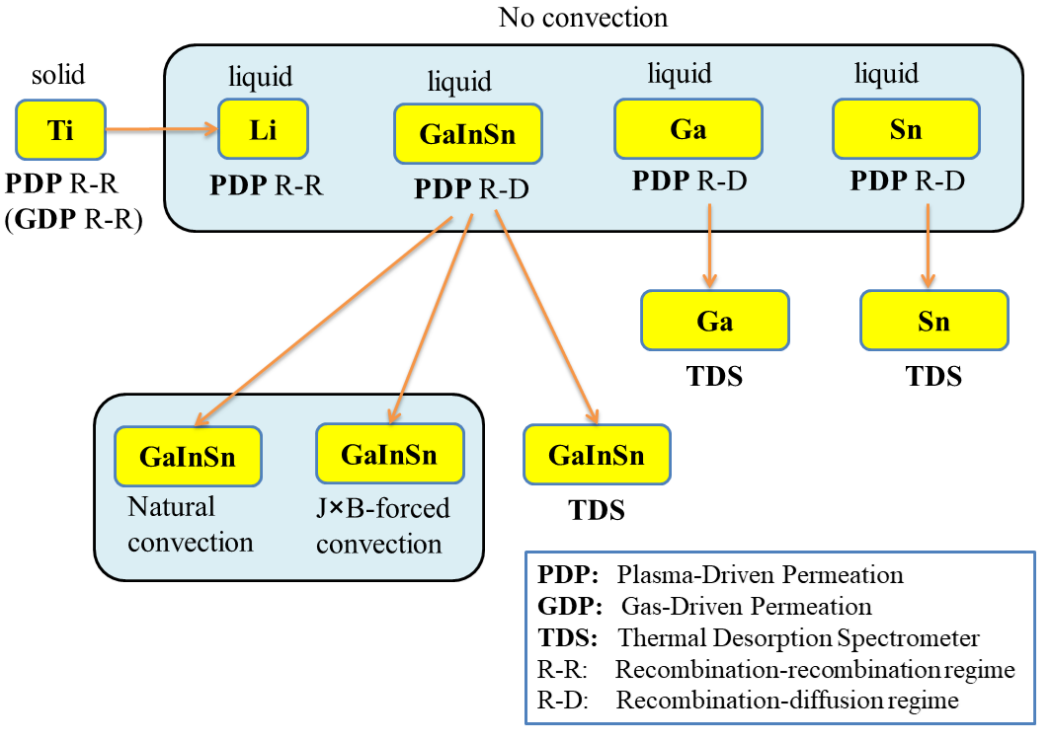

Figure 1.12 Research procedure chart

Chapter 2 Theories on hydrogen transport in liquids

In Chapter 1 the database of hydrogen isotopes transport parameters in some liquid metals has been briefly reviewed. To understand those data for PWI, this chapter reviews some of the physical mechanisms involved in the interaction of hydrogenic particles with solids, their diffusion and trapping in the solids, and the surface recombination allowing them to be released. After that, the physical mechanisms of hydrogen isotopes transport in flowing liquids are reviewed. In the latter part of the chapter, the steady state permeation models and hydrogen isotope effects are shown.

2.1. Trapping and release of hydrogen isotopes in solids

The design of a fusion reactor requires an understanding of the hydrogen isotope (protium, deuterium, and tritium) retention and recycling that will occur during operation. Retention of the hydrogen isotopes is particularly important if the isotope is tritium. Retention of large quantities of tritium in the reactor plasma facing components increases the fuel costs of the reactor and presents a safety concern. Recycling is the rate of return of the cold hydrogen to the plasma, controlling the fueling rate and lowering the plasma temperature. The different processes controlling the retention as well as the recycling of the hydrogen isotopes in the plasma-facing components are shown in Figure 2.1 [51]. A fraction of the ions striking the surface are directly scattered back into the plasma. The number of particles promptly returned to the plasma by this scattering process depends on the incident energy of the incoming particles as well as the type of material. Particles stopped in the material have several possible fates. Previously existing defects, defects resulting from fusion neutrons, and defects caused by the energetic hydrogen ions may trap hydrogen atoms in the implantation zone, defined by the maximum range of the incident hydrogen. In the extreme case where the hydrogen solubility is very low in the implanted material, molecular recombination within the implantation zone may occur. Bubble coalescence can eventually lead to an open porous implant layer. In the more normal case, the traps eventually become saturated, and the untrapped hydrogen atoms diffuse out of the implant zone, going either deeper into the material or to the front surface. Those atoms heading deeper into the material will eventually find traps outside of the implant zone, or will reach the backside of the material.

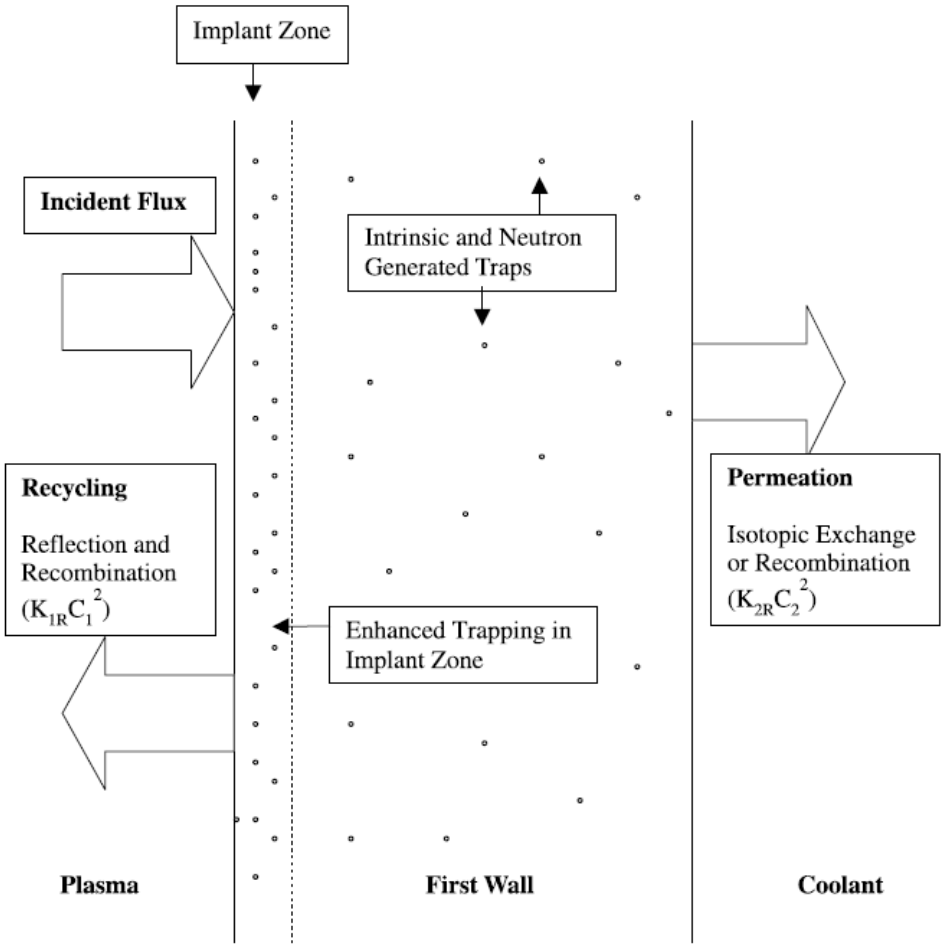

Figure 2.1 Processes involved in the hydrogen isotope retention and recycling in fusion reactor plasma-facing materials [51].

2.1.1. Reflection and implantation

When energetic hydrogen atoms or ions impinge on the first walls, a fraction of them is reflected in a time of $\leq 10^{-12}$ s [66]. The particle reflection coefficient, $R_{N,}$ is defined as the number of all backscattered particles, N, divided by the number of incident particles, N_0. As shown in Fig. 2.2, the particles backscattered have distributions in energy E, exit polar angle β, exit azimuthal angle φ and charge state q_i, depending on the incident energy, $E_{0,}$ and angle, α, which may be described by [66,67]:

$$f(E_0, \alpha; E, \beta, \varphi, q_i) \tag{2.1}$$

Then R_N can be obtained by integrating the distributions:

$$R_N(E_0,\alpha)=\sum_i \int_0^{E_0} dE \int_0^{\pi/2} d\beta \int_0^{2\pi} d\varphi f(E_0,\alpha;E,\beta,\varphi,q_i)\sin\beta \tag{2.2}$$

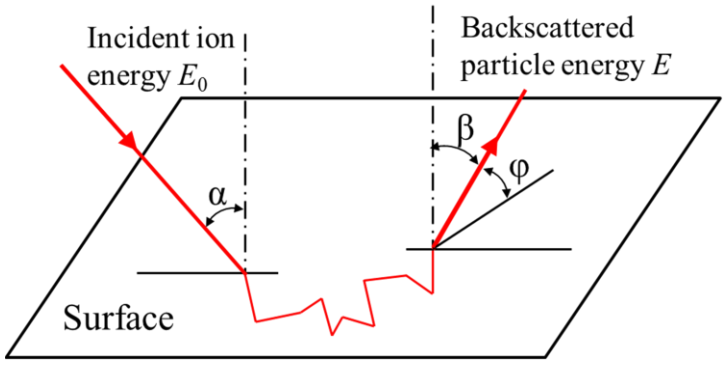

Figure 2.2 Backscattering of an ion with incident energy E_0 from the surface of a solid (re-plot from [66].)

The particles which are not backscattered are implanted into the walls. These particle will be slowed down by transferring energy to the target electrons (electronic stopping), or by interaction with the target atom core (nuclear stopping). The mean range of implantation ions may be calculated by [68]:

$$\bar{d}=\frac{1}{n}\int_0^{E_0}\frac{dE}{S(E)} \tag{2.3}$$

where E_0 is the incident energy, n is the particle number and $S(E)$ is the total stopping cross section from electronic and nuclear stopping.

Based on the binary collision approximation (BCA) [69], several Monte Carlo simulation codes have been developed for plasma-wall interaction applications, for example, TRIM [70], ACAT [71] and EDDY [72]. Shown in Figure 2.3 are the calculation results for the reflection coefficient of hydrogenic particles on a pure iron surface by these codes [73]. The calculated reflection coefficient decreases with the increase of implantation energy, E_0, when E_0 is larger than 10eV. Figure 2.4 shows one

calculation on hydrogen implantation profile in iron by SRIM2008 [74] and EDDY. In general, the calculation results given by these codes are in good agreement.

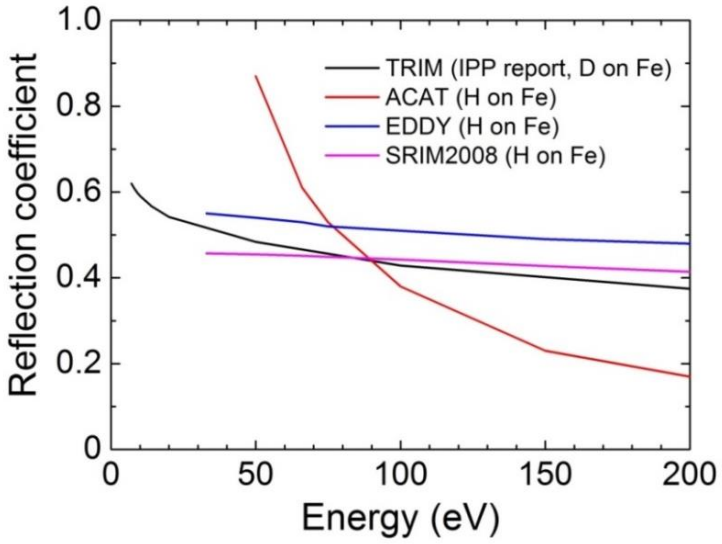

Figure 2.3 Particle reflection coefficient of hydrogen on iron estimated by the Monte Carlo codes [73]. For the IPP report, see [70].

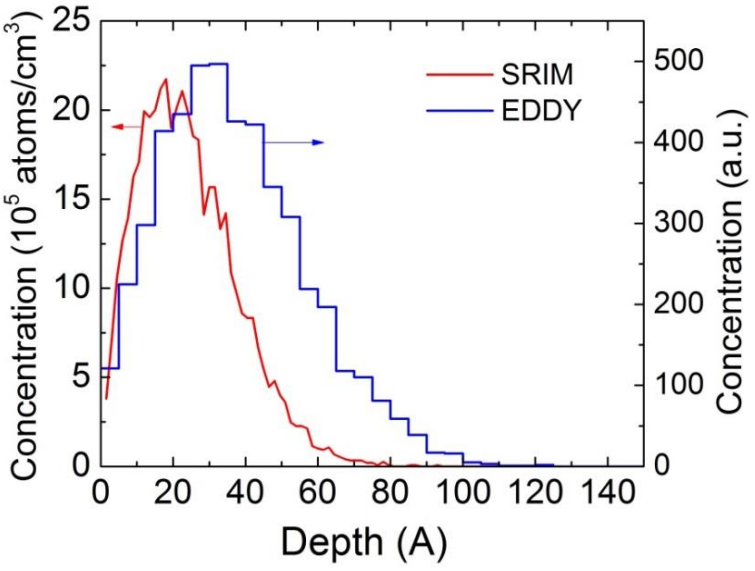

Figure 2.4 Calculated hydrogen implantation profile in iron by SRIM2008 and EDDY codes. The implantation energy is 100 eV [73].

2.1.2. Solution

For hydrogen gas and solids in thermodynamic equilibrium, the hydrogen solubility in metal is proportional to the square root of the partial pressure of the gas (Sieverts' law [75]) and the bulk concentration C can be given by:

$$C = S \cdot \sqrt{p}\,, \tag{2.4}$$

with S denoting the solubility expressed by [68]:

$$S = S_0 \exp(-\frac{U_S}{kT})\,, \tag{2.5}$$

where U_S is the enthalpy of solution, which may be positive for endothermal hydrogen-solid system and negative for the exothermal case.

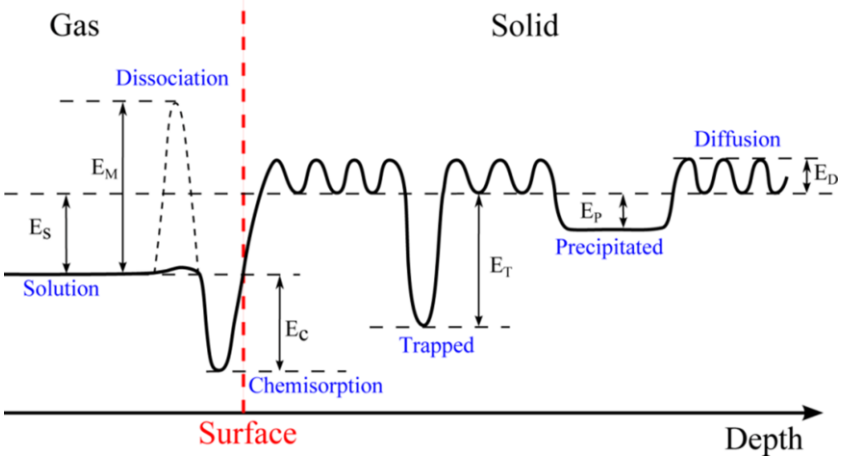

Figure 2.5 Schematic energy diagram for hydrogen in metals. (Re-plot from [68]). U_S, U_C, U_t and U_P are the enthalpies of solution, chemisorption, trapping and precipitation. U_M is the dissociation energy and U_D is the activation energy for diffusion.

2.1.3 Diffusion and trapping

The dissolved hydrogen atoms may migrate in the host lattice, or be trapped by defects and impurities in the lattice. Figure 2.5 shows a schematic energy diagram for hydrogen in metals. It can be seen that the trapping sites expose a higher binding energy than regular solution sites. The behavior of one-dimensional hydrogen transport through a solid with trapping sites can be described by the following equations [76]:

$$\frac{\partial C(x,t)}{\partial t} = D(T)\frac{\partial^2 C(x,t)}{\partial x^2} - \frac{\partial C_t(x,t)}{\partial t} + G(x,t) \tag{2.6}$$

$$\frac{\partial C_t(x,t)}{\partial t} = D(T)\frac{C(x,t)C_t^e(x,t)}{\lambda^2} - C_t(x,t)\nu_0 \exp(-U_t / kT) \tag{2.7}$$

$$C_t^e(x,t) = C_t^0(x) - C_t(x,t) \tag{2.8}$$

where $C(x,t)$ and $C_t(x,t)$ are the concentrations of mobile and trapped atoms as a function of position x and time t; D is the diffusion coefficient; T is the temperature; $G(x,t)$ is the hydrogen implantation profile; $C_t^0(x)$ and $C_t^e(x)$ are the concentrations of intrinsic and empty trapping sites, respectively; λ is the mean distance between trapping sites; ν_0 is the jumping frequency; k is Boltzman's constant and U_t is the de-trapping energy. Equation (2.6) indicates that trapping sites introduced by neutron or energetic particle bombardment will only affect the initial transient permeation behavior.

The diffusion coefficient, D, can be derived from the "random walk" model, in which case D is given as [80]:

$$D = D_0 \exp(-\frac{U_D}{kT}) \tag{2.9}$$

where D_0 is the pre-exponential parameter containing the jumping frequency and lattice structure information, and U_D is the activation energy for diffusion.

2.1.4. Surface recombination

Hydrogen is released from the surface of a solid via the recombination of dissolved atoms to a hydrogen molecule. The recombination flux (i.e. re-emission flux) $J_{\_}$ is proportional to the square of the bulk concentration C at the surface [3]:

$$J_{\_} = K_r \cdot C^2 \tag{2.10}$$

with the recombination coefficient K_r.

Based on the idealized energy diagram shown in Figure 2.5, several models for estimating K_r have been proposed (see Ref. [77], [78] and [79]). Baskes [77] gave a simplified method to calculate the recombination coefficient and the K_r is given as:

$$K_r = \frac{K_0}{\sqrt{T}} \exp(-\frac{U_K}{kT}) \tag{2.11}$$

where U_K is the activation energy of recombination and $U_K = U_D+U_S$ when $U_D+U_S \geq 0$; and $U_K = 2U_S$ when $U_D+U_S < 0$. K_0 is a pre-factor which is related to the solubility, diffusivity and surface sticking coefficient:

2.2. Hydrogen isotopes transport in liquids

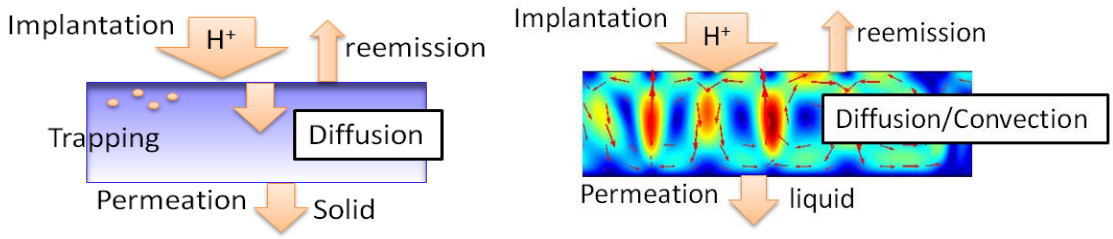

Fig.2.6 A schematic diagram of hydrogen transport (a) in a solid and (b) in a liquid under plasma bombardment.

For liquid metals, due to the mobility or flowing property, the incident hydrogen atoms transport by not only diffusion but also convection, as shown in Figure 2.6. The velocity of a molecule undergoing mass transfer incorporates both convective

and diffusive component. We understand convection as mass transport due to the average velocity of all molecules, and diffusion as mass transport due to the instantaneously varying, randomized velocity of individual molecules, compared to the average velocity of the fluid as a whole. Hence, by a suitable choice of reference velocity, we can identify a diffusive flux and a convective flux. For dilute species transport, where one component, such as a solvent or carrier gas, dominates the momentum of the system, it is normal to take the reference velocity as that of the dominant component. The motion of a bulk fluid therefore contributes a flux of dilute species, in addition to the flux due to diffusion. This flux can be written as follows [80]:

$$\mathbf{N}_{i,\text{conv}} = c_i \mathbf{u} \tag{2.12}$$

where c_i is the species concentration (mol.m^{-3}) and $\mathbf{u}$ is the fluid velocity (m.s^{-1}).The convective flux vector is proportional to the fluid velocity, **u**, so it acts in the same direction as this velocity. This is because convection is the transport of mass due to bulk fluid motion. For a dilute species, this velocity is the velocity of the solvent or carrier gas. The change in concentration at a point, due to convection, follows by substituting the above into the mass continuity equation:

$$\left(\frac{\partial c_i}{\partial t}\right)_{\text{conv}} = -\nabla \cdot \mathbf{N}_{i,\text{conv}} = -c_i \nabla \cdot \mathbf{u} - \mathbf{u} \cdot \nabla c_i \tag{2.13}$$

The first term (including $\nabla \cdot \mathbf{u}$) equals zero for an incompressible fluid flow as a result of the conservation of mass of the fluid as a whole. As a consequence, we see that only in the presence of concentration gradients will the concentration at a point be changed by convection:

$$\left(\frac{\partial c_i}{\partial t}\right)_{\text{conv}} = -\mathbf{u} \cdot \nabla c_i \tag{2.14}$$

This is the convection equation, a time-dependent, first-order partial differential equation.

Since chemical species have a nonzero diffusivity in reality, it is normal to solve the convection-diffusion equation, where both the diffusive and convective contributions to the mass transport are included:

$$\frac{\partial C}{\partial t} = \underbrace{\nabla \cdot (D\nabla C)}_{\text{Diffusion}} \underbrace{- \boldsymbol{u} \cdot \nabla C}_{\text{Convection}} + \underbrace{G}_{\text{Source}} \tag{2.15}$$

In a finite element analysis software COMSOL, the fluid velocity, **u** can be obtained in the computational fluid dynamics(CFD) module, by solving the following equations: The continuity equation [80]:

$$\frac{\partial \rho}{\partial t} + \nabla \cdot (\rho u) = 0 \tag{2.16}$$

and the momentum equation:

$$\rho \frac{\partial u}{\partial t} + \rho(u \cdot \nabla)u = \nabla\left[-pI + \mu\left(\nabla u + (\nabla u)^T\right) - \frac{2}{3}\mu(\nabla \cdot u)I \right] + F \tag{2.17}$$

where

ρ is the density (SI unit: kg/m^3);

u is the velocity vector (SI unit: m/s);

p is pressure (SI unit: Pa);

μ is the dynamic viscosity (Pa·s);

F is the volume force vector (SI unit: N/m^3).

For the case of a standing liquid, the velocity vector u=0, then the convection-diffusion equation 2.15 will become a diffusion equation. For the case of a liquid under J×B-forced convection, the volume force vector F= j×B, where j (SI unit: A/m^2) is the current density and B (SI unit: T) is the magnetic field. For the case of a liquid under natural convection, the volume force, F, comes from the buoyancy force, which is induced by thermal expansion of the fluid due to temperature variation. The heat transfer in the fluids module in COMSOL uses the following version of the heat equation to model heat transfer in fluids:

$$\rho C_p \frac{\partial T}{\partial t} + \rho C_p u \cdot \nabla T = \nabla \cdot (k \nabla T) + Q \tag{2.18}$$

where

C_p is the heat capacity at constant pressure (J/(kg·K));

k is the thermal conductivity (W/(m·K));

Q the heat source (W/m^2).

2.3. Steady state permeation models

To evaluate hydrogen isotopes transport parameters, experiments on hydrogen isotopes plasma-driven permeation through standing liquid metals have been proposed. The steady state permeation flux J_+ controlled by diffusion is generally given by Fick's first law [81]:

$$J_+ = -D \frac{\partial C}{\partial x} \tag{2.19}$$

For plasma-driven permeation, three regimes are considered [82,83]: (1) diffusion-limited release of hydrogen from both the upstream and downstream surfaces (to be referred to as the DD regime); (2) recombination-limited release of hydrogen from the upstream surface and diffusion-limited release of hydrogen from the downstream surface (to be referred to as the RD regime) and (3) recombination-limited release of hydrogen for both surfaces (to be referred to as the RR regime).

The rate controlling process can be characterized by the dimensionless parameter W [82]:

$$W = \frac{d}{D} (J_0 K_r)^{1/2}. \tag{2.20}$$

Shown in Fig. 2.7 (a) are the normalized hydrogen concentrations as a function of W, assuming the ratio of the implantation range and the membrane thickness $\alpha = d/L = 10^{-6}$, and the surface conditions for the front surface and back surface are the same ($\beta = K_r/K_l$

=1). C_R, C_0 and C_L are the hydrogen concentrations at the implantation range, front surface and back surface, respectively.

The overall hydrogen transport is controlled by the slowest process and the parameter W may be regarded as a competition between diffusion and recombination. For $W > 1$, which is possible when hydrogen is deeply implanted and diffusion is slow compared with surface recombination, the concentration is peaked at the implantation range d ($C_R > C_0$, C_L, as shown in Fig.2.7(b)). This regime is the DD-regime. For $\beta\alpha < W < 1$, $C_R \approx C_0$ and $C_L \approx 0$, indicating recombination-limited behavior at the upstream surface and diffusion-limited behavior at the downstream surface. If $W < \beta\alpha$, the hydrogen concentration is uniform throughout the membrane and PDP is in the RR regime.

The steady state hydrogen plasma-driven permeation flux J_+ is given by the following formulae:

$$J_+ = \frac{d}{L} J_0 \qquad \text{(for DD regime)} \qquad (2.21)$$

$$J_+ = \frac{D}{L} \sqrt{\frac{J_0}{K_r}} \qquad \text{(for RD regime)} \qquad (2.22)$$

$$J_+ = \frac{K_l}{K_r + K_l} J_0 \qquad \text{(for RR regime)} \qquad (2.23)$$

It should be pointed out that:

(1) In the DD regime, J_+ is not related to the surface recombination coefficients;

(2) In the RD regime, J_+ is only affected by the upstream surface recombination coefficient, but not the downstream surface condition. Meanwhile, only in this regime J_+ is proportional to the square root of the implantation flux J_0.

(3) In both DD and RD regimes, J_+ is inversely proportional to the membrane thickness, L. In contrast, J_+ is not affected by L in the RR regime.

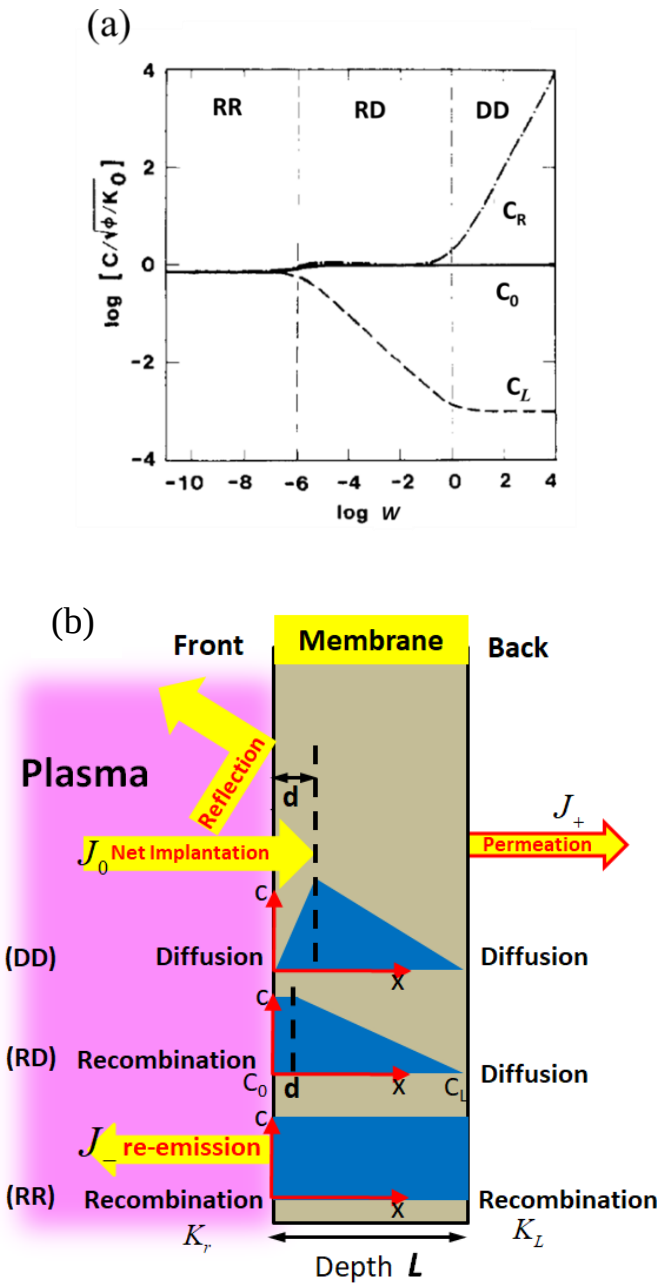

Figure 2.7 (a) normalized hydrogen concentrations as a function of *W* (re-edit from [82]) and (b) hydrogen concentration profiles for the three regimes.

2.4. Isotope effects

For D-T fusion reactor studies, isotope effects must be taken into account because both deuterium and tritium are the fuels. Isotope effects on hydrogen transport can be divided into two classes [84], i.e. intrinsic effects and synergistic effects. The former class is related to the differences in the transport properties of each of the individual isotopes, for example, the isotope dependence of the diffusivity, the heat of transport and trap strength. The latter class is due to the competition of the various isotopes for traps and the coupling of isotopes through the process of surface recombination.

Taking into account the isotope effects, the one-dimensional hydrogen transport process described in (2.6)-(2.8) can be modified as [85]:

$$\frac{\partial C^j(x,t)}{\partial t} = D_j(T)\frac{\partial^2 C^j(x,t)}{\partial x^2} - \sum_i \frac{\partial C_t^{ij}(x,t)}{\partial t} + G_j(x,t) \tag{2.24}$$

$$\frac{\partial C_t^{ij}(x,t)}{\partial t} = D_j(T)\frac{C^j(x,t)C_t^{ei}(x,t)}{\lambda^2} - C_t^{ij}(x,t)\nu_0 \exp(-U_t^i / kT) \tag{2.25}$$

$$C_t^{ei}(x,t) = C_t^{0i}(x) - \sum_j C_t^{ij}(x,t)\,, \tag{2.26}$$

where $C^j(x,t)$ and $C_t^{ij}(x,t)$ are the concentrations of the mobile j^{th} species and trapped j^{th} species in the i^{th} trapping site; D_j is the diffusion coefficient of the j^{th} species; T is the temperature; $G_j(x,t)$ is the hydrogen implantation profile of the j^{th} species; U_t^i is the de-trapping energy of the i^{th} trapping site; $C_t^{0i}(x)$ and $C_t^{ei}(x)$ are the concentrations of intrinsic and empty i^{th} trapping sites, respectively.

2.5. Summary

In this chapter, the physical mechanisms involved in the hydrogen permeation process are briefly introduced. When hydrogenic particles impinge on a solid/liquid, a fraction of them will be immediately reflected. For those hydrogenic atoms implanted into the solid, they will either be transported in the lattice of solids, or be trapped by impurities and defects. Finally, the mobile atoms will be released as molecules by surface recombination.

For liquid metals, due to the mobility or flowing property, the incident hydrogen atoms are transported by not only diffusion but also convection. The velocity vector of the liquid can be obtained by the computational fluid dynamics method.

The theories on hydrogen isotopes transport through solids/standing liquids have been well developed and some hydrogen transport cases can be analytically or numerically solved. This thesis work tries to utilize these theories to explain the observations in various permeation experiments. Using the equations describing the transient and steady state hydrogen transport behavior, the permeation properties of various materials can be evaluated and the transport parameters such as diffusion and recombination coefficients can be measured.

Chapter 3 Experimental setup for plasma-driven permeation

3.1. VEHICLE-1 linear plasma facility

3.1.1. VEHICLE-1 linear plasma facility

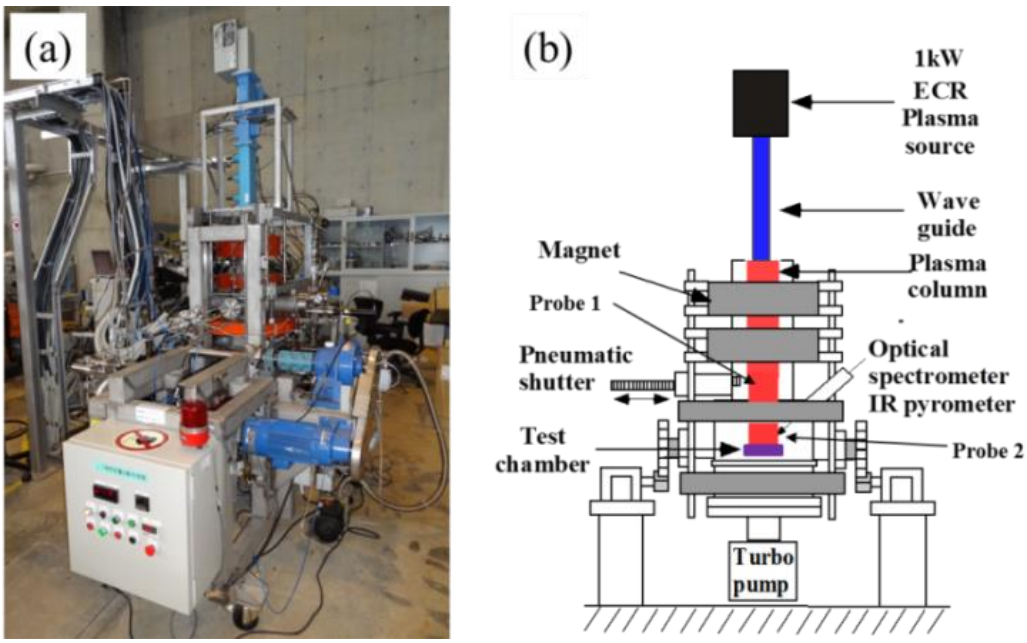

Figure 3.1 (a) The VEHICLE-1 facility and **(b)** a schematic diagram of the device.

Figure 3.1 shows (a) a picture and (b) a schematic diagram of the linear plasma facility: VEHICLE-1 (the Vertical and Horizontal positions Interchangeable test stand for Components and Liquids for fusion Experiments) [87]. The VEHICLE-1 facility employs a 1 kW 2.45 GHz electrical cyclotron resonance (ECR) plasma source, which can generate steady state plasmas. The maximum magnetic field in the resonance zone is 943 G. For well-diagnosed experiments, VEHICLE-1 is installed with a movable Langmuir probe, a digital CCD camera, an optical spectrometer, a total and partial pressure gauges for plasma characterization, and equipped with an infrared pyrometer, thermocouples and a resistive heater for temperature measurements and control, respectively.

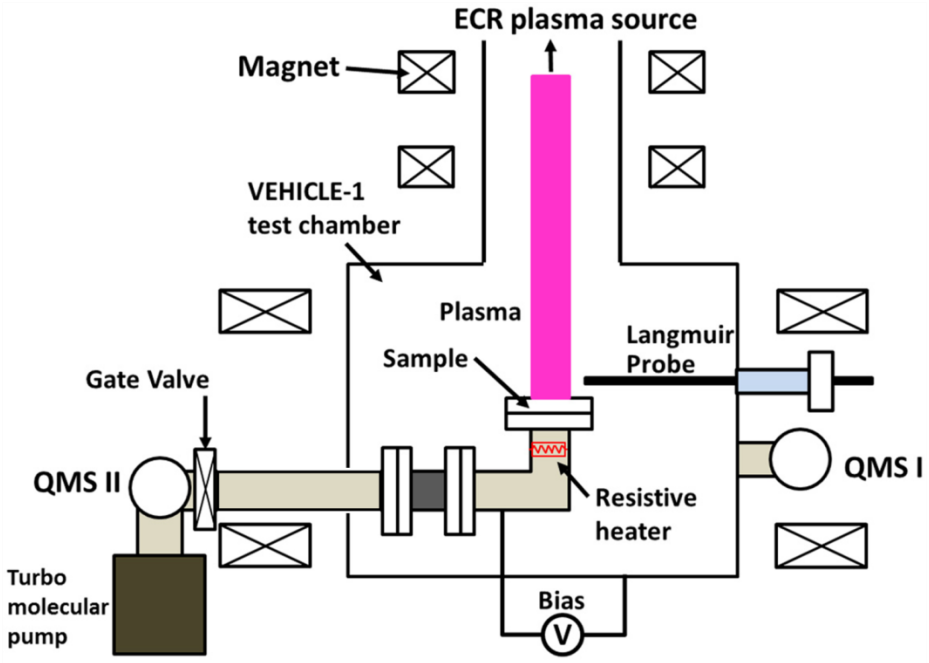

Figure 3.2 A schematic diagram of the plasma-driven permeation setup in VEHICLE-1.

Shown in Figure 3.2 is a schematic diagram of the PDP setup in VEHICLE-1. There are two chambers in VEHICLE-1, and the two chambers are separated by the samples. The plasma is produced in the upstream chamber and guided down to the target samples by the magnetic field. A resistive heater is set beneath the sample to control the temperature. The hydrogen permeation flux due to PDP can be measured by a quadrupole mass spectrometer (QMS) in the downstream side. The plasma density is of the order of 10^{10} cm^{-3}, the electron temperature is ~3eV. The ion bombarding energy is controlled by a negative bias applied to the membrane, relative to the VEHICLE-1 machine ground.

3.1.2. Electron cyclotron resonance (ECR) discharges

For electron cyclotron resonance (ECR) discharges, a right circularly polarized wave propagates along the dc magnetic field lines to a resonance zone, where the wave energy is absorbed by a collisionless heating mechanism. ECR discharges are generally excited at microwave frequencies (e.g., 2.45 GHz), and the wave absorption requires application of a strong dc magnetic field (875 G at resonance) [88].

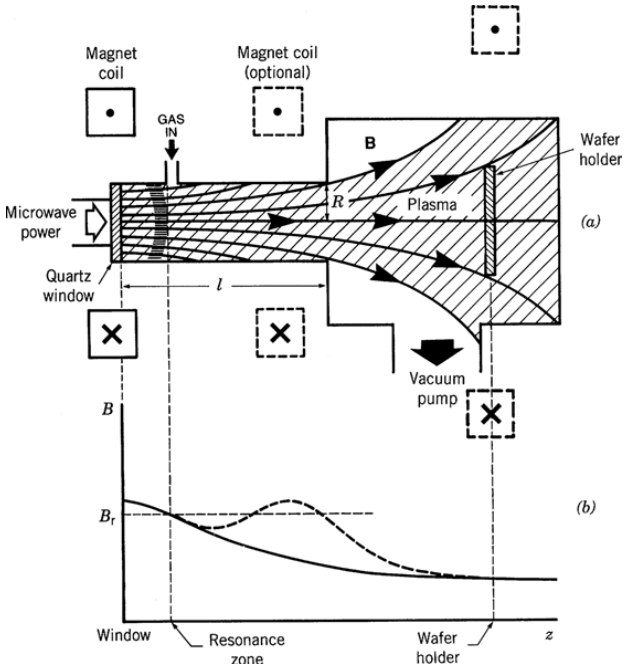

Figure 3.3 A typical high-profile ECR system: (a) geometric configuration; (b) axial magnetic field variation, showing one or more resonance zones [89].

Figure 3.3 shows a typical high aspect ratio ECR system, with the microwave power injected along the magnetic field lines [89]. The power at frequency f =ω/2π is coupled through a vacuum end window into a cylindrical metal source chamber, which is often lined with a dielectric to minimize metal contamination resulting from wall sputtering. One or several magnetic field coils are used to generate a nonuniform, axial magnetic field B(z) within the chamber. The magnetic field strength is chosen to achieve the ECR condition, $\omega_{ce}(z_{res}) = \omega$, where z_{res} is the axial resonance position. When a low-pressure gas is introduced, the gas breaks down and a discharge forms inside the chamber. The plasma streams or diffuses along the magnetic field lines into a process chamber toward a wafer holder. Energetic ions and free radicals generated within the entire discharge region (source and process chambers) impinge on the wafer. A magnetic field coil at the wafer holder is often used to modify the uniformity of the etch or deposition process.

3.1.3. Langmuir probe

The electron density (n_e) and electron temperature (T_e) can be measured by Langmuir probes. A Langmuir probe consists of a bare wire or metal disk (as shown in Figure 3.4),

which is inserted into a plasma and electrically biased with respect to a reference electrode (as shown in Figure 3.5) to collect current-voltage I-V characteristic curve as the applied bias voltage is swept from a negative to a positive potential [90,91].

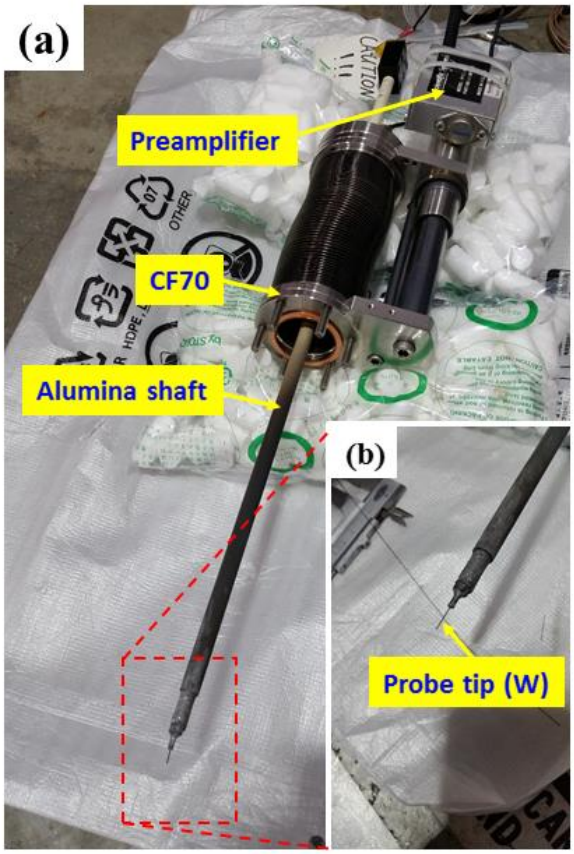

Figure 3.4 A picture of the Langmuir probe used in VEHICLE-1.

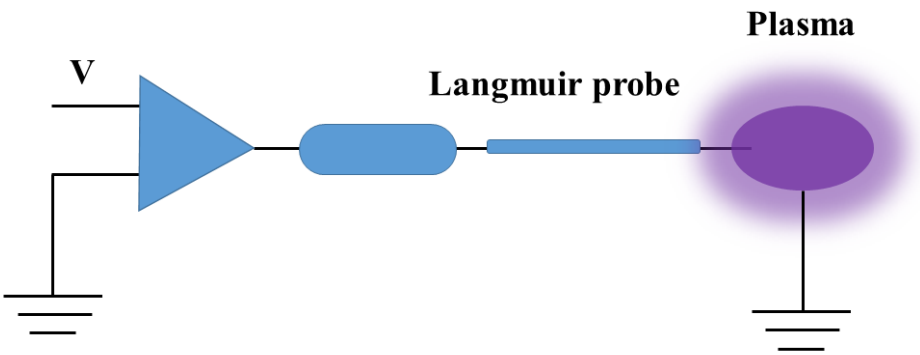

Figure 3.5 A simple Langmuir probe schematic.

The plasma parameters including n_e and T_e can be obtained by analyzing the I-V characteristic curve. The I-V characteristic curve, as described in Figure 3.6, can be divided into three regions [91, 92]: (a) the electron saturation region, (b) the electron retardation region and (c) the ion saturation region.

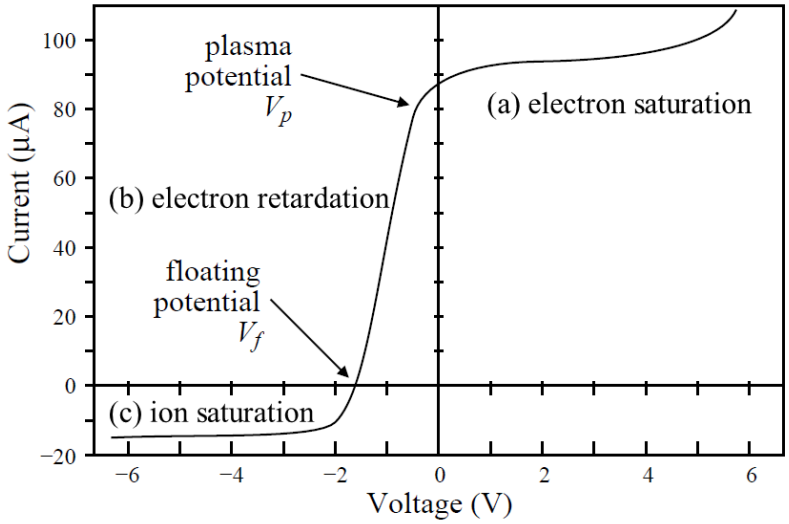

Figure 3.6 A characteristic I-V curve of Langmuir probe [91].

(a) In the electron saturation region the probe is biased positively with respect to the plasma potential. Negative ions and electrons are attracted to the probe and electron saturation occurs.

(b) When the probe is biased negatively with respect to the plasma potential the probe attracts electrons which are energetic enough to overcome the potential barrier. If the electron distribution is in thermal equilibrium the electron current is exponential with respect to the applied voltage and the slope of the exponential region yields the electron temperature.

(c) For increasingly negative potentials with respect to the plasma potential the point is reached where no electrons reach the probe and only positive ions are collected. This region yields the ion number density in the plasma.

The way in which the I-V characteristic is analyzed is vital to the accuracy of the measured plasma parameters. The zero second derivative method is a simple and efficient

analysis routine to calculate the plasma parameters including plasma potential (V_p), floating potential (V_f), electron temperature (T_e) and electron density (n_e).

Plasma potential, V_p: The I-V characteristic goes through an inflection at the plasma potential. At the plasma potential there is no potential between the probe and the plasma and the current measured is due to thermal electrons and ions in the plasma. The inflection point on the I-V characteristic can be accentuated by taking the first and second derivative of the current with respect to the applied voltage. The first derivative goes through a maximum at the plasma potential and the second derivative is equal to zero at the plasma potential.

Floating potential, V_f: The negative potential which develops on a floating probe is known as the floating potential. There is no net current flow through the probe and V_f will repel sufficient electrons to equate the ion and electron fluxes. The voltage point on the I-V curve is the point at which the net current (I) is equal to zero.

Electron temperature, T_e: The electron temperature is calculated by taking the current measured at the plasma potential, $I(V_p)$ and dividing it by the integral of the I-V curve from V_f to V_p, i.e.

$$\frac{I(V_p)}{\int_{V_f}^{V_p} I(V)dv} = \frac{1}{kT_e} \tag{3.1}$$

This method of calculating T_e is less sensitive to noise than the more common technique of calculating T_e by dividing $I(V_p)$ by the derivative of the I-V characteristic.

Electron density, n_e: The electron density is calculated from the current measured at the plasma potential using the following equation:

$$n_e = \frac{I(V_p)}{A_p}\left(\frac{2\pi m_e}{e^2 kT_e}\right)^{\frac{1}{2}} \tag{3.2}$$

where A_p is the area of the probe, m_e is the mass of electron and e is the electronic charge.

3.1.3. Quadrupole mass spectrometer

A mass spectrometer analyzes the composition of chemical substances by means of partial pressure measurement under vacuum. Mass spectrometers are used to analyze gases. Solid or liquid substances can also be analyzed if they are vaporized in an upstream inlet system. The gas is diluted by pumping it down to a low pressure (molecular flow range) in a vacuum chamber and ionizing it through electron bombardment. The ions thus generated are separated in a mass filter according to their charge-to-mass ratio.

Mass spectrometers differ as a result of the wide variety of available versions. The main difference consists of the separating systems. The following four types of mass filters are in widespread use today [93]:

(1) Sector field devices use the deflection effect of a magnetic field on moving charge carriers.

(2) Time-of-flight mass (TOF) spectrometers utilize the differing velocities of molecules of equal energy for the purpose of separation.

(3) In ion traps, the trajectories of the ions are influenced by a high-frequency field.

(4) Quadrupole mass spectrometers utilize the resonance of moving ions in a high-frequency field (similar to ion traps).

For Quadrupole mass spectrometers , the actual analyzer is located in the vacuum and consists of the following components: The ion source ionizes neutral gas particles, which are then separated in the mass filter on the basis of their mass-to-charge ratio *m*/e. The ion current is measured using a Faraday detector or a secondary electron multiplier (SEM) after the ions have left the separating system. The current is a measure of the partial pressure of the respective gas molecules or a measure of fragments that may have been generated in the ion source. A data analysis system processes the ion currents measured with the aid of the detector and presents these currents in various forms.

Quadrupole mass spectrometers utilize the resonance of moving ions in a high-frequency field (similar to ion traps). The filter system of a quadrupole mass spectrometer consists of four parallel rods arranged in the form of a square. Each pair of opposite rods

in Figure 3.7, designated (+) or (-), is connected to each other. Between the two pairs of rods, an electrical voltage consisting of a DC portion U and an AC portion with amplitude V and frequency $f=\omega/2\pi f=\omega/2\pi$ applied. Ideal quadrupole fields require rods that have a hyperbolic profile. In actual practice, however, cylindrcal rods are used, with the rod radius being equal to 1.144 times the field radius r_0 (refer to Figure 3.7 for a definition of the field radius). An electrical quadrupole field is formed between the rods. Ions of varying mass are injected axially into the rod system at approximately equal energy and move through the rod system at uniform velocity. The applied quadrupole field deflects the ions in the X and Y directions, causing them to describe helical trajectories around the Z axis through the mass filter. If the amplitude of the trajectory oscillation is smaller than field radius r_0, the ions reach the detector; if the amplitude exceeds this the ions will discharge on the rods or the surrounding surfaces and will not pass through the filter.

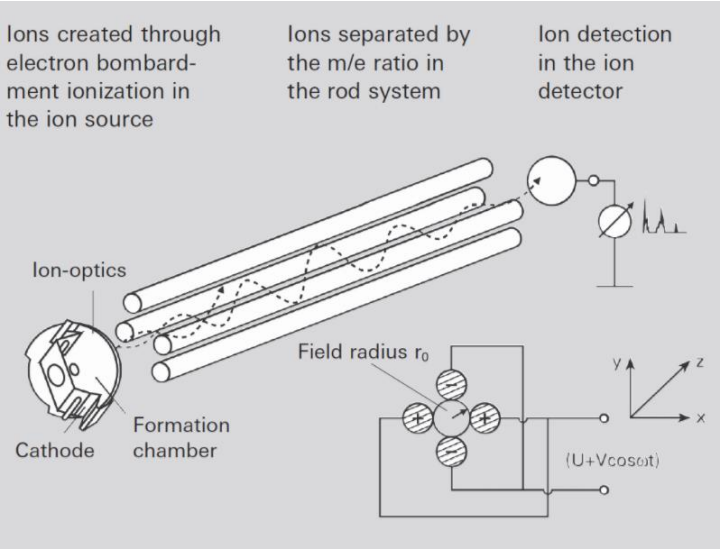

Figure 3.7 The principle of quadrupole mass spectrometer [93].

3.1.4. Spectroscopy and line radiation

The emission spectrum of a chemical element or chemical compound is the spectrum of frequencies of electromagnetic radiation emitted due to an atom or molecule making a transition from a high energy state to a lower energy state. The photon energy of the emitted photon is equal to the energy difference between the two states. There are many

possible electron transitions for each atom, and each transition has a specific energy difference. This collection of different transitions, leading to different radiated wavelengths, makes up an emission spectrum. Each element's emission spectrum is unique. Therefore, spectroscopy can be used to identify the elements in matter of unknown composition. Similarly, the emission spectra of molecules can be used in chemical analysis of substances [94].

In the case of ion beam experiments, assuming that the background level is low, the partial pressure of hydrogen recycled due to reemission and reflection from the target material is generally used as the measure of recycling. In the case of plasma experiments, however, because hydrogen is the feed gas for plasma generation and its partial pressure is rather high, partial pressure measurements would not serve for the same purpose. Therefore, spectroscopic measurements focused on the H_α light have been conducted in the present work. To briefly mention the atomic physics processes related to the H_α spectroscopy, electron impact excitation of hydrogen up to n=/3 followed by relaxation down to n=/2, where n is the principal quantum number, induces photon emission with the particular wave length of 656.3 nm, referred to as H_α light. There are two origins of H_α photons; one from reflected hydrogen atoms; the other from those generated by the dissociation of reemitted molecules. Therefore, one expects that the intensity of H_α light may be used as the measure of hydrogen recycling and is expressed as [95]:

$$I_{H_\alpha} = n_e n_H < \sigma v > \tag{3.3}$$

where H_α is the H_α light intensity, n_e is the electron density, n_H is the atomic hydrogen density, and $< \sigma v >$ is the excitation rate coefficient.

Visible light measurements have been conducted in the VEHICLE-1 device. One finds in Figure 3.8 that the visible light is essentially composed of H_α and H_β emission under the typical experimental conditions (ECR power: ~400 W, hydrogen gas pressure: ~0.1 Pa, DC bias: -100 V). In addition to H_α spectroscopy, the intensities of Ga-I, In-I and Sn-I are monitored to see if the sputtering, evaporation and also "splashing"of $Ga_{67}In_{20.5}Sn_{12.5}$ are taking place under plasma bombardment energized by DC bias. Therefore, the visible light intensity profile to be shown in Chapter 6 is treated as an indicator of hydrogen recycling.

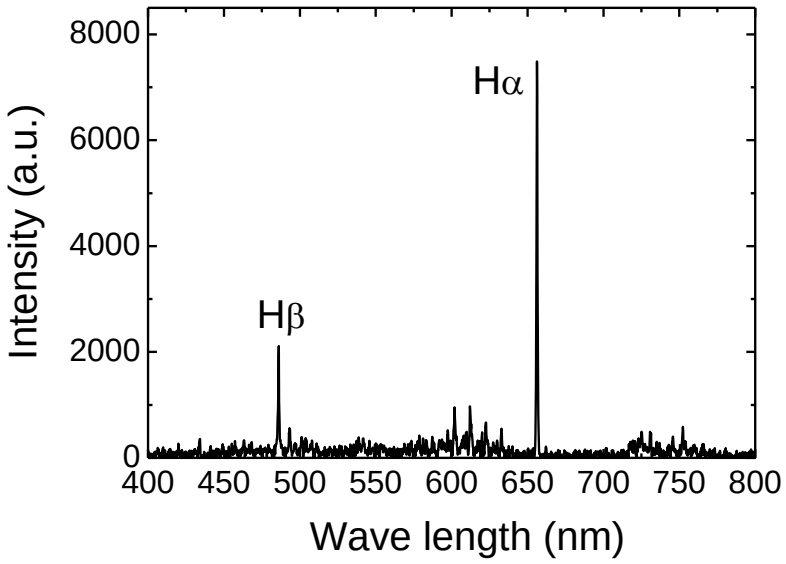

Figure 3.8 Major components in the visible light wave length range (data taken in the VEHICLE-1 device).

3.1.5. The Thermal Desorption Spectroscopy (TDS) facility

Thermal desorption spectroscopy (TDS), also known as temperature programmed desorption (TPD), is the method of observing desorbed molecules from a surface when the surface temperature is increased. When molecules or atoms come in contact with a surface, they adsorb onto it, minimizing their energy by forming a bond with the surface. The binding energy varies with the combination of the adsorbate and surface. If the surface is heated, at one point, the energy transferred to the adsorbed species will cause it to desorb. The temperature at which this happens is known as the desorption temperature. Thus TDS shows information on the binding energy. Since TDS observes the mass of desorbed molecules, it shows what molecules are adsorbed on the surface. Moreover, TDS recognizes the different adsorption conditions of the same molecule from the differences between the desorption temperatures of molecules desorbing different sites at the surface, e.g. terraces vs. steps. TDS also obtains the amounts of adsorbed molecules on the surface from the intensity of the peaks of the TDS spectrum, and the total amount of adsorbed species is shown by the integral of the spectrum. To measure TDS, one needs a mass spectrometer, such as a quadrupole mass spectrometer or a time-of-flight (TOF) mass spectrometer, under ultrahigh vacuum (UHV) conditions. The amount of adsorbed

molecules is measured by increasing the temperature at a heating rate of typically 2 K/s to 10 K/s. Several masses may be simultaneously measured by the mass spectrometer, and the intensity of each mass as a function of temperature is obtained as a TDS spectrum. Shown in Fig 3.9 is a schematic diagram of the Thermal Desorption Spectroscopy (TDS) facility in our laboratory. The sample is heated by infrared introduced from the heater by a quartz rod. The gasses released from the sample are detected by the QMS. Thermal desorption is described based on the Arrhenius equation [96]:

$$r(t) = -\frac{\mathrm{d}\sigma}{\mathrm{d}t} = v_n \sigma^n e^{-E_{\mathrm{act}}/RT} \tag{3.4}$$

where

r(t) the desorption rate[mol/(cm^2 s)];

n order of desorption;

σ surface coverage;

v_n pre-exponential factor [Hz];

E_{act} activation energy of desorption [kJ/mol];

R gas constant;

T temperature [K].

We also assume a linear heating rate:

$$\mathrm{T(t)} = \mathrm{T(0)} + \beta \mathrm{t} \tag{3.5}$$

where β the heating rate in [K/s]; T(0) the start temperature in [K]; t the time in [s].

It is assumed that the pump rate of the system is indefinitely large, thus no gasses will be absorbed during the desorption. Using the Redhead method and the temperature maximum T(m) one can determine the activation energy. By integrating the desorption flux during the heating, the total amount of hydrogen retention in the sample can be obtained.

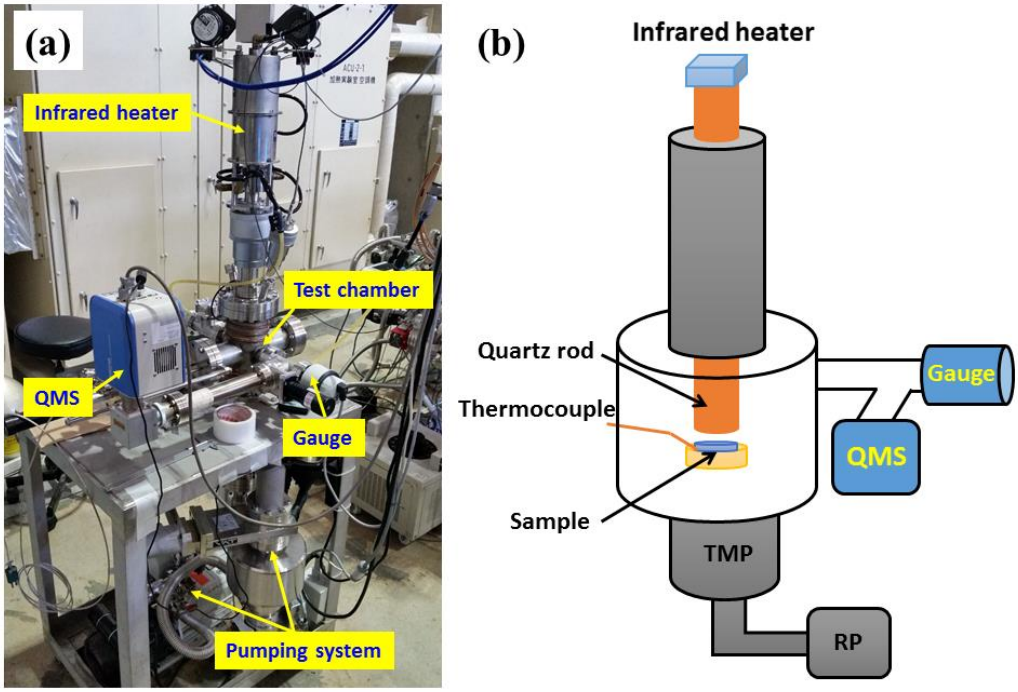

Figure 3.9 (a) A schematic diagram of the Thermal Desorption Spectroscopy (TDS) facility; (b) A sample under heating in TDS.

3.2. Characterization of hydrogen plasmas in VEHICLE-1

The plasma densities and electron temperatures measured by the Langmuir probe are shown in Figure 3.10 as a function of ECR power and in Figure 3.11 as a function of hydrogen neutral gas pressure, respectively. For the ECR power dependence measurements, the hydrogen pressure was maintained at ~0.2 Pa in these measurements. The plasma density increases with increasing ECR power, which, however, is not the case for the electron temperature. In Fig.3.11, the ECR power is fixed at 200 W. The plasma density increases with increasing hydrogen gas pressure while the plasma temperature shows an opposite trend.

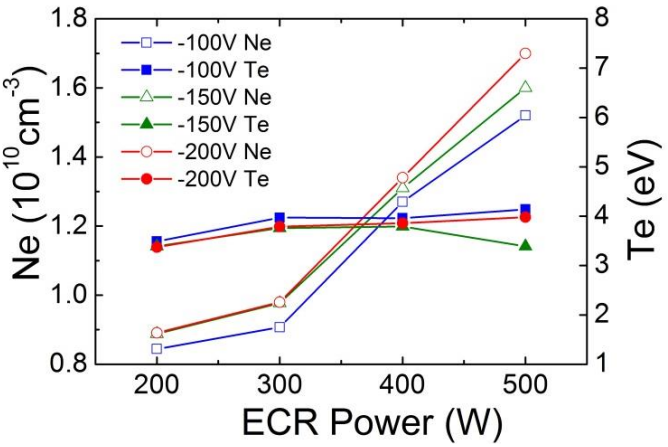

Figure 3.10 Plasma density and electron temperature as a function of ECR power[73].

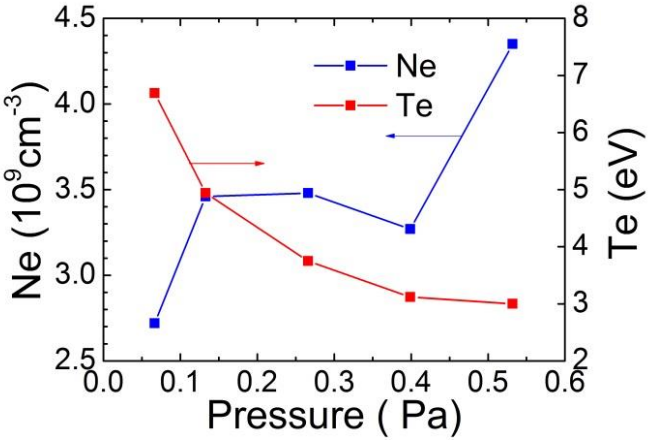

Figure 3.11 Plasma density and electron temperature as a function of hydrogen pressure[73].

Shown in Fig.3.11 is one calculation result using the zero-dimensional model [73]. In this calculation, the electron density is set at 1×10^{10} cm^{-3} and the atom reflection coefficient R is assumed to be 0.9. The ion confinement time τ_i for H^+ is estimated to be ~200 μs according to the plasma parameters and dimension of the VEHICLE-1 facility. The ion confinement time for other species are estimated by assuming τ_i is proportional to the square root of the ion mass. The electron temperature and density data used in the calculation are taken by Langmuir probe measurements. For ECR discharges in laboratory-sale facilities, usually $T_e >> T_i$ holds. The ion temperature is assumed to be 0.1 eV, which is the lower temperature limit of the available database [97].

The modelling results indicate that H_3^+ is the dominant ion species at the electron temperature and neutral hydrogen gas pressure (~0.1 Pa) in our experiments. The concentration of H^+ increases with the increase of electron temperature and becomes the dominant species when the electron temperature is higher than 4 eV.

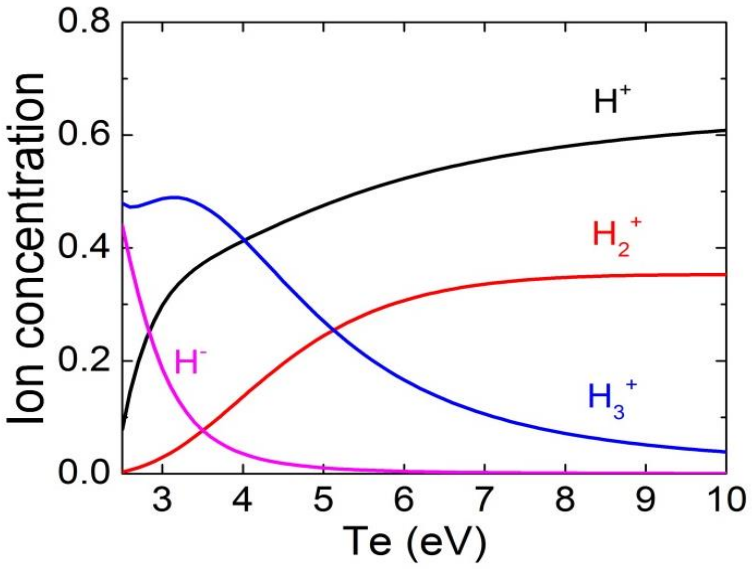

Figure 3.12 Estimation of the ion species mix using the zero-dimensional model [73].

Then the net implantation flux, $J_{0,}$ at the applied bias voltage into a membrane can be expressed in the following manner:

$$J_0 = \sum_{j=1}^{3} \frac{(1-\gamma_k)\, jN_k}{2} \sqrt{\frac{k_B(T_e + T_i)}{m_{H_j^+}}} \tag{3.6}$$

where k_B is the Boltzmann constant, T_e and T_i ($T_i \approx 0$) are the electron and ion temperatures, respectively, and γ_k is the ion reflection coefficient calculated from the Monte Carlo program, SRIM (See Fig.2.2 in Chapter 2). The net implantation is estimated to be of the order of 10^{15} ~10^{16} H/cm^2/s.

Generally, the edge plasma density in the scrape-off layer (to be referred to as SOL) of a magnetic fusion device is of the order of 10^{13} /cm^3 and the cross-field diffusion coefficient is typically of the order of 10^3 cm^2/s. Assuming that the thickness of the SOL is a few cm, the cross-field particle flux to the first wall may be estimated to be of the order of 10^{16} H/cm^2/s. It is thus believed that the plasma bombardment conditions in VEHICLE-1 are relevant to those to be seen in the first wall environment of fusion reactors.

3.3 The permeation experimental setup

Three types of permeation setups have been developed in our laboratory. For Type **A**, the membrane samples are prepared in the same dimensions as those commercially available conflat flanges with an outer diameter of 70 mm, except that a circular area of ~35 mm in diameter inside the knife-edge is machined down to thicknesses of 0.5 mm to 5 mm to use as permeation membranes, as shown in Figure 3.13. This type of setup provides a good sealing for permeation experiments, especially for high pressure gas-driven permeation(GDP) experiments. Hydrogen transport parameters for α-Fe and F82H have been evaluated by using this type of permeation setup in Vehicle-1[73].

For Type **B**, the membrane samples are clamped on a flange by using a press-on ring with a knife-edge, as shown in Figure 3.14. The outer periphery of the press-on ring and the inner periphery of the flange are machined to screw thread structures, so they can be connected with each other. This type of setup is not suitable for high pressure GDP due to the small gap between the screws. While for PDP and low pressure GDP(< 10 Pa), the leakage flux is negligible compared to the permeation flux. Hydrogen GDP and PDP through titanium membranes are conducted by using this type of setup.

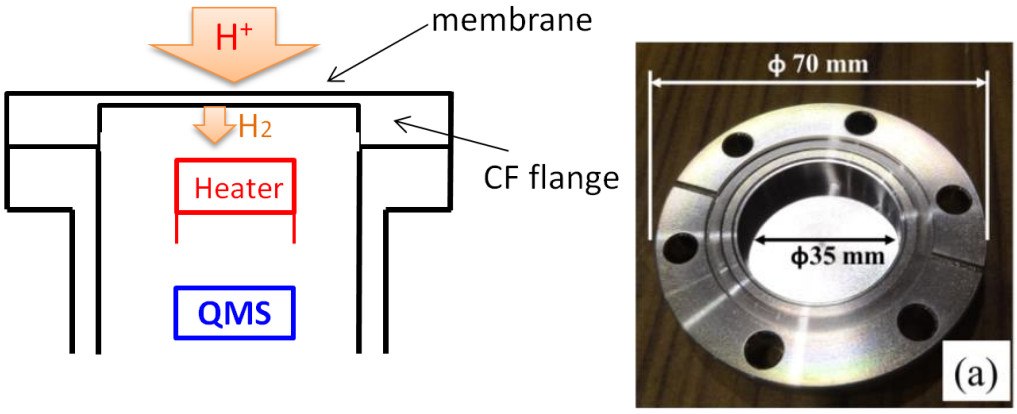

Figure 3.13 A schematic diagram of the permeation membrane for type a.

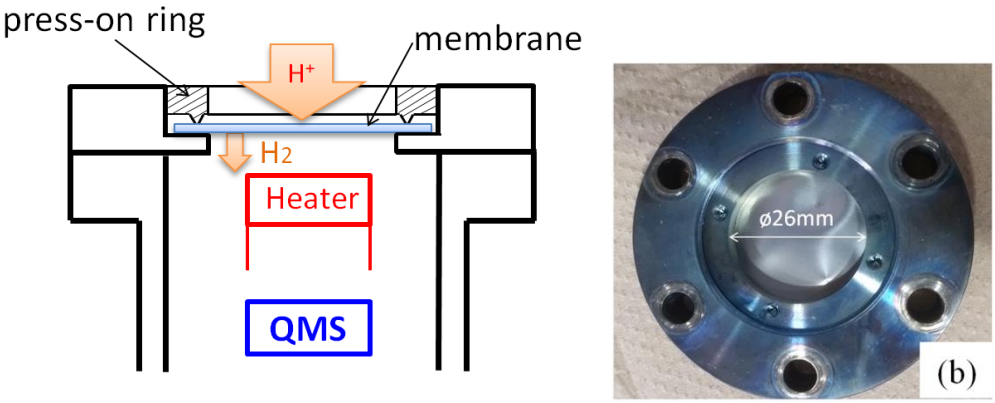

Figure 3.14 A schematic diagram of the permeation membrane for type b.

Type **C** is specifically developed for gases permeation through liquid metals, by using the mesh-surface tension method, as shown in Figure 3.15 [98]. A liquid metal is sitting on a mesh sheet held by surface tension. The mesh openings allow the downstream surface of the liquid to be exposed to a vacuum. The upstream chamber and the downstream chamber are seprated by the liquid. The mesh sheet is made of stainless steel and it is pressed on a flange by using bolts. Hydrogen isotopes PDPs through liquid Li, GaInSn and Ga are conducted by using this type of setup.

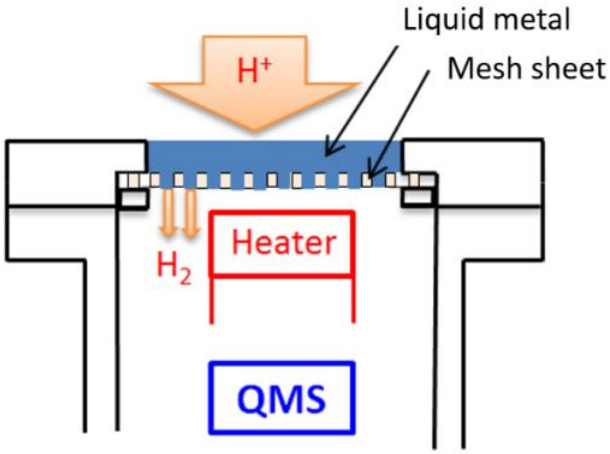

Figure 3.15 A schematic diagram of the permeation setup for type c. It is specifically developed for gas permeation through liquid metals

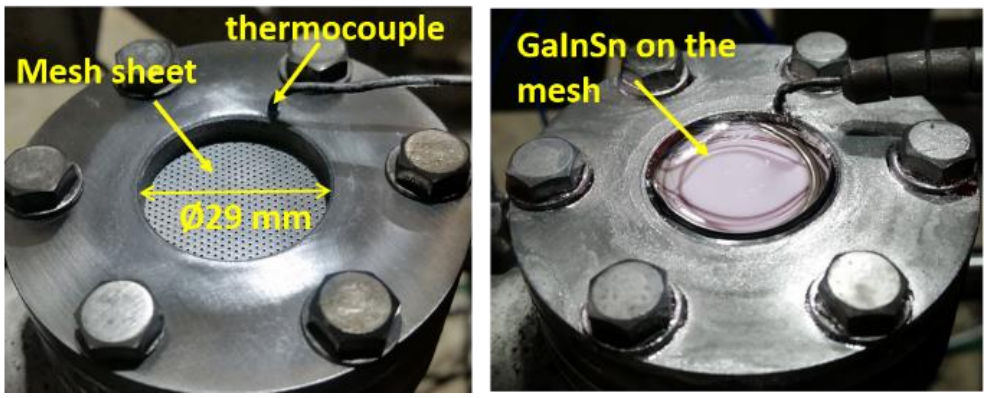

Figure 3.16 A liquid GaInSn sample is sitting on the mesh sheet held by surface tension.

3.4. The mesh-surface tension method

The use of a sheet mesh to hold a liquid metal sample is based on the assumption that surface tensions of liquid metals are relatively high. Shown in Figure 3.17 is the temperature dependence of surface tension data for some liquid metals [99,100]. People might see small drops of water being suspended on a tap, which is held by surface tension of the water. The surface tension for liquid metals decrease as the temperature increases, but they are still much higher than water at room temperature. To avoid liquid metal

dropping down through the mesh openings, upward force provided by the surface tension should be larger than the weight of liquid metal and pressure difference caused by gases in upstream chamber. Shown in Figure 3.18 is the stress balance on liquid lithium set on the mesh, which can be described by:

$$\sin\theta \times 2\pi R\sigma = \pi R^2\left(P_{H2} + \rho g d\right),\ 0^o < \theta < 90^o \tag{3.7}$$

where σ is the surface tension of the liquid metal, R is the radius the pore, d is the thickness of the liquid, ρ is the density, and P_{H2} is neutral gas pressure in the upstream chamber, θ is the angle between the direction of surface tension and horizontal line. Shown in Figure 3.19 is the angle θ depending on the gas pressure in the upstream chamber for a constant liquid depth of 5mm. It is easy to image that as the pressure increases, θ will increase. If $\theta = 90^o$, the liquid will drop down through the mesh openings. Under this condition, the critical pressure to avoid the penetration has been determined. For a 4mm thick liquid GaInSn, the maximum pressure difference to avoid liquid dropping down could be ~5286 Pa at 500°C, while the typical hydrogen gas pressure in the upstream chamber for running plasma is only ~0.1 Pa. For liquid lithium with thickness of 2mm at 500 ◦C, surface tension, σ, is 0.356 N/m. Then θ will be 0.17◦ calculated from Equation 3.17, which suggests that the surface tension is sufficient to hold liquid lithium.

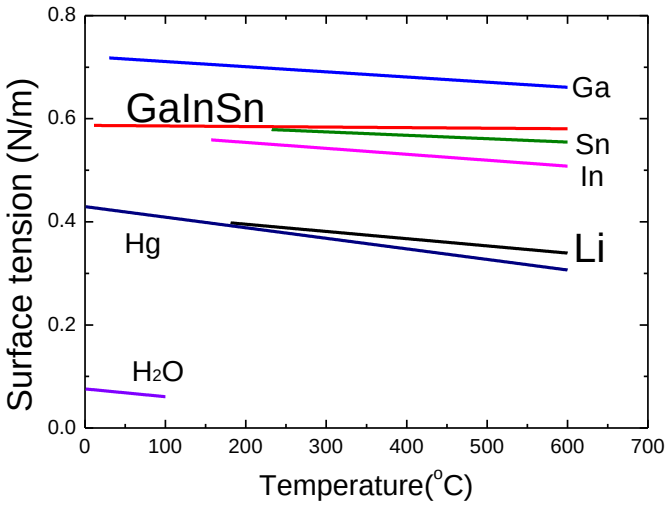

Figure 3.17 Surface tension of some liquids [99,100].

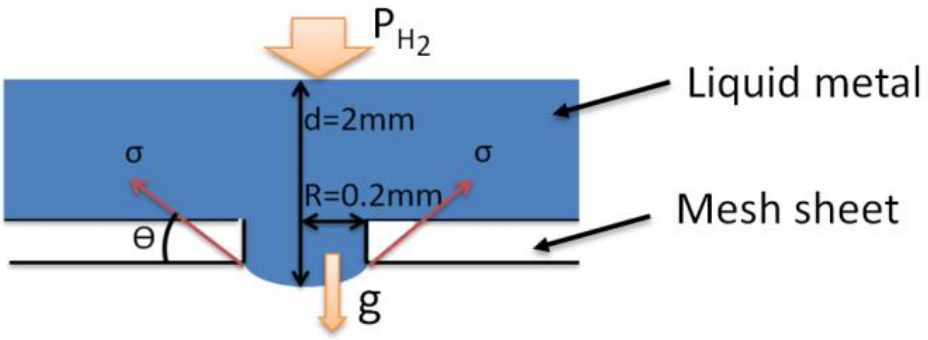

Figure 3.18 A schematic diagram of the surface tension to hold a liquid metal on the mesh sheet.

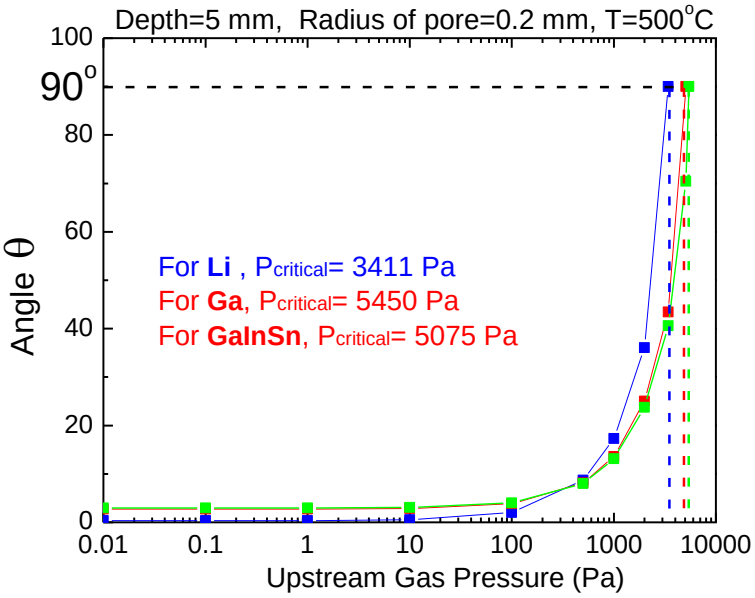

Figure 3.19 The relations between the angle θ and the gas pressure in the upstream chamber.

3.5 The samples preparation

Shown in Figure 3.20 is the liquidus surface of Ga-In-Sn alloys, it is found that this eutectic alloy has a lowest melting point of 10.5^{o}C with the composition of 67% Ga, 20.5% In, and 12.5% Sn in w.t%. $Ga_{67}In_{20.5}Sn_{12.5}$ is liquid at room temperature, and it has low chemical reactivity. In this thesis, it is employed as a surrogated material to study the properties of liquid metals. Shown in 3.21 are the vapour pressures of four liquid metals (Li, Ga, In and Sn). Shown in Figure 3.22 is the energy dependence of the physical sputtering yield for Ga, In, Sn and Fe, calculated by using the EDDY code.

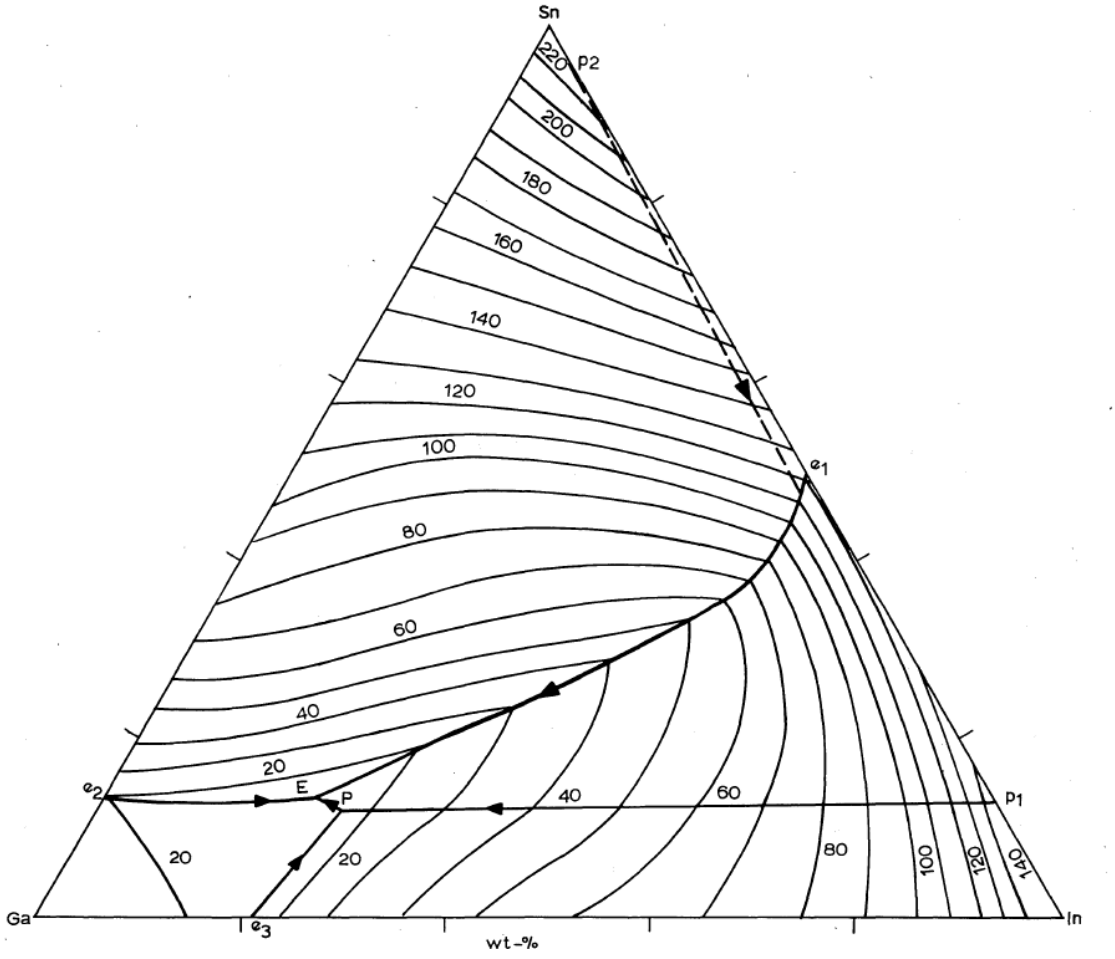

Figure 3.20 The liquidus surface of Ga-In-Sn alloys, ^{o}C[36].

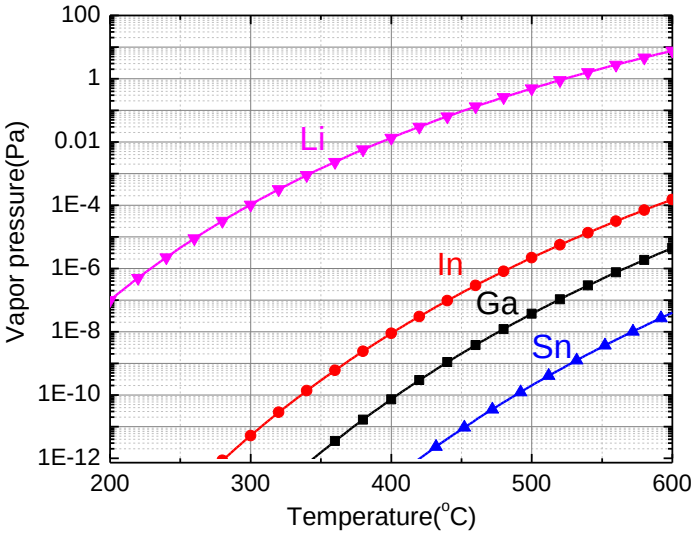

Figure 3.21 Vapour pressure of four liquid metals (Li, Ga, In and Sn) as a function of temperature[36].

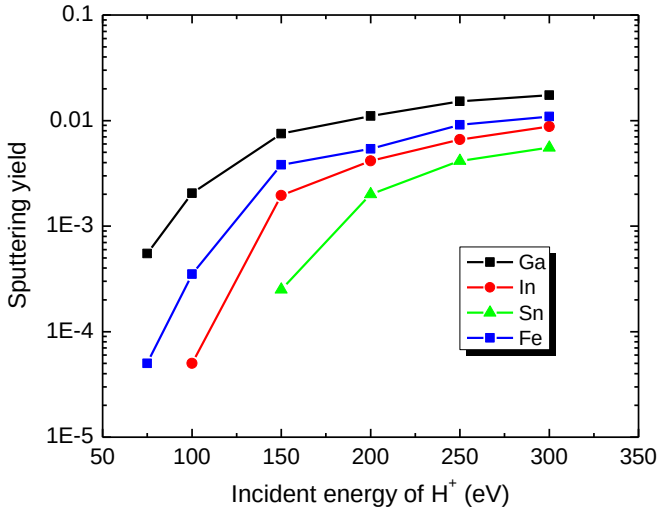

Figure 3.22 Energy dependence of the physical sputtering yield for Ga, In, Sn and Fe, calculated by using the EDDY code.

3.6. Summary

In this chapter, the experimental setup for plasma-driven permeation through liquid metals has been introduced. The experiments on plasma-driven permeation plasma are conducted in a linear plasma facility VECHICLE-1. The system of VECHICLE-1 and the plasma parameters have been described.

The mesh-surface tension method has been developed to hold a liquid metal on a mesh sheet. The liquid metal separates the upstream chamber and the downstream chamber. The upstream surface of the liquid is exposed to the plasma, then the hydrogen atoms diffuse to the downstream surface and are released to the downstream chamber through the mesh openings.

The main diagnostic instruments in VECHICLE-1 are the Langmuir probe, the Quadrupole mass spectrometer, and the visible spectroscopy. The plasma parameters are measured by the Langmuir probe; the hydrogen permeation fluxes are measured by the Quadrupole mass spectrometer; and the hydrogen recycling behavior is measured by the visible spectroscopy. The deuterium static retention in the samples are measured by the thermal desorption spectroscopy (TDS) facility.

Chapter 4 Hydrogen isotopes plasma-driven permeation through liquid metals

Hydrogen and deuterium plasma-driven permeation (PDP) through liquid metals, including lithium, GaInSn and Gallium have been systematically investigated using a steady state laboratory-scale plasma device: VEHICLE-1. An innovative method to hold the liquid samples has been developed for running PDP through liquid metals. Hydrogen gas-driven permeation (GDP) and PDP for a solid metal, titanium, has also been investigated as a pilot study, because titanium and lithium are both hydride forming metals. Hydrogen isotopes transport parameters have been measured for these metals. The hydrogen isotopes dynamic and static retention have been investigated as well. Based on these results, evaluation of hydrogen isotopes transport and retention in liquid metal PFCs would be possible for reactor design studies.

4.1. Hydrogen PDP though solid titanium

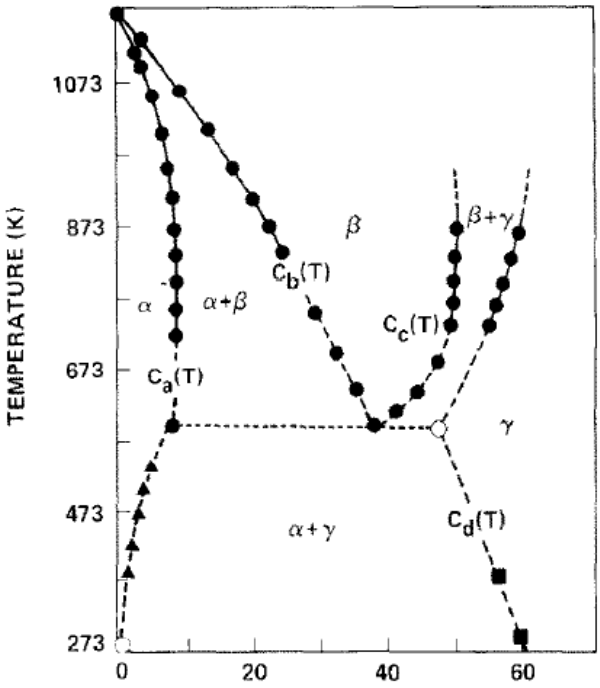

Figure 4.1 The phase diagram of the titanium-hydrogen system.

To investigate hydrogen PDP through liquid lithium, it is realized that liquid lithium is not only difficult to handle in a PDP experiment, but also the Li-H system is complicated.

It is found that titanium and lithium are both hydride forming metals, and both of them have a strong ability for absorbing hydrogen gases. From the phase diagram of the Ti-H system, as shown in Figure 4.1, it is found that phase transformation may take place if the hydrogen concentration exceeds the phase boundary. In GDP experiments for titanium membranes, it is found that gas-phase hydrogen transport through α-phase titanium between 400◦C and 800◦C is influenced by surface reactions and is not controlled by hydrogen diffusion through the titanium lattice [101, 102]. These findings suggest that hydrogen PDP through liquid lithium may also be influenced by surface reactions. Since no examples of PDP experiment through lithium or titanium exist in the literature, it is proper to investigate hydrogen PDP through titanium as a pilot study to explore PDP through hydride forming metals.

4.1.1 Hydrogen PDP through Ti

For hydrogen PDP through titanium, the membranes are clamped on a flange by using a press-on ring with a knife-edge, as shown in Fig.3.14. The temperatures of the membrane are measured by a thermocouple attached on the upstream surface. Hydrogen PDP experiments for 0.1mm and 1mm thick titanium membranes have been conducted in the temperature range from 331 to 532◦C. Shown in Figure 4.2 is the temperature dependence of steady state PDP fluxes through 0.1mm and 1mm titanium membranes. It is shown that the steady state permeation fluxes increase as the temperature increases. And there is no obviously thickness effect on the steady state PDP fluxes, even though the thickness difference is one order of magnitude. Then, it is concluded that hydrogen PDP through titanium under these conditions is surface recombination limited, which is referred to be in R-R regime based on the steady state PDP model. For PDP in the R-R regime, the hydrogen concentration in the membrane is uniform at steady state.

In these PDP experiments, the hydrogen implantation flux $J_0 = 6 \times 10^{15}$ H/cm^2/s and the steady state permeation flux $J_+ = 1 \times 10^{13} \sim 2 \times 10^{15}$ H/cm^2/s. For the reemission flux $J_- = J_0 - J_+$, it is calculated that the permeation flux is much less than the reemission flux.

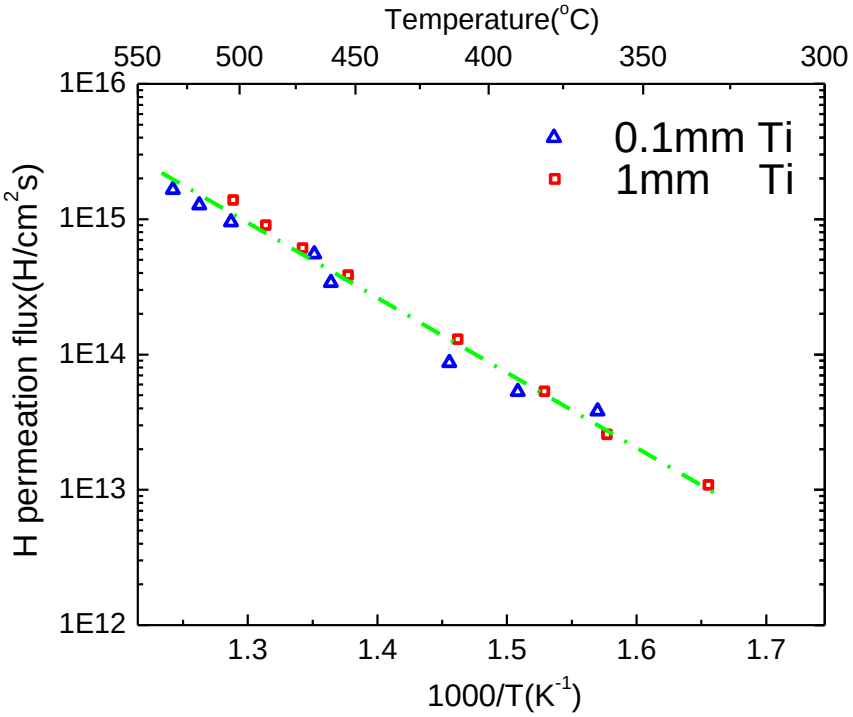

Figure 4.2 Hydrogen steady state PDP fluxes through titanium membranes with thickness of 0.1mm and 1 mm.

$$J_+ = K_r \cdot C^2 \tag{4.1}$$

$$J_- = K_r' \cdot C^2 \tag{4.2}$$

where C is hydrogen concentration in the membrane; K_r is the recombination coefficient at the back surface (without plasma bombardment); K_r' is the recombination coefficient at the front surface (with plasma bombardment).

For the titanium membrane in PDP experiments, the downstream surface is essentially a virgin surface, while the morphology of the upstream surface maybe modified by plasma bombardment [73]. Since C, K_r and K_r' are all unknown, it is not possible to evaluate their values only from the PDP experimental data. And it is found that for the case of GDP in the R-R regime, the permeation flux $J_+$is given by:

$$J_+ = \frac{1}{2} K_r \cdot K_S^2 \cdot P \tag{4.3}$$

Where K_r is the surface recombination coefficient of a virgin surface; K_S is Sieverts' constant, which is available in the literature; and P is the gas pressure in the upstream chamber. In Equ.4.3, only K_r is unknown, while J_+ and P are measureable. In order to evaluate K_r, hydrogen GDP experiments for titanium membranes have been conducted and the results are shown in the following section.

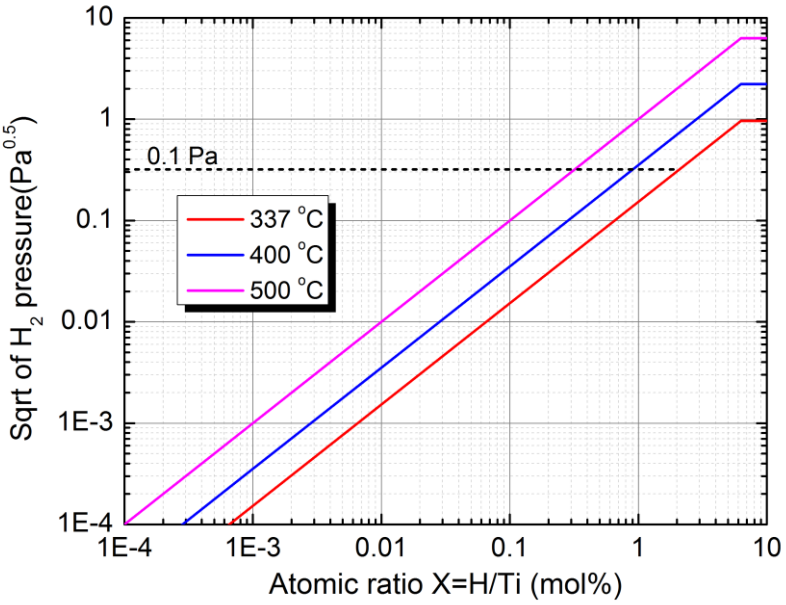

Figure 4.3 Pressure-Concentration-Temperature (PCT) diagram of Ti-H system[104].

4.1.2 Hydrogen GDP through Ti

Consider a metallic surface to be reacting with gaseous hydrogen of pressure P in an isolated system [103] held at the temperature T in the manner:

$$\mathrm{M} + \mathrm{H_2(gas)} \rightleftharpoons \mathrm{MH_2} \tag{4.4}$$

The rate of increase in the amount of dissolved hydrogen in the metal, (dx/dt), is given by

$$\frac{dx}{dt} = v\Gamma(P) - K_r \cdot C^2 \tag{4.5}$$

where $\Gamma(P)$ is the H_2 arrival rate to the surface, which is proportional to the hydrogen gas pressure P; v is the sticking coefficient; K_r is hydrogen recombination coefficient; C is the dissolved hydrogen concentration in the metal. When this metal-hydrogen reaction

system reaches its thermodynamic equilibrium, the following relations are automatically established

$$v\Gamma(P) = K_r \cdot C^2 \tag{4.6}$$

And the hydrogen concentration, *C*, can obtained by the equilibrium hydrogen pressure *P* in the PCT diagram of a Ti-H system. The relation is defined as

$$C = K_S \sqrt{P} \tag{4.7}$$

Where K_S is Sieverts' constant.

$$v\Gamma(P) = K_r \cdot C^2 = K_r(K_S \sqrt{P})^2 \tag{4.8}$$

Hydrogen GDP experiments through titanium membranes have been conducted by using the same permeation setup for PDP. Hydrogen gas pressure in the upstream chamber for GDP is 1.0Pa, which guarantees that the Ti-H system is in α-phase, as shown in Figure 4.3[104]. Hydrogen GDP experiments for 0.1mm and 1mm thick titanium membranes have been conducted in the temperature range from 376 to 490 ◦C. Shown in Figure 4.4 is the temperature dependence of steady state GDP fluxes through 0.1mm and 1mm titanium membranes. It is shown that the steady state permeation fluxes increase as the temperature increases. And there is no obvious thickness effect on the steady state GDP fluxes. Then, it is concluded that hydrogen GDP through titanium under these conditions is limited by surface reactions. And hydrogen concentration in the membrane is uniform at steady state, which is similar to the R-R regime in the PDP model.

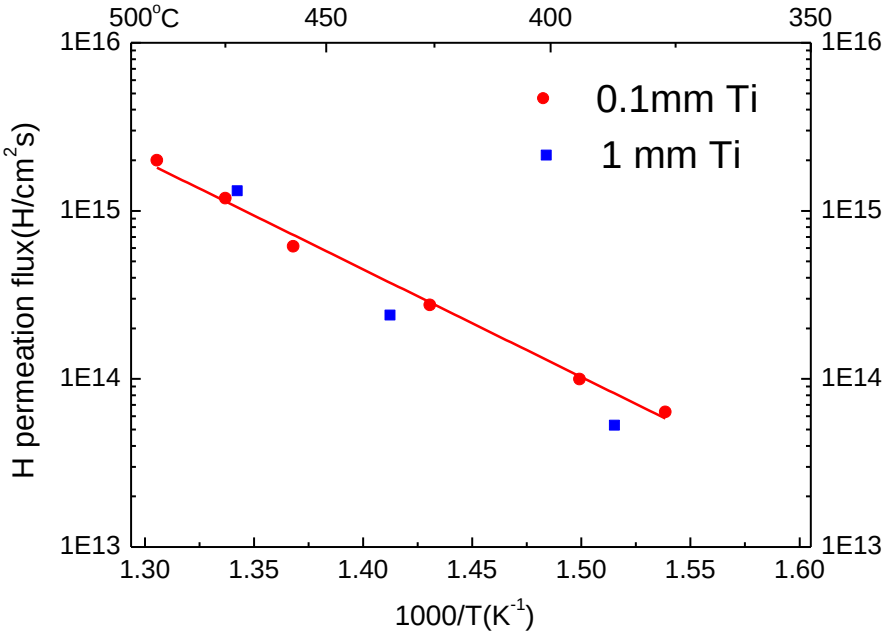

Figure 4.4 Hydrogen steady state GDP fluxes through titanium membranes with thickness of 0.1mm and 1 mm.

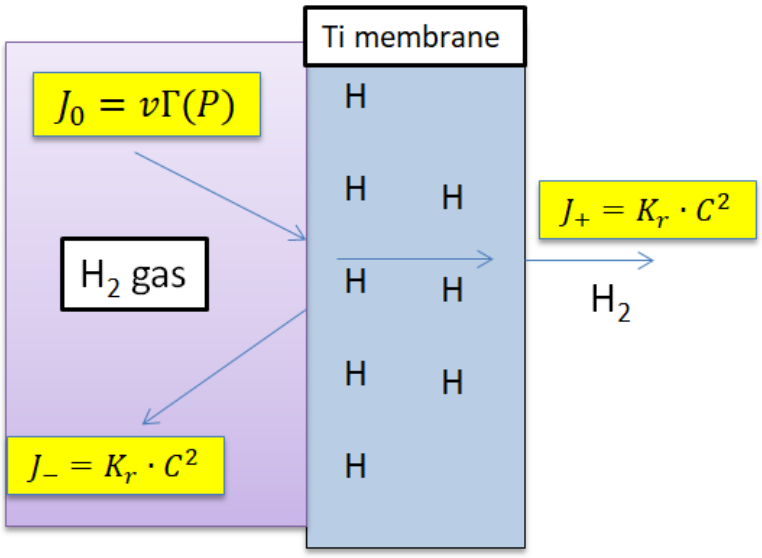

Figure 4.5 The process of hydrogen gas-driven permeation through a titanium membrane.

Shown in Figure 4.5 is the process of hydrogen gas-driven permeation through a titanium membrane. J_0 is the incoming hydrogen flux that dissolved in the membrane, J_+ is the permeation flux from the downstream surface, and J_- is the reemission flux from the

upstream surface. In GDP experiments, both surfaces are essentially virgin surfaces. So it is assumed that the surface recombination coefficients for both surfaces are the same. Thus, there is the following relation:

$$J_+ = J_- = \frac{1}{2}J_0 = \frac{1}{2}v\Gamma(P) \tag{4.9}$$

Take Eq.4.8 into Eq.4.9, then J_+ can be given as following:

$$J_+ = \frac{1}{2}K_r \cdot K_S^2 \cdot P \tag{4.10}$$

Since J_+ and P are measurable, and K_s is available in the literature, then K_r can be derived. The result of K_r is shown in Figure 4.6, which is found to be about 4 orders of magnitude smaller than the only existing data [68]. This data is a theoretical calculation assuming the sticking coefficient, v, to be 1. Generally, the sticking coefficient is much smaller than 1. For example, the hydrogen sticking coefficient on titanium has been found to be $v = 2 \times 10^{-4}$ at 277°C [105]. From Eq.4.8, it is found that K_r is proportional to v. So the K_r data obtained in the GDP experiment is reasonable.

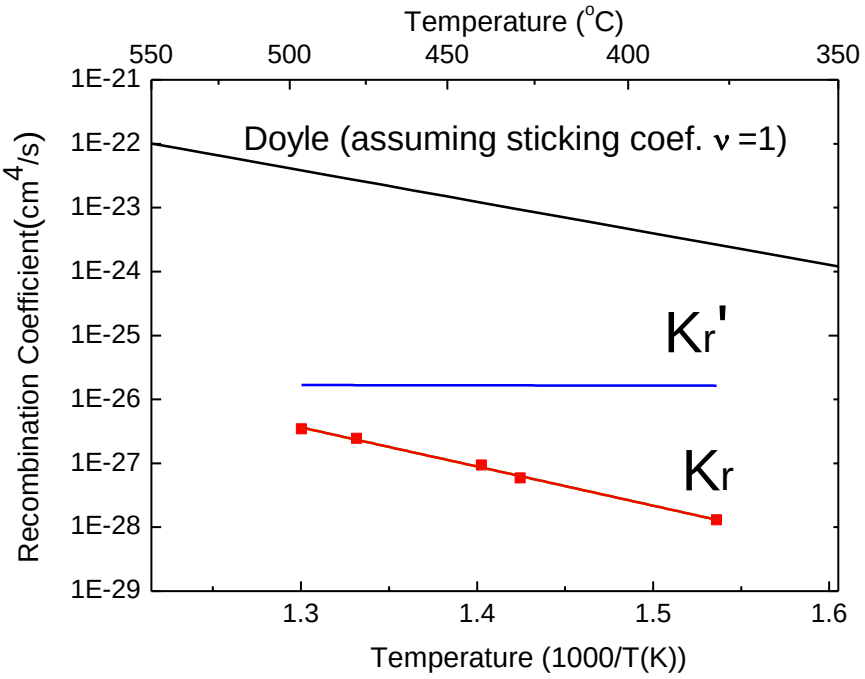

Figure 4.6 Hydrogen surface recombination coefficient for titanium. K_r is for the surface without plasma bombardment ; K_r' is for the surface with plasma bombardment.

4.1.3 Hydrogen concentration in Ti during PDP

Inserting K_r data into Eq.4.1 and Eq.4.2, then the hydrogen concentration, C, in the membrane during PDP, and the surface recombination for the front surface, $K_{r,}'$ have been obtained. It is shown in Fig.4.6 that K_r' is larger than Kr, which suggests that the surface recombination coefficient is increased under plasma bombardment for titanium. The calculation results of the hydrogen concentration, C, in titanium during hydrogen PDP are shown in Fig.4.7, which are found to be ~1 at.%. The phase boundary of the α-phase is ~7 at.% [106]. So it is concluded that there is no phase transformation during the PDP experiments.

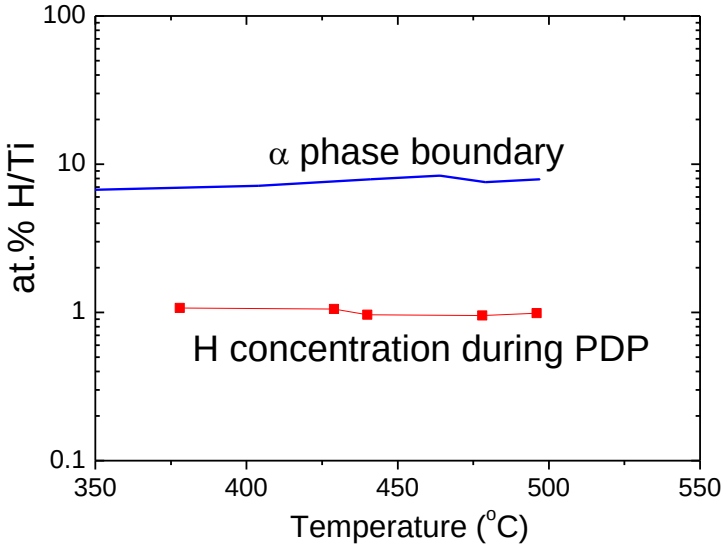

Figure 4.7 Hydrogen concentration in titanium during PDP.

4.2. Hydrogen isotopes PDP through liquid lithium

4.2.1 Hydrogen and deuterium PDP through liquid lithium

Hydrogen and deuterium PDP experiments with liquid lithium have been conducted in the temperature range from 313 to 402°C. Shown in Figure 4.8 is the time evolution of hydrogen PDP flux through 2mm deep liquid lithium at 332°C. Shown in Figure 4.9 is the temperature dependence of the steady state hydrogen PDP fluxes through 2mm deep liquid lithium.

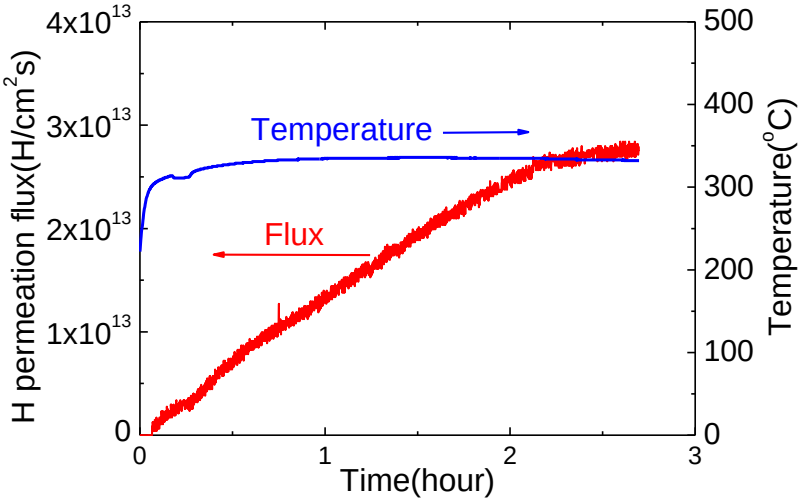

Figure 4.8 Time evolution of hydrogen PDP flux through 2mm deep liquid lithium at 332°C.

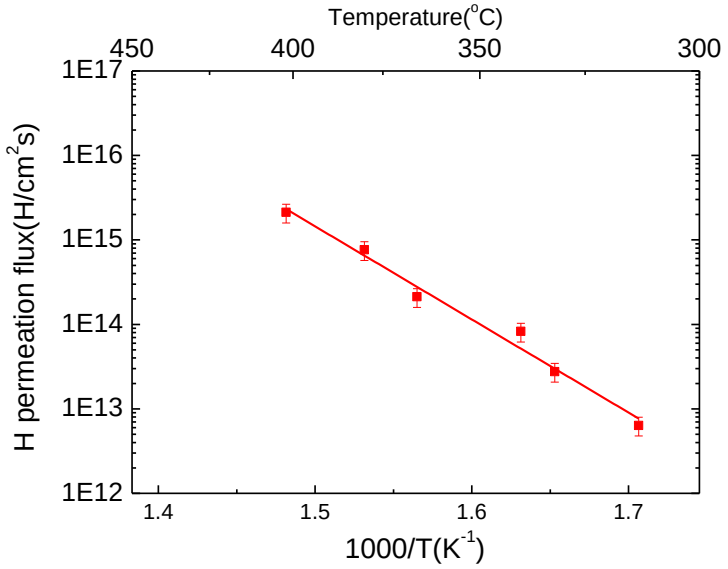

Figure 4.9 Temperature dependence of the steady state hydrogen PDP fluxes through 2mm deep liquid lithium.

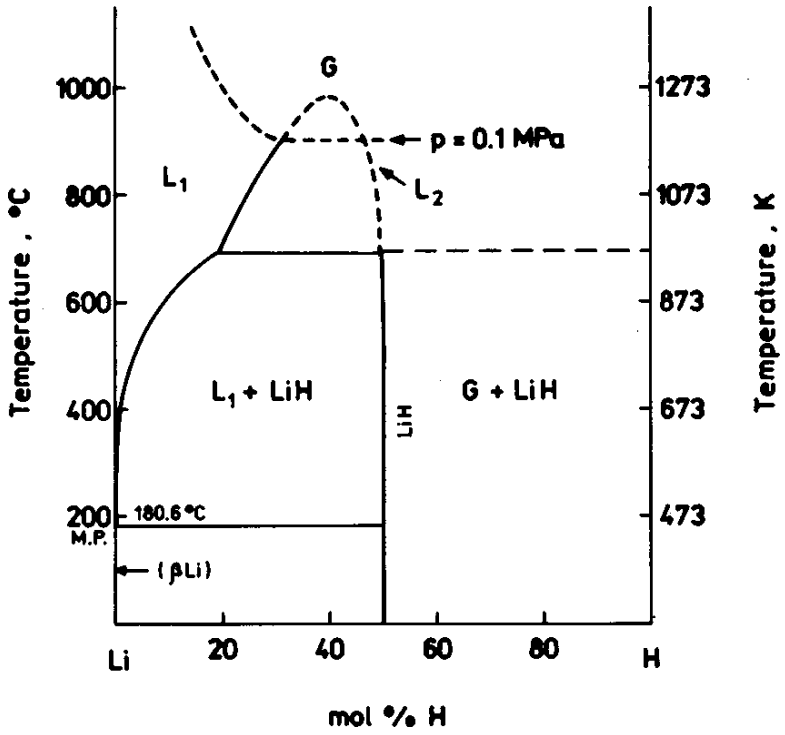

Figure 4.10 The phase diagram of the Li-H system [107].

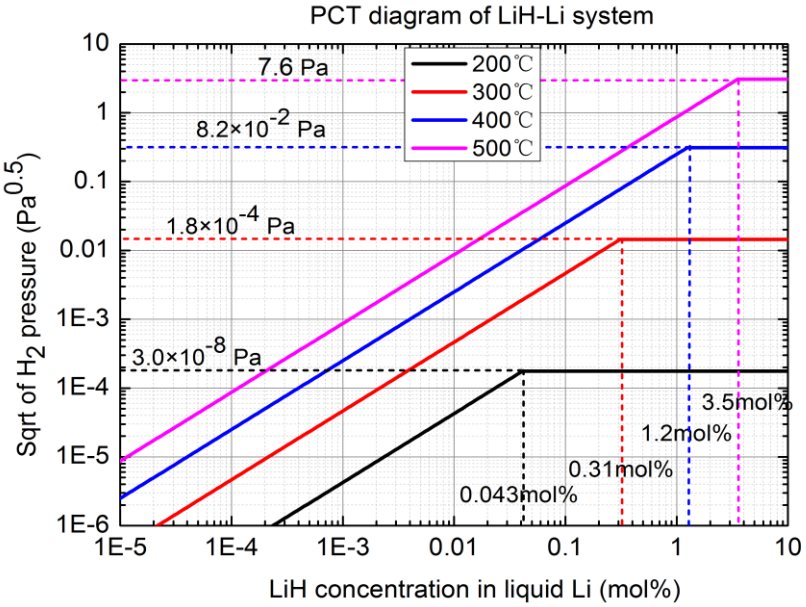

Figure 4.11 Pressure-Concentration-Temperature (PCT) diagram of Li-H system [107].

The Pressure-Concentration-Temperature (PCT) diagram of the LiH-Li system has been obtained based on the data evaluated by H. Borgstedt [107], as shown in Figure 4.11.

The equilibrium pressure of LiH-Li in the temperature range from 313 to 402°C is from 4.5×10^{-4} Pa to 9.1×10^{-2} Pa. And the corresponding hydrogen solubility limit is from 1.76×10^{20} H/cm^3 to 5.82×10^{20} H/cm^3, taken from the PCT diagram. The pressure in the upstream chamber (0.1 Pa) for running plasma is higher than the equilibrium pressure of LiH-Li, so there is no reemission flux at the upstream surface of lithium. And the measured hydrogen permeation flux at steady state is in the range from 6.36×10^{12} H/cm^{2}s to 2.12×10^{15} H/cm^{2}s, which is less than the upstream implantation flux. Therefore the dissolved hydrogen concentration in lithium will always increase until solid LiH starts to precipitate at the upstream surface, meaning the LiH-Li system will transform from the $\boldsymbol{\alpha}_{liq}$ phase to the $\boldsymbol{\alpha}_{liq}+\boldsymbol{\beta}_{sol}$ phase. Then the dissolved hydrogen concentration at the upstream surface is fixed to be the hydrogen solubility limit.

In the experiment, the steady state permeation flux is established within 3 hours, which shows a big difference compared with the time lag, t_{lag}, based on the assumption of diffusion-limited PDP. So hydrogen PDP through liquid lithium is not diffusion limited but recombination limited, which has been found in titanium as well.

For recombination limited PDP, the hydrogen concentration at the downstream surface is approximately the same as the dissolved hydrogen concentration at the upstream surface when the steady state permeation flux is established. Then the recombination coefficient K_r can be obtained by the equation：

$$K_r = {}^{J}/_{C_s^2} \tag{4.11}$$

Where J is the steady state PDP flux and C_s is the dissolved hydrogen concentration at the downstream surface.

The temperature dependence on the hydrogen recombination coefficients has been obtained, which is close to the deuterium recombination coefficients in liquid lithium [108], as shown in Fig.4.12.

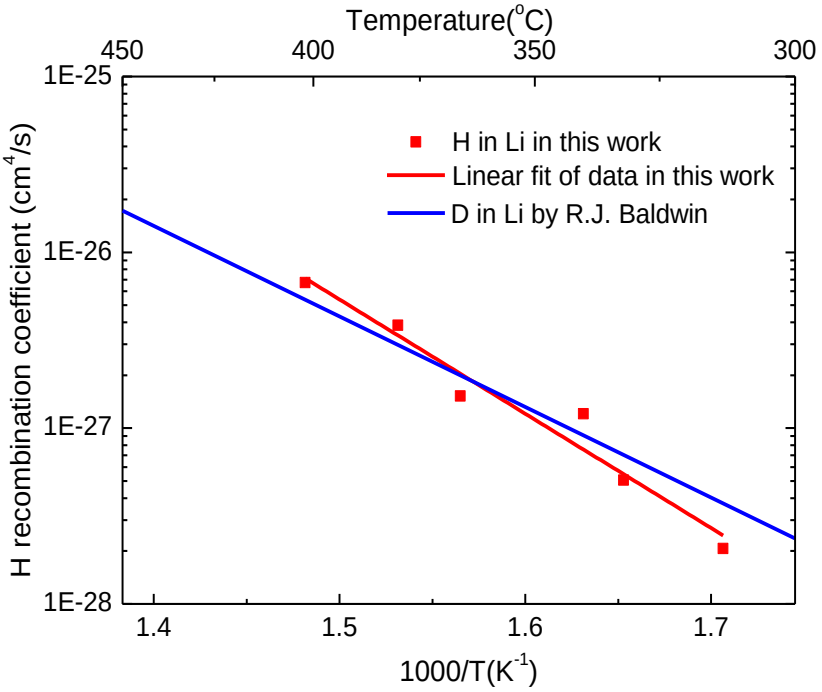

Figure 4.12 Hydrogen recombination coefficients for liquid lithium.

4.2.2 Simulation result on hydrogen transport in liquid lithium

The simulation results of permeation flux with different diffusivity values in Fig.4.13 show that diffusivities in the orders of 10^{-5}-10^{-3} cm^2/s are all close to the experimental data. As diffusivity plays a minor role in a recombination limited PDP, to get precise diffusivities from PDP is infeasible. However, the recombination limited PDP in this work suggests that the diffusivity of hydrogen in liquid lithium is sufficiently rapid, which supports Moriyama's results [52], as shown in Fig.4.14.

Shown in Figure 4.15 is the simulation result of the hydrogen concentration profile in liquid lithium during deuterium PDP. It is shown that the hydrogen concentration profile in the liquid lithium is uniform at steady state, which indicates it to be in the R-R regime.

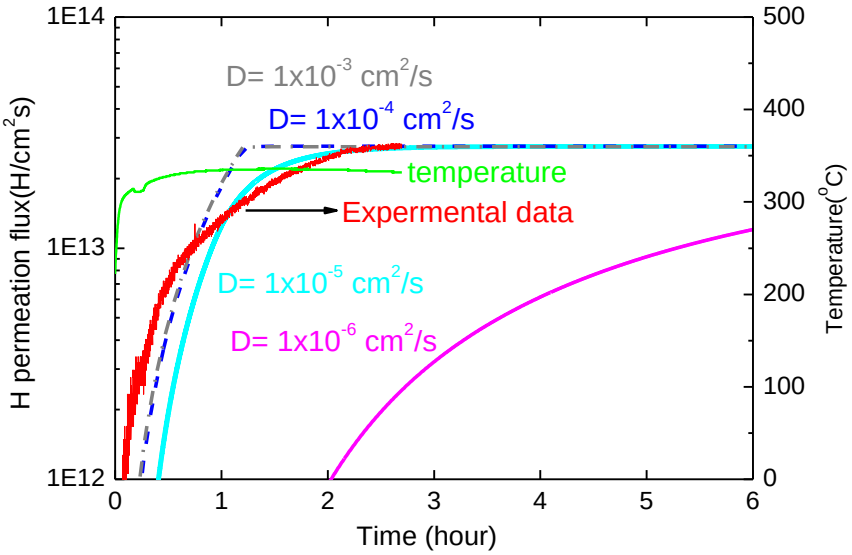

Figure 4.13 Comparison of experimental data and simulation results on hydrogen PDP permeation flux for liquid lithium.

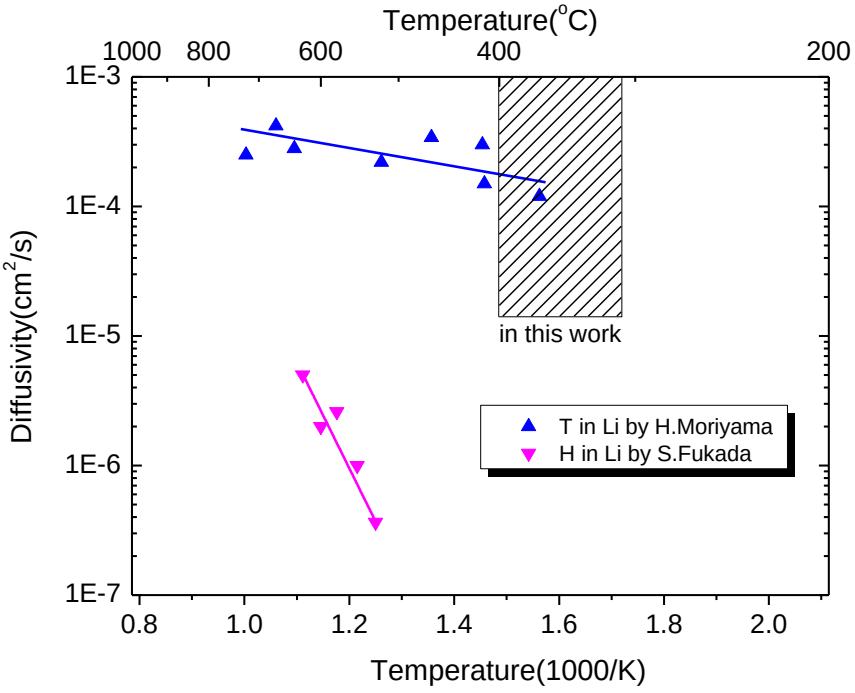

Figure 4.14 Comparison of Hydrogen diffusivities in liquid lithium [52, 57].

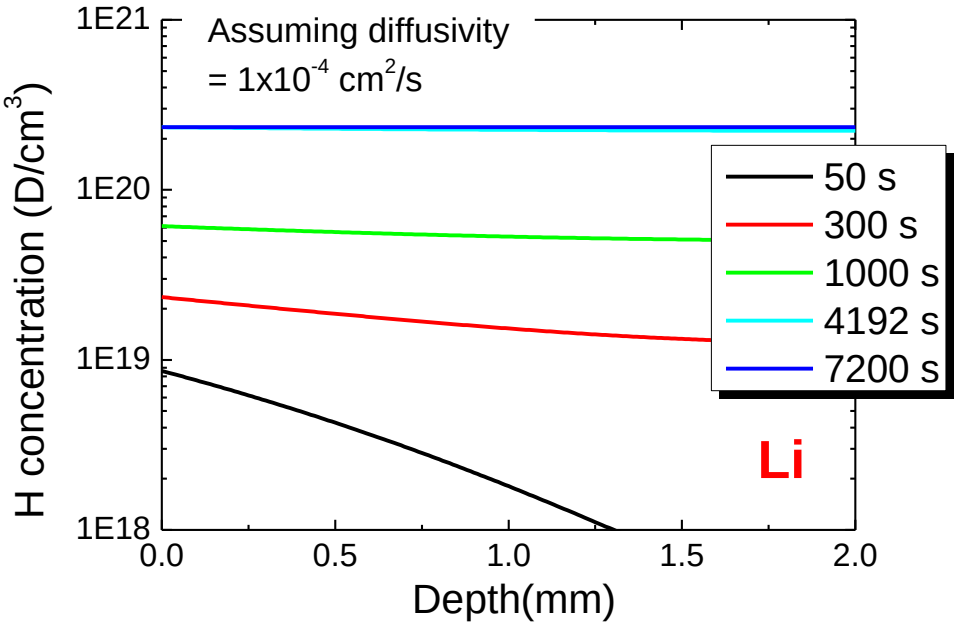

Figure 4.15 Hydrogen concentration profile in liquid lithium during deuterium PDP.

4.3. Hydrogen isotopes transport and retention in liquid GaInSn

4.3.1 Hydrogen and deuterium PDP through GaInSn

Hydrogen PDP experiments have been conducted with 2 mm thick GaInSn from 390 to 528^{o}C. Deuterium PDP experiments have been conducted with 2 mm and 4 mm thick GaInSn from 363 to 546^{o}C. Shown in Fig.4.16 are the time evolutions of hydrogen PDP fluxes through 2 mm GaInSn and the time evolutions of deuterium PDP fluxes through 4mm GaInSn at different temperatures. Plasmas were started at time t=0 s. Shown in Fig. 4.17 are the steady state hydrogen PDP fluxes through 2 mm GaInSn, and the steady state deuterium PDP fluxes through 2 mm and 4 mm GaInSn. It is obvious that PDP fluxes increase as the temperature increases. Hydrogen and deuterium PDP fluxes are close to each other for the same thickness of GaInSn. And the deuterium PDP fluxes through 2 mm GaInSn are about 2 times of the PDP fluxes through 4 mm GaInSn. The thickness effects on PDP fluxes indicate that hydrogen isotopes PDP through liquid GaInSn are diffusion-limited for the downstream surface.

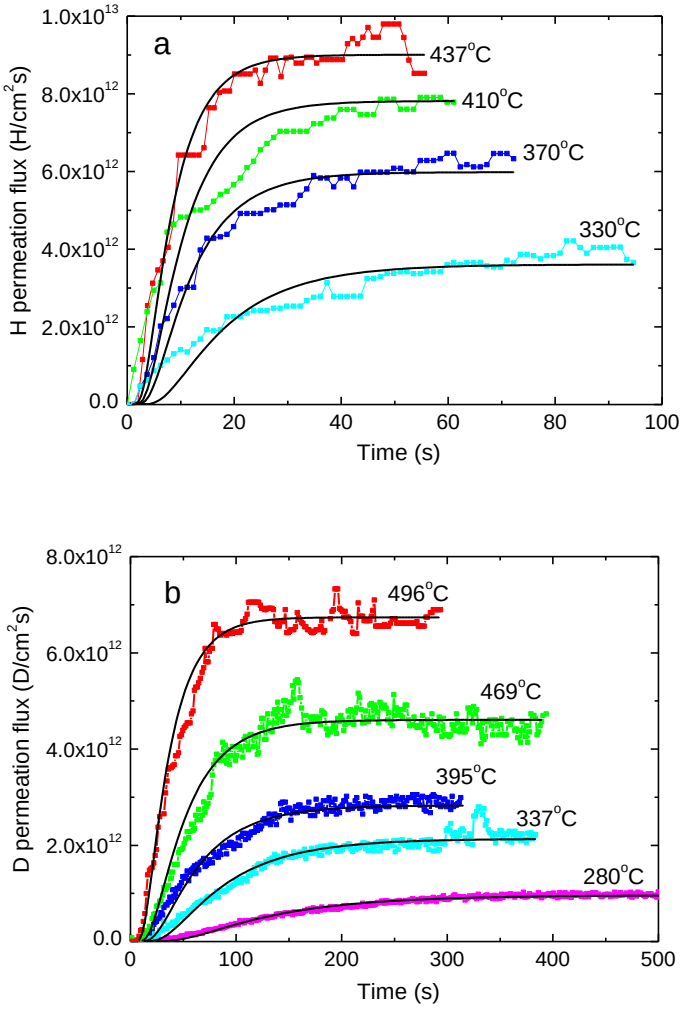

Figure 4.16 Time evolutions of hydrogen permeation fluxes through 2mm liquid GaInSn (a) and deuterium permeation fluxes through 4mm liquid GaInSn (b). Plasmas were started at time t=0 s. The black curves are fitting results from Eq.4.12.

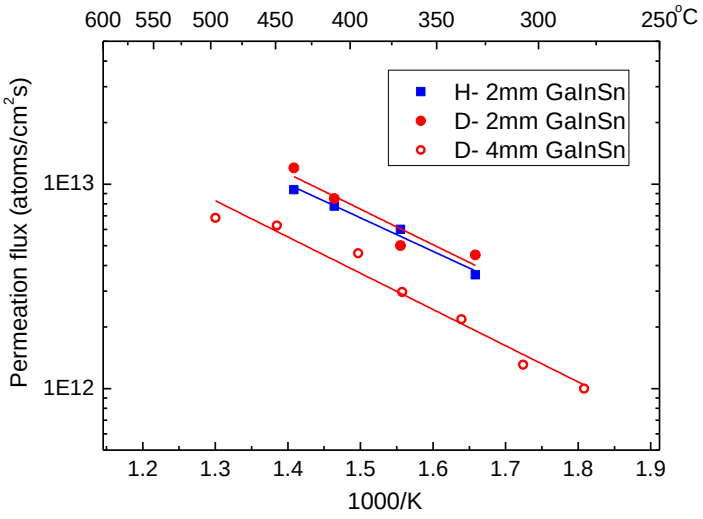

Figure 4.17 Temperatures effects on the steady state hydrogen (H) and deuterium (D) PDP fluxes through liquid GaInSn.

For PDP taking place in the R-D regime, the hydrogen concentration, $C_{0,}$ at the upstream surface is assumed to be constant, and the hydrogen concentration, $C_{1,}$ at downstream surface is assumed to be C_1=0. Then a time dependent expression for the hydrogen permeation flux $J_+(t)$ is possible to obtain where the initial concentration throughout the membrane is zero[81]:

$$J_+(t) = \frac{DC_0}{L} \times [1 + 2\sum_{n=1}^{\infty}(-1)^n \exp\left(-D\frac{n^2\pi^2}{d^2}t\right)] \qquad (4.12)$$

where diffusivity D is assumed to be constant. Then the experimental permeation breakthrough curves shown in Fig.4.16 are individually fitted by Eq.4.12. As a result, hydrogen and deuterium diffusivity have been obtained and are shown in Fig.4.18. The diffusivity of hydrogen isotopes in liquid GaInSn can be given as following:

Hydrogen: $\mathrm{D} = 3.52 \times 10^{-3}\exp(\frac{-0.192(eV)}{kT})$ cm^2/s (4.13)

Deuterium: $\mathrm{D} = 3.30 \times 10^{-3}\exp(\frac{-0.192(eV)}{kT})$ cm^2/s (4.14)

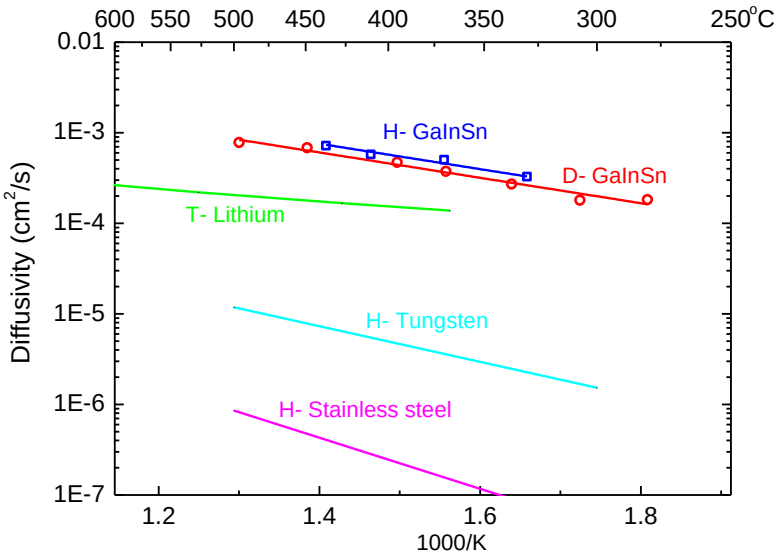

Figure 4.18 Hydrogen and deuterium diffusivity in liquid GaInSn. Tritium diffusivity in liquid lithium [17] and hydrogen diffusivity in tungsten and stainless steel [18] are shown for comparison.

4.3.2 Hydrogen and deuterium recombination coefficients

For PDP taking place in the R-D regime, the steady state permeation flux J_+ is given by:

$$J_+ = \frac{D}{L}\sqrt{\frac{J}{K_r}} \tag{4.15}$$

where J is the net hydrogen implantation flux, K_r is the hydrogen recombination coefficient at the upstream surface, D is the hydrogen diffusivity, L is the thickness of the membrane. J is measured by the Langmuir probe with an assumption that the reflection coefficient is 0.5. Then by taking the diffusivity and permeation flux data into Eq. 4.15, the upstream recombination coefficient, $K_{r,}$ has been obtained and is shown in Fig.6. The hydrogen isotopes surface recombination coefficients for liquid GaInSn can be given as following:

Hydrogen: $K_r = 7.74 \times 10^{-21} \exp(\frac{0.76(eV)}{kT})$ (4.16)

Deuterium $K_r = 7.74 \times 10^{-21} \exp(\frac{0.76(eV)}{kT})$ (4.17)

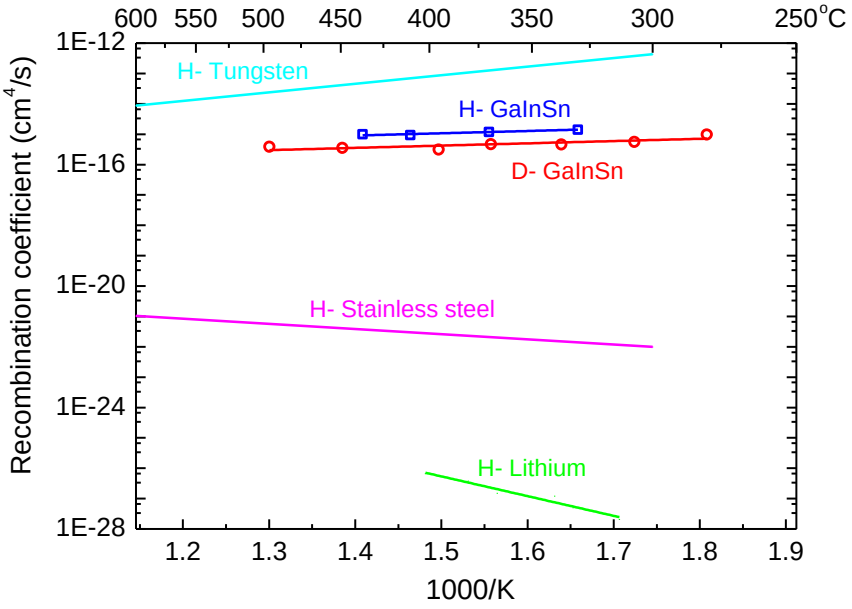

Figure 4.19 Hydrogen and deuterium surface recombination coefficients for liquid GaInSn.

4.3.3 Deuterium concentration in GaInSn during PDP

In Section 4.3.2, the hydrogen diffusivity is obtained by fitting the permeation breakthrough curves with Eq.4.12, assuming the diffusivity is constant. However, the temperature of the sample increases 10-20°C under the plasma bombardment in each PDP experiment. So the hydrogen diffusivity and surface recombination coefficient would vary. To check the temperature effects on the evaluation of the diffusivity, temperature dependent D(T(t)), K_r(T(t)) from equation Eq.4.14 and Eq.4.17 have been employed to calculate the deuterium permeation flux. T(t) is the temperature as a function of time, which is taken from the thermocouple recording. Fig.4.20 shows a comparison of calculation result with experimental data for deuterium PDP on 4mm GaInSn, where the temperature increased from 378°C to 392°C. It is found that the deviation between the calculation result and experimental data is not significant, which suggests the diffusivity

obtained by fitting method in section 4.3.2 is efficacious. Using the same D(T(t)) and $K_r(T(t))$, the time evolution of the deuterium concentration profile in GaInSn during PDP has been calculated and is shown in Fig.4.21. It is found that the deuterium concentration at quasi steady state is about 3×10^{15} D/cm^3 for the upstream surface.

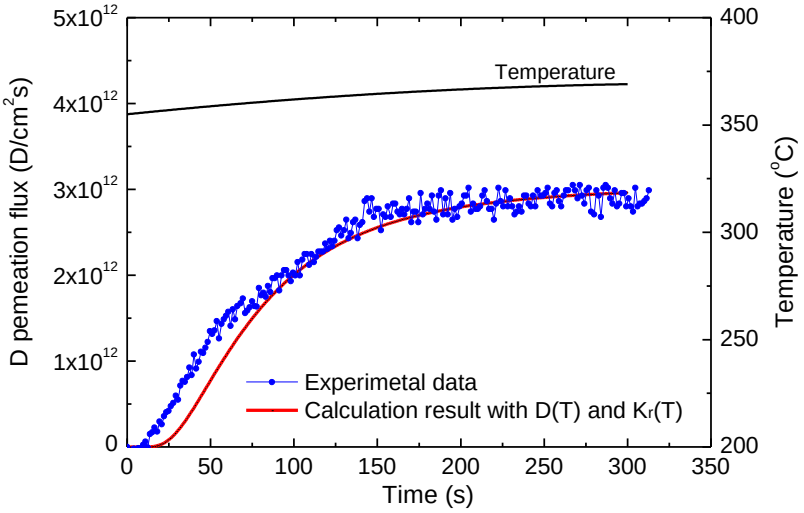

Figure 4.20 A comparison of experimental data and calculation result on deuterium permeation flux through 4mm GaInSn.

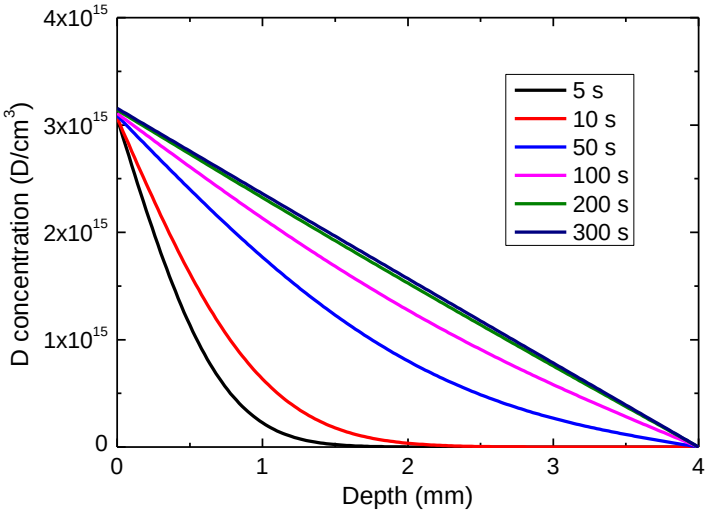

Figure 4.21 Time evolution of deuterium concentration profile in GaInSn during deuterium PDP

4.3.4 TDS measurements of hydrogen isotopes retention

After being exposed to hydrogen or deuterium plasmas during PDP, the samples are naturally cooled down to room temperature. 10 gram of liquid GaInSn sample is taken out of VEHICLE-1 and put into a stainless tray by using a syringe. Then the liquid GaInSn sample together with the tray is heated in the thermal desorption spectroscopy (TDS) facility. 10 grams of fresh GaInSn without being exposed to plasma is also measured as the background. For TDS measurement after hydrogen PDP, the hydrogen retention is found to be less than the order of 10^{16} D/cm^3, while a precise amount is not obtained due to the high background of hydrogen pressure. Fig.4.22 shows the TDS measurement data after deuterium PDP. By time integrating the desorption fluxes, the amount of deuterium static retention is found to be 2.92×10^{14} D/cm^3. Considering some of the deuterium atoms desorb from the sample during the cooling down process, it is consistent with the average dynamic deuterium concentration of 1.5×10^{15} D/cm^3, as shown in Fig.4.21.

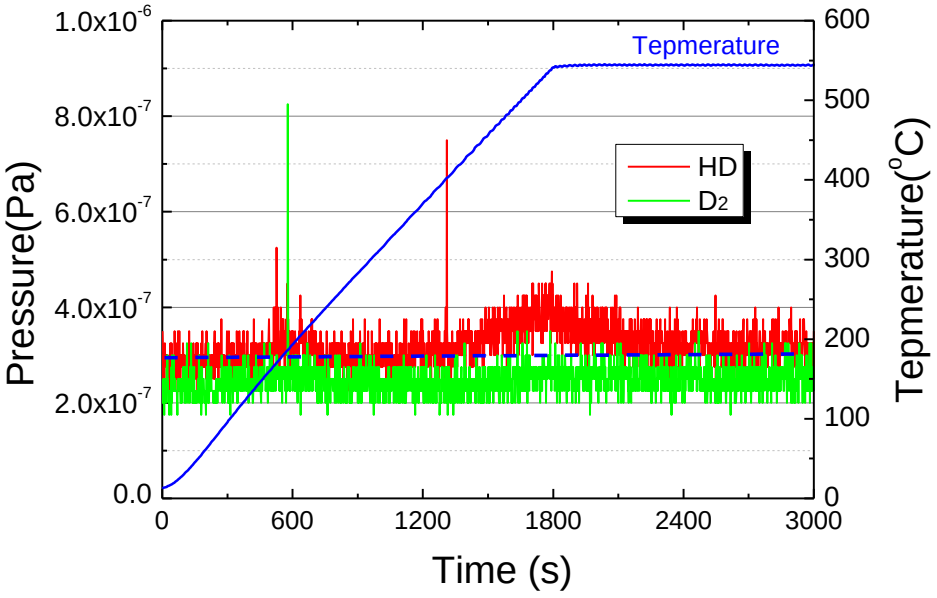

Figure 4.22 TDS measurement for GaInSn after deuterium PDP.

4.4. Hydrogen isotopes transport and retention in liquid Ga

4.4.1 Hydrogen and deuterium PDP through liquid Ga

Hydrogen PDP experiments have been conducted with 4 mm deep Ga from 300 to 475^{o}C. Deuterium PDP experiments have been conducted with 2 mm and 4 mm deep GaInSn from 270 to 510 ^{o}C. Shown in Fig.4.23 are the time evolutions of deuterium PDP fluxes through 4mm deep Ga at different temperatures. Plasmas were started at time t=0 s. Shown in Fig. 4.24 are the steady state hydrogen PDP fluxes through 2 mm deep Ga, and the steady state deuterium PDP fluxes through 2 mm and 4 mm deep Ga. It is obvious that PDP fluxes increase as the temperature increases. Hydrogen and deuterium PDP fluxes are close to each other for the same depth of Ga samples. And the deuterium PDP fluxes through 2 mm deep Ga are about 2 times of the PDP fluxes through 4 mm deep Ga. The thickness effects on PDP fluxes indicate that hydrogen isotopes PDP through liquid Ga are diffusion-limited at the downstream surface.

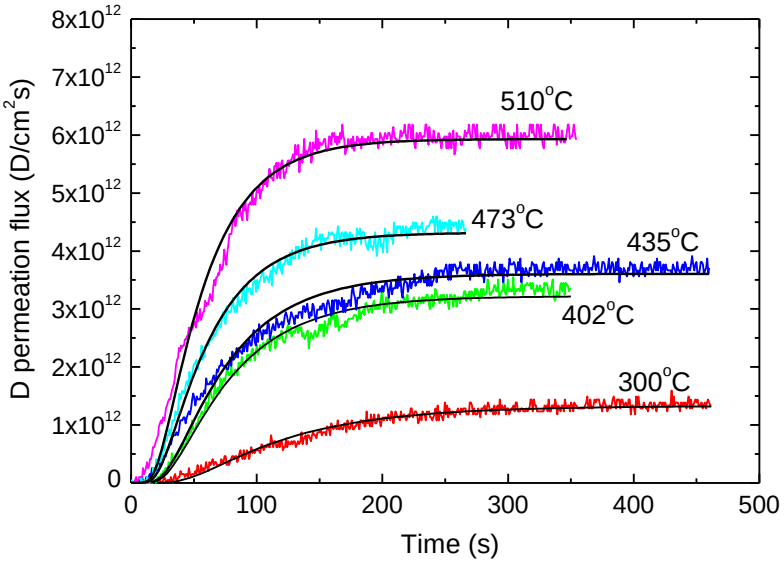

Figure 4.23 Time evolutions of deuterium permeation fluxes through 4mm liquid gallium.

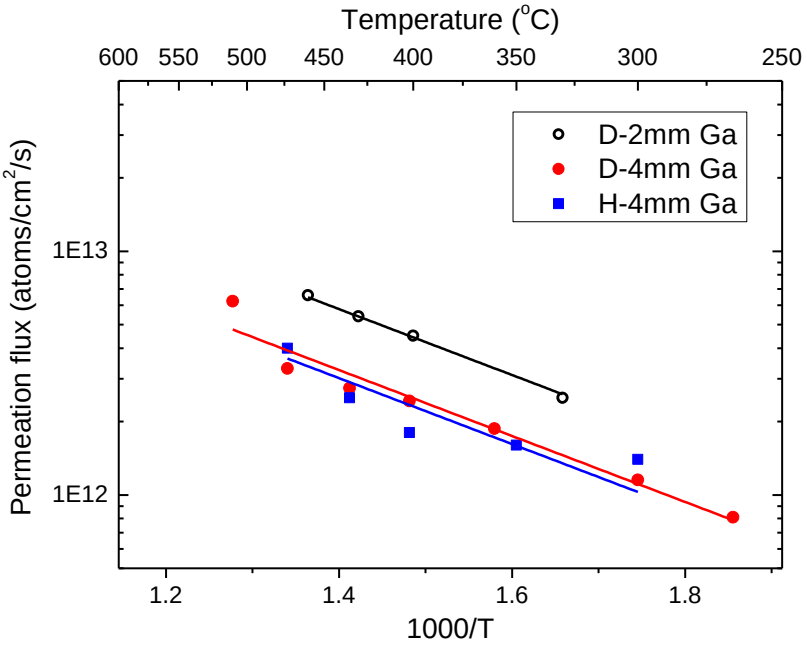

Figure 4.24 Temperatures effects on the steady state hydrogen (H) and deuterium (D) PDP fluxes through liquid gallium.

For PDP taking place in the RD regime, the hydrogen concentration C_0 at the upstream surface is assumed to be constant, and the hydrogen concentration C_1 at the downstream surface is assumed to be C_1=0. Then hydrogen isotopes diffusivity in Ga are obtained by fitting the permeation flux $J_+(t)$ by using Eq.4.12. As a result, the diffusivity of hydrogen isotopes in liquid Ga has been obtained (shown in Figure 4.25). They can be given as following:

$$\mathrm{D(H)} = 4.67 \times 10^{-3} \exp\left(\frac{-0.154(eV)}{kT}\right) \quad cm^2/s \qquad (4.16)$$

$$\mathrm{D(D)} = 3.76 \times 10^{-3} \exp\left(\frac{-0.154(eV)}{kT}\right) \quad cm^2/s \qquad (4.17)$$

Similarly to the case of GaInSn, the hydrogen isotopes surface recombination coefficient for Ga has been obtained (shown in Figure 4.26)by using equation 4.15:

$$K_r(H) = 2.43 \times 10^{-17} \exp\left(\frac{0.233(eV)}{kT}\right) \quad cm^4/s \qquad (4.18)$$

$$K_r(\mathrm{D}) = 1.35 \times 10^{-17} \exp\left(\frac{0.233(eV)}{kT}\right) \quad cm^4/s \qquad (4.19)$$

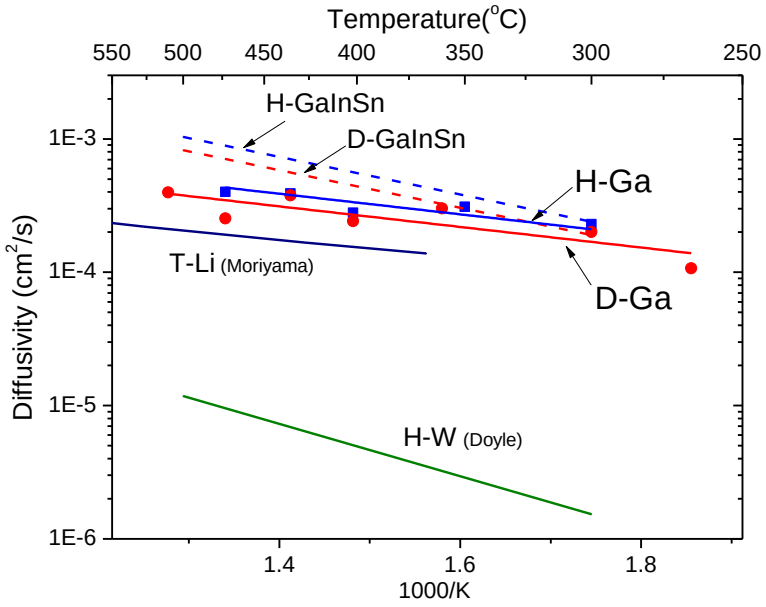

Figure 4.25 Hydrogen and deuterium diffusivity in liquid gallium.

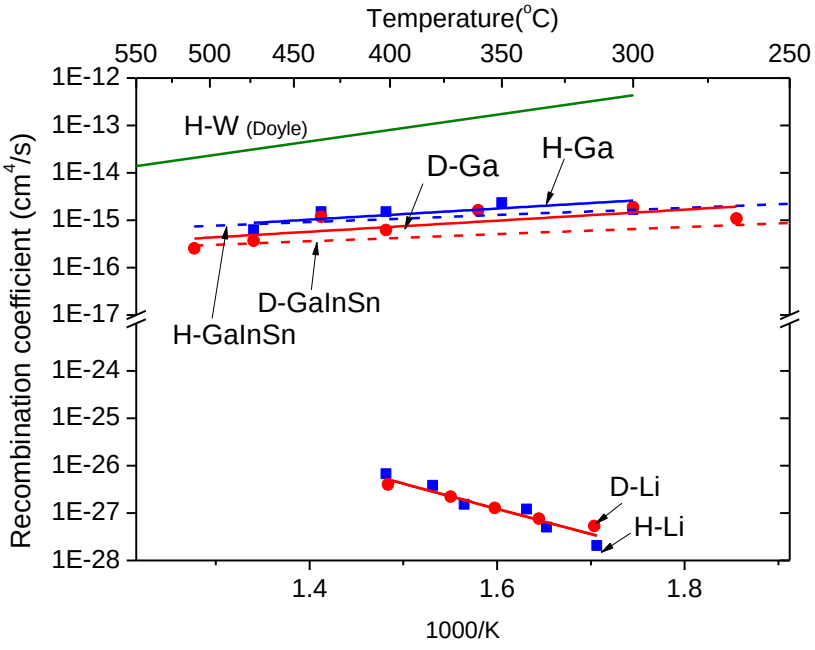

Figure 4.26 Hydrogen and deuterium surface recombination for liquid gallium.

4.4.2 Deuterium retention in liquid Ga

After being exposed to deuterium plasmas during PDP, the samples are naturally cooled down to room temperature. 10 gram of liquid Ga sample is taken out of VEHICLE-1 and put into a stainless tray by using a syringe. Then the liquid Ga sample together with the tray is heated in the thermal desorption spectroscopy (TDS) facility. Shown in Figure 4.27 is the TDS measurement for Ga after deuterium PDP at 208^{o}C. Shown in Figure 4.28 is the TDS measurement for Ga after deuterium PDP at 290^{o}C. It is found that the desorption flux of HD from the Ga sample after PDP at 208^{o}C is much higher than that from the the Ga sample after PDP at 290^{o}C. And in Figure 4.27, it is found that deuterium starts to release at ~250^{o}C. Shown in Figure 4.29 is the temperature dependence of deuterium static and dynamic retention in Ga. The static retention is obtained by integrating the desoption flux during the TDS measurements:

$$Q_S = \int_0^t \frac{P \times S}{k \times T} dt \Big/ V \tag{4.20}$$

Where P is the HD and D_2 pressure during TDS measurements; V is the volume of the Ga sample. The dynamic retention is calculated by using the following equation:

$$Q_S = \frac{1}{2} C_0 = \frac{1}{2} \sqrt{\frac{J_0}{K_r}} \tag{4.20}$$

Where C_0 is the deuterium concentration at the upstream surface during PDP; J_0 is the deuterium implantation flux; K_r is the deuterium surface recombination coefficient for Ga.

It is found that the static retention is close to the dynamic retention for PDP at temperatures below 250^{o}C; while the static retention is much less than the dynamic retention for PDP at temperatures above 250^{o}C. These results suggest that most of deuterium has released from the Ga samples during the cooling down process for PDP at temperatures above 250^{o}C. And deuterium is stably retained in Ga if the temperature is below 250^{o}C.

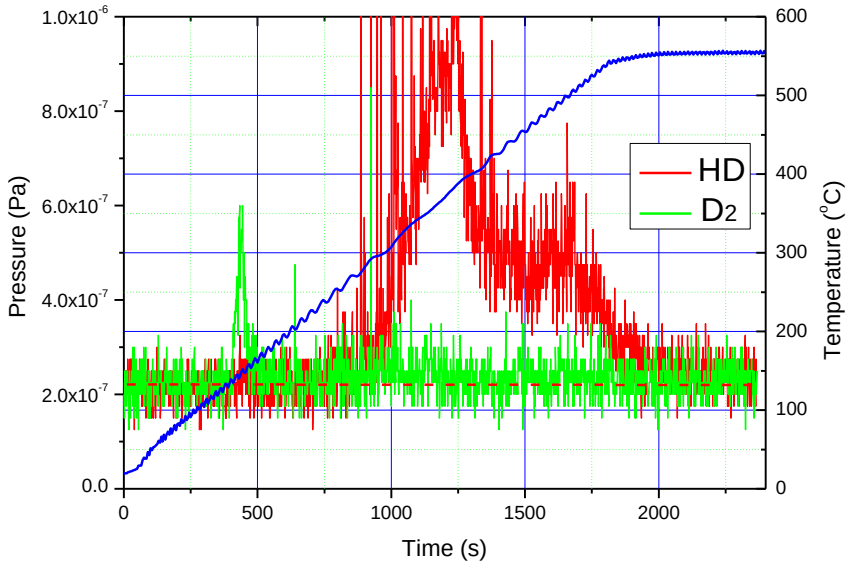

Figure 4.27 TDS measurement for gallium after deuterium PDP at 208°C.

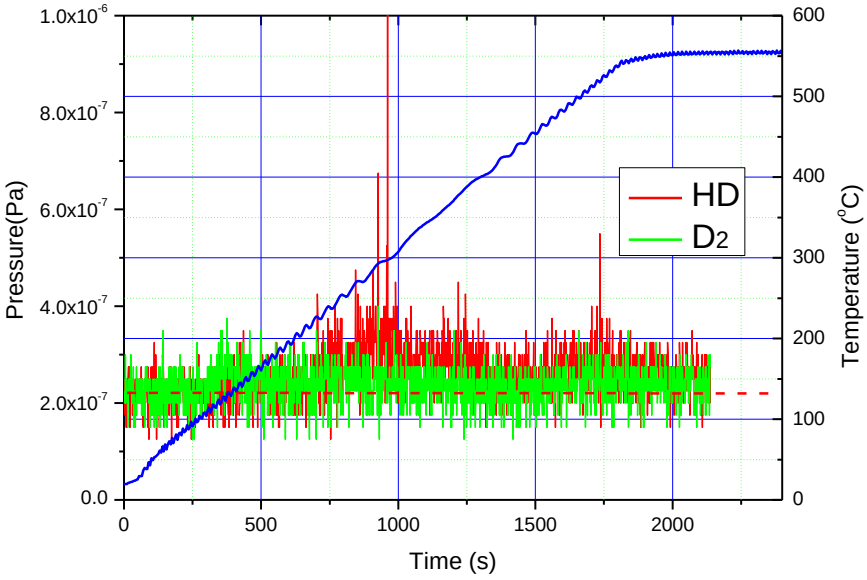

Figure 4.28 TDS measurement for gallium after deuterium PDP at 290°C.

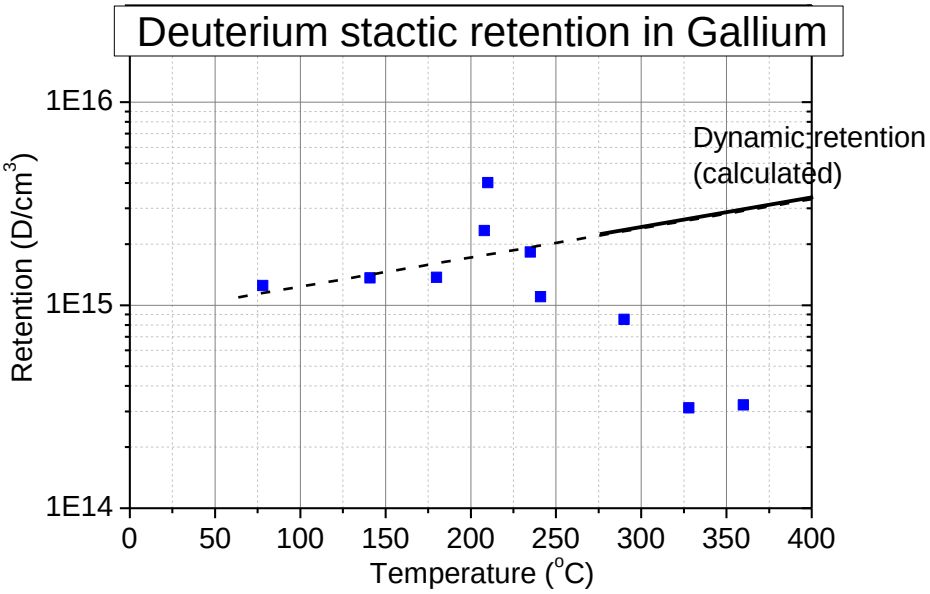

Figure 4.29 Temperature dependence of deuterium static and dynamic retention in gallium.

4.5. Hydrogen isotopes transport and retention in liquid Sn

Hydrogen and deuterium PDP experiments for Sn have been conducted under the similar conditions for liquid Ga. Temperature dependence and thickness dependence effects for Sn have been observed, which suggest hydrogen isotopes PDP through liquid Sn are in R-D regime. By using the fitting method, hydrogen and deuterium diffusivity in liquid Sn have been evaluated.

As shown in Fig.4.30, hydrogen and deuterium diffusivity for Sn are found to be of the order of 10^{-4} to 10^{-3} cm^2/s. And the deuterium diffusivity obtained in the present work are relatively in good agreement with that evaluated from molecular dynamics [109]. Shown in Fig.4.31 are hydrogen and deuterium surface recombination coefficients for liquid Sn. It is found that the data is about two orders of magnitude lower than that for liquid Ga. Generally, lower surface recombination coefficient suggests higher dynamic retention, because dynamic retention is inversely proportional to the surface recombination coefficient, as shown in Equ.4.20.

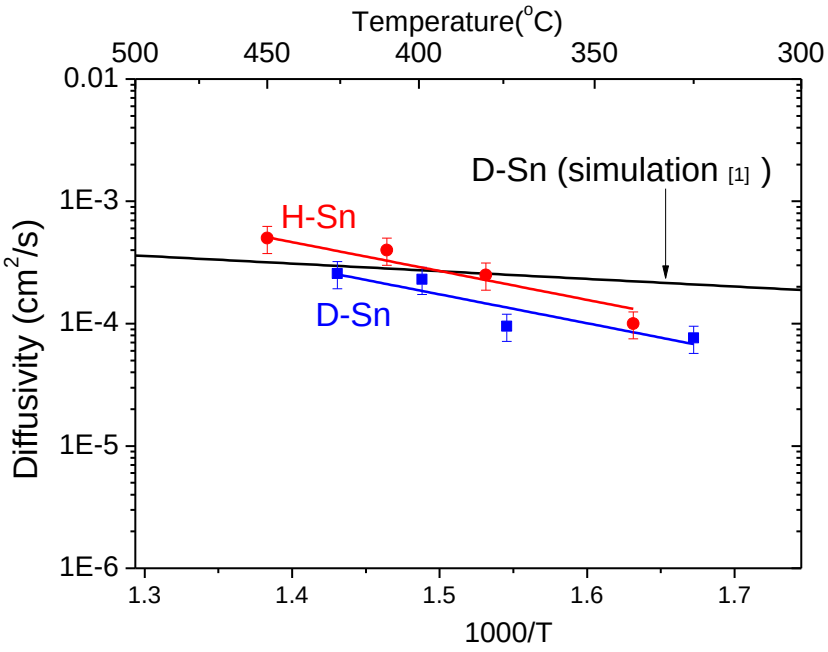

Figure 4.30 Hydrogen and deuterium diffusivity in liquid Sn. The data evaluated from molecular dynamics is shown for comparison [109].

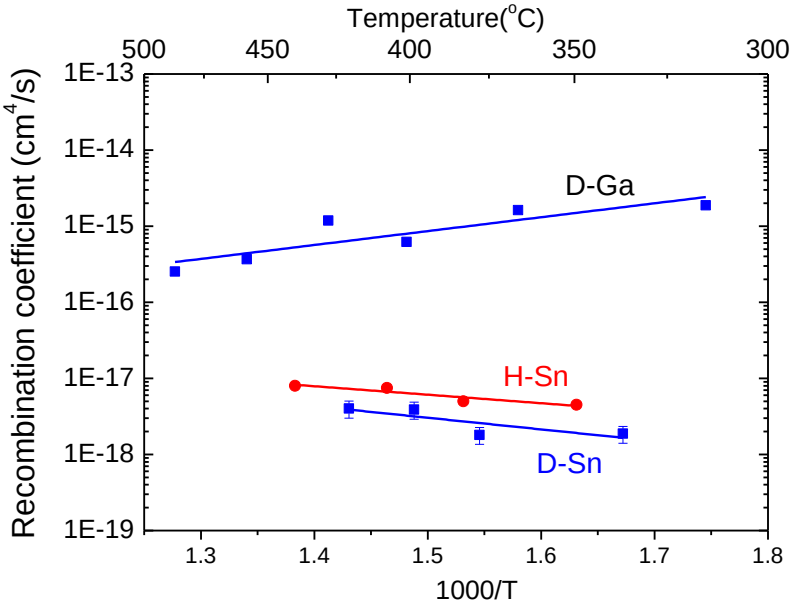

Figure 4.31 Hydrogen and deuterium surface recombination coefficient for Sn and Ga.

After deuterium plasma exposure during PDP, the deuterium static retention in the Sn samples are evaluated by TDS. As shown in Fig4.32, it is found that the deuterium static retentions in liquid Sn are of the order of 10^{16} to 10^{17} D/cm^3. They are smaller than the dynamic retentions, because some of the deuterium desorbed from the samples during the cooling process. And the static retentions in Sn are about one orders of magnitude than that of Ga, which is consistent with their difference on surface recombination coefficients.

Shown in Fig.4.33 and Fig.4.34 are overview of the hydrogen diffusivity and recombination coefficient data taken in this thesis work. It is found that hydrogen isotopes diffusivity for these liquid metals, including liquid GaInSn, Ga, Sn and Li, are all in the orders of 10^{-4} to 10^{-3} cm^2/s. In Fig.4.34, it is found that the surface recombination coefficient for these liquid metals is several orders of magnitude different. Especially, the data for liquid Li is much lower than liquid GaInSn, Ga and Sn.

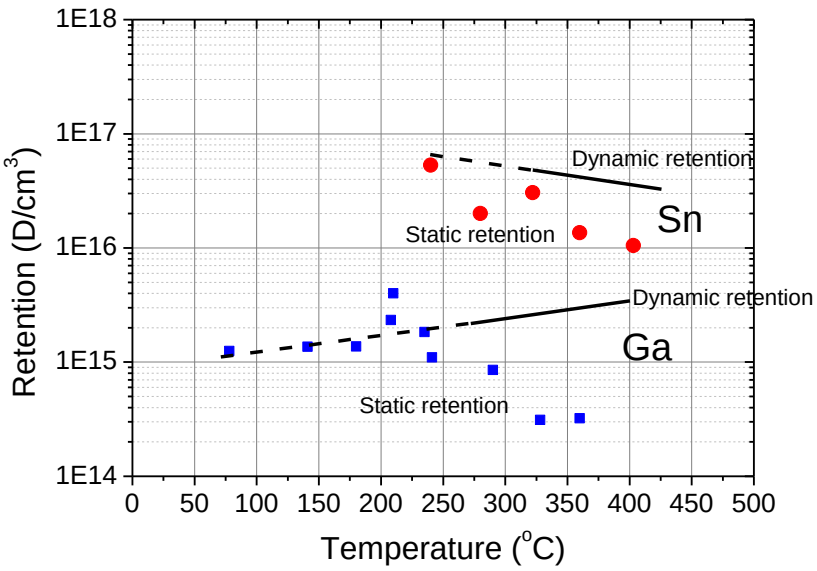

Figure 4.32 Deuterium static and dynamic retention for liquid Sn and Ga.

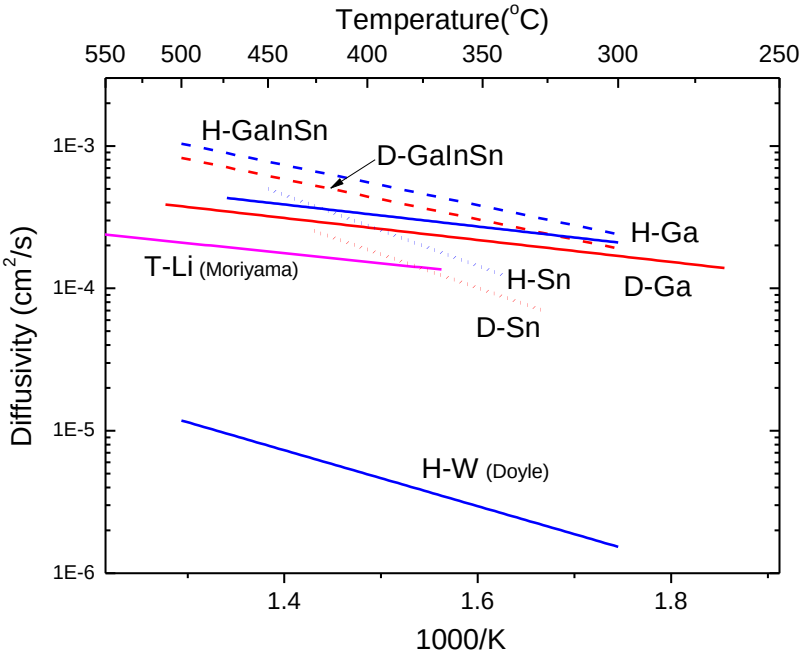

Figure 4.33 Hydrogen isotopes diffusivity for liquid metals.

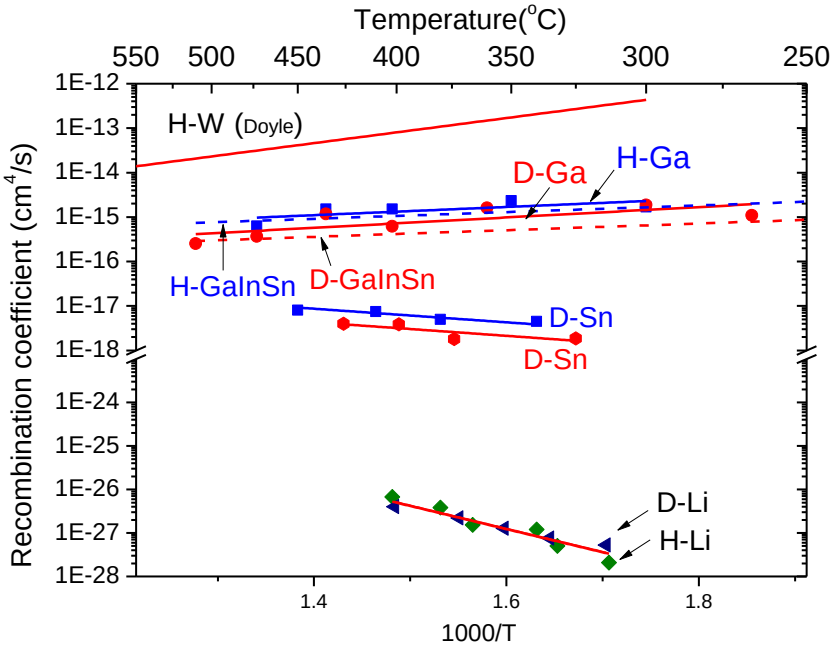

Figure 4.34 Hydrogen isotopes surface recombination coefficient for liquid metals.

4.6. Summary

Hydrogen isotopes plasma-driven permeation through liquid metals, including lithium, GaInSn and gallium have been investigated by using a steady state laboratory-scale plasma device: VEHICLE-1.

Both GDP and PDP have been found to be recombination-limited for titanium, which suggests that surface reactions can dominate the hydrogen transport other than diffusion for hydride forming metals. The hydrogen surface recombination coefficient for titanium has been measured. And it has been found that the surface recombination coefficient is increased under plasma bombardment.

Hydrogen and deuterium PDP have been found to be recombination-limited for liquid lithium. The hydrogen and deuterium transport parameter data taken for liquid lithium have been found to be in good agreement with the literature data, which validates the mesh-surface tension method.

Hydrogen and deuterium PDP have been found to be diffusion-limited for liquid GaInSn, gallium and Sn. The hydrogen transport parameters such as the diffusivity and the recombination coefficient have been measured. The temperature dependence of deuterium dynamic and static retention have been evaluated. Both of them have been found to be relatively small.

It is believed that hydrogen isotopes transport parameter data for other liquid metals can also be evaluated, by using this mesh-surface tension method in PDP experiments. With these transport parameter data, it is possible to predict hydrogen isotopes recycling and retention for liquid PFCs.

Chapter 5 Natural convection effects on deuterium PDP

5.1. Introduction

Natural convection corresponds to situations where the fluid is set in motion by buoyancy force due to density variations. Consider a layer of fluid heated from below. As a result the density at the bottom layer becomes lighter than at the top. The system is thus top heavy but does not necessarily undergoes convective motion since viscosity and thermal diffusivity of the fluid try to prevent the convective motion. If the fluid is heated sufficiently (higher temperature gradient across the layer), then only the top-heavy state becomes unstable and convective motion ensues. Here we shall consider the conditions necessary for the onset of the thermal instability. The first intensive experiments were carried out by Benard in 1900. He experimented on a fluid of thin layer and observed appearance of hexagonal cells when the instability in the form of convection developed [110]. Rayleigh in 1916 developed the theory which found the condition for the instability with two free surfaces. He showed that the instability would result if the temperature gradient was large enough so that the so called Rayleigh number exceeds a certain (critical value) [111].

It is reasonable to foresee this phenomenon in a fusion device, where the liquid PFCs and liquid blankets would run at high temperature ranges. $Ga_{67}In_{20.5}Sn_{12.5}$ is a benign alloy with the melting point of 10.5^{o}C, so it is chosen as a surrogate material in the present work. A plasma-driven permeation (PDP) setup employing GaInSn is installed in a linear plasma device VEHICLE-1. The natural convection effects on deuterium permeation through liquid GaInSn are experimentally investigated. In addition, analytical result on natural convection and simulation result on the motion of the liquid and the deuterium transport process are presented.

5.2. Experimental setup

The deuterium PDP experiments are conducted in VEHICLE-1. In this work the electron temperature is ~10eV and the plasma density is ~10^{10}cm^{-3}. The ion bombardment flux is ~10^{16}D/cm^{2}s, and the bombarding energy is set at 29eV by applying a negative DC bias on the sample tray. A liquid metal sample is fixed in such a way that the upstream surface is exposed to deuterium plasma, while the downstream side is exposed to an

ultrahigh vacuum (10^{-6}~10^{-5} Pa) chamber. The upstream chamber and downstream chamber are separated by the liquid metal. As shown in Fig.5.1, the bottom of the tray is a mesh sheet made of stainless steel, which is referred to as liquid supporting mesh (LSM). The diameter of each opening of the mesh is ø0.4mm. The area of the sheet is 6.6 cm^2, and the total area of the openings is 0.66 cm^2. A resistive heater is set under the mesh sheet to control the temperature. The temperature is measured by a thermocouple attached to the sidewall of the liquid metal. Deuterium permeation flux due to PDP is measured by a quadrupole mass spectrometer (QMS) at the downstream side.

Two sets of experiments are prepared for comparison. In Case **A**, the depth of the liquid is 15mm, and the diameter of the tray is ø29mm, as shown in Fig.5.1(a). It is expected that natural convection would take place in the liquid metal. And the detailed discussion is shown in Section 3. In Case **B,** a Convection Preventing Mesh (CPM) sheet is immersed in the middle of the liquid metal, as shown in Fig.5.1(b). The thickness of the mesh sheet is 0.5mm. The diameter of each opening is ø1mm, and the opening area is 40.3% in total, as shown in Fig.5.2.

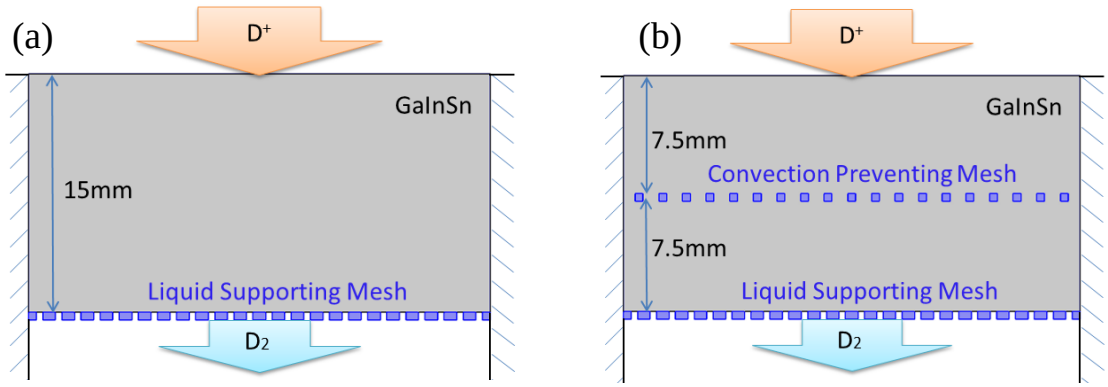

Figure 5.1 (**a)**. A liquid metal GaInSn sample in the tray. (**b)**. A liquid metal sample with a Convection Preventing Mesh (CPM) sheet immersed in the middle.

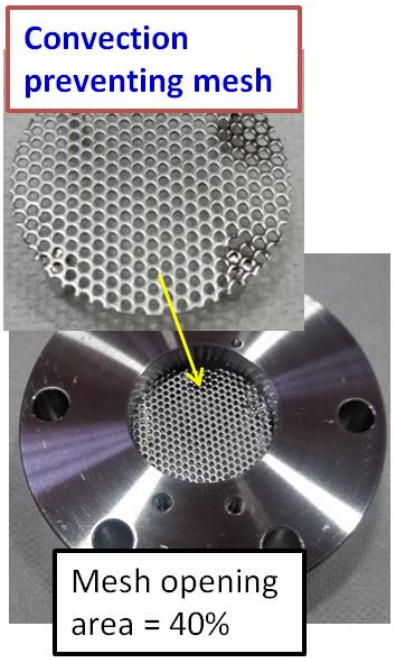

Figure 5.2 A picture of the plasma-driven permeation setup with a convection preventing mesh.

5.3. Results and discussion

5.3.1 Criteria for natural convection

During the PDP experiments, the heat load on the top surface due to the plasma bombardment is ~1 kW/m^2, while the heating power by the resistive heater at the bottom is estimate to be ~10 kW/m^2. As the heating power is higher at the bottom, one may assume that natural convection, like Rayleigh–Benard convection would take place in the liquid during the PDP experiments. Since there is a density gradient between the top and the bottom plates, gravity acts trying to pull the cooler, denser liquid from the top to the bottom. This gravitational force is opposed by the viscous damping force in the fluid. The balance of these two forces is expressed by a non-dimensional parameter called the Rayleigh number. The Rayleigh number is defined as:

$$R_a = \frac{\alpha(T_{down} - T_{up}) g d^3}{k v} \tag{5.1}$$

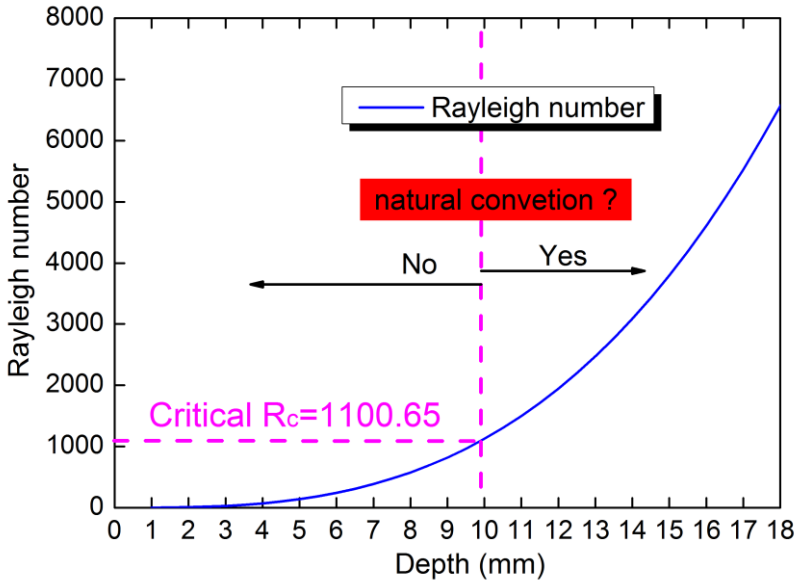

Figure 5.3 Rayleigh number of the liquid metal with different depth for T_{down}-T_{up}= 5.8K.

where $\alpha = 1 \times 10^{-4}$ is the thermal expansion coefficient taken from gallium, T_{down} is the temperature at the bottom, T_{up} is the temperature at the top, g is the acceleration due to gravity, d is the depth of the liquid, k is the thermal diffusivity, v is the kinematic viscosity. The critical Rayleigh number R_C in the case of a rigid boundary at the bottom and a free boundary at the top is R_C = 1100.65 [110]. For liquid GaInSn with d =15 mm, T_{up}=723 K, thermal conductivity λ=40 W/m/K [112], assuming the heat loss q at the top is due to the thermal radiation to the ambient surroundings, then the temperature difference is calculated as:

$$T_{down} - T_{up} = \frac{q \times d}{\lambda} < \frac{\sigma \times T_{up}^4 \times d}{\lambda} = 5.8 \text{ K} \quad (5.2)$$

where σ is the Stefan–Boltzmann constant. For $T_{down} - T_{up} = 5.8$ K, the depth dependence of the Rayleigh number of GaInSn has been calculated, as shown in Fig.5.3. For liquid GaInSn with d =15 mm, the Rayleigh number $R_a \approx 3797.9$, which is larger than the critical Rayleigh number R_C. Therefore it is expected that natural convection would take place in the liquid GaInSn in Case **A**.

For liquid GaInSn with a Convection Preventing Mesh (CPM) sheet immersed right in the middle, the liquid metal is considered to be "separated" into two volumes. Thus the depth of the liquid metal in each space d =7.5 mm, and the temperature difference is assumed to be 2.9K. In this case, the Rayleigh number $R_a \approx 237.4$, which is smaller than the critical Rayleigh number R_C. Therefore it is expected that natural convection would not take place in the liquid GaInSn in Case **B**.

5.3.2 Simulation results on the natural convection

The natural convection motion of the liquid metal is simulated by solving the Navier-Stokes equations with the CFD (Computational Fluid Dynamic) module in a finite element analysis software COMSOL. And the CFD module is coupled with the heat transfer module, in which the temperature distribution is solved. In this work, a simplified 2-D model is built based on the experimental conditions. In Case **A**, the depth of the liquid is 15mm, and the width is 29mm. The temperature of the top surface is set to be 723K, while the temperature of the bottom surface is 728.8K. The side walls are thermally insulated. A Boussinesq approximation is applied for the simulation, in which the variation in density is neglected everywhere except in the buoyancy term **F** [113]. The temperature dependence density of the liquid :

$$\rho_T = \rho[1 - \alpha(T - T_{up})] \tag{5.3}$$

where $\rho =$ is the density at T_{up}= 723K, $\alpha =$ is the thermal expansion coefficient, ρ_T is the density at temperature of T(K). Then the buoyancy term **F=** [F_x, F_y**]** is:

$$F_x = 0, \quad F_y = -g(\rho - \rho_T) = \rho g \alpha (T - T_{up}) \tag{5.4}$$

The top surface is set as a sliding wall, while the rest are set as no sliding wall. As a result shown in Fig. 5.4, the velocity field vector **u** = [u_x, u_y] at steady state is obtained, where the maximum velocity of the liquid is 1.6×10^{-2} m/s. It is shown that two convection cells are formed in the liquid, where the liquid rises in the center and falls down along the periphery. And the temperature distribution is shown in Fig. 5.5(a).

In Case **B**, a stainless steel mesh is set in the middle of the liquid, and the walls of the mesh are all no sliding walls. As a result, no convection motion is found in the liquid,

and the temperature distribution is found to be horizontally uniform, as shown in Fig.5.5(b). The simulation result is consistent with the analysis result in Section 5.3.1, i.e. the natural convection of the liquid metal is suppressed by the CPM.

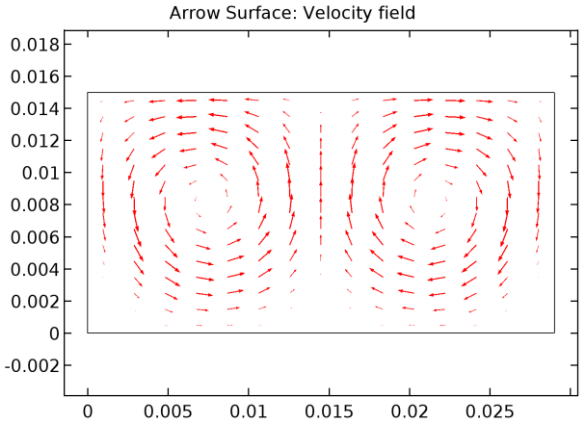

Figure 5.4 The velocity field of the liquid at steady state.

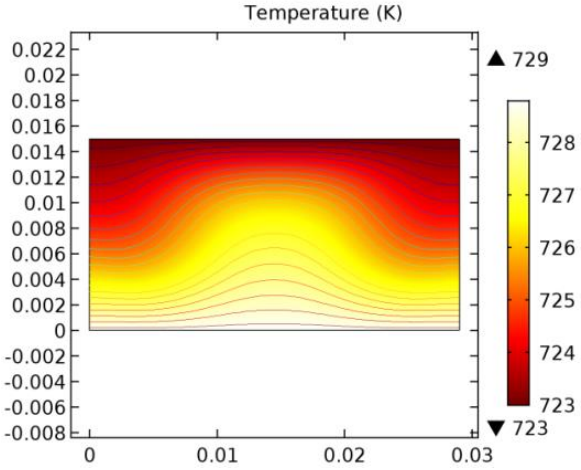

Figure 5.5 (a). Temperature profile in the liquid metal for Case **A**.

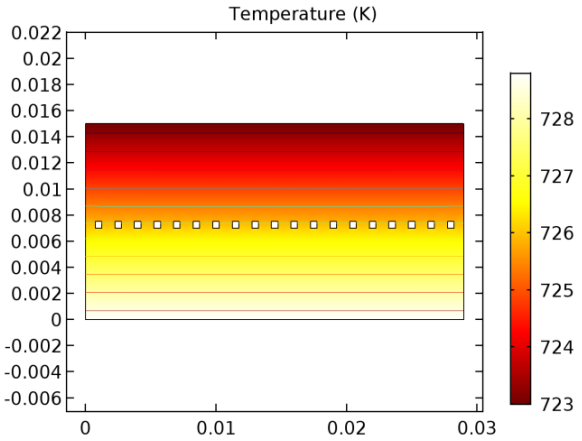

Figure 5.5 (b). Temperature profile in the liquid metal for Case **B**.

5.3.3. Simulation results on deuterium transport in the liquid metal

The deuterium transport behavior in the liquid metal is simulated with the finite element analysis method by solving a basic mass balance equation, which contains the diffusion term and convection term [114]. The diffusivity of deuterium in liquid GaInSn is estimated to be 6.8×10^{-4} cm^2/s at 450°C [115]. As the temperature difference in the liquid is small here, a constant diffusivity D = 6.8×10^{-4} cm^2/s is used for the simulation. And the velocity vector **u** = [u_x, u_y] are taken from the CFD module in Section 5.3.2.

Compared to the implantation flux J_0 = 4.8×10^{15} $atoms/cm^2/s$, the permeation flux is much smaller as shown in Fig.5.8, so the reemission flux, J_-, is approximately equal to the implantation flux, J_0. For a surface recombination coefficient K_r = 3.5×10^{-16} cm^4/s at 450°C [115],

$$J_0 \approx J_- = K_r \times C_0^2 \tag{5.5}$$

$$\Longrightarrow \quad C_0 = 3.7 \times 10^{15} \text{ atoms}/cm^3$$

Then the boundary condition for the deuterium concentration at the upstream surface is set as a constant C_0 = 3.7×10^{15} $atoms/cm^3$, assuming that it is a recombination limited process at the top surface. The deuterium concentration at the downstream surface is set as a constant C_0 = 0 $atom/cm^3$, assuming that it is a diffusion limited process at the

downstream surface. The initial concentration of the deuterium in the liquid is set as C = 0 atom/cm^3.

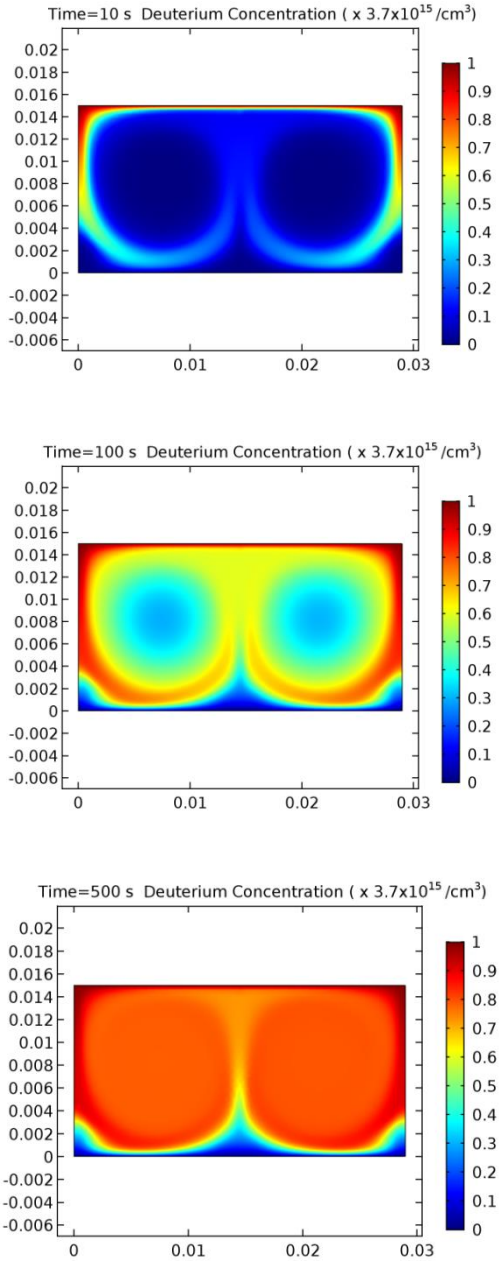

Figure 5.6 Deuterium concentration in the liquid metal at time t=10s, 100, 500s respectively for Case **A**.

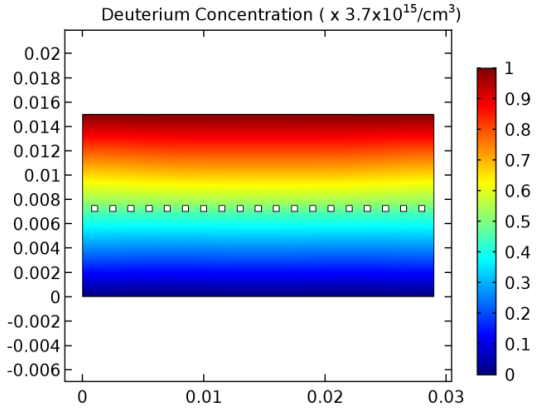

Figure 5.7 Deuterium concentration in the liquid metal at steady state for Case **B**.

Shown in Fig.5.6 are the results of the deuterium concentration profile in the liquid at time t=10s, 100s, 500s respectively for Case **A**. It is found that some deuterium is transported to the bottom within tens of seconds. For a comparison, the concentration profile for Case **B** is also obtained and shown in Fig.5.7. It is found that the deuterium concentration is horizontally uniform. And the deuterium concentration in the liquid under natural convection is much higher than that in the case without convection.

5.3.4 Plasma-driven permeation experiment

To avoid the liquid metal dropping down through the liquid supporting mesh (LSM), upward force provided by the surface tension should be larger than the gravity of the liquid metal plus the pressure difference between the two chambers. The figure of the stress balance on the liquid metal is shown in Fig.3.18. For a 15mm thick liquid GaInSn, the maximum pressure difference to avoid liquid dropping down could be ~ 4866 Pa at 500^{o}C, while the typical deuterium gas pressure in the upstream chamber for plasma is only ~ 0.1 Pa. Thus surface tension is sufficient to hold the 15mm depth liquid metal.

For deuterium plasma-driven permeation experiments, the liquid metal target has been bombarded by steady state deuterium plasma with the bias voltage set at -29 V. The initial temperature of the liquid metal is ~430^{o}C. Ar plasma bombardment with -100V bias is employed before the experiment to remove the impurity film on the liquid surface. And the temperature of the liquid during deuterium plasma bombardment is

~450^{o}C. As shown in Fig.5.8, deuterium plasma bombardment on the upstream surface starts at t=0 s. The deuterium permeation flux is calculated from the partial pressures of HD and D_2 in the downstream chamber. In Case **A**, the permeation flux rapidly increases to a quasi-steady state level as the plasma bombardment starts. And the permeation flux decreases as the plasma bombardment stops. In Case **B**, the permeation flux gradually increases to a steady state level, which is about one order of magnitude lower than that of Case **A**.

The deuterium permeation behavior under natural convection have been repeatedly observed in the temperature ~400^{o}C, as shown in Fig.5.9. The deuterium permeation fluxes rapidly increase as the plasma bombardment starts. And the permeation fluxes rapidly decrease as the plasma bombardment stops.

From the simulation results, a better understanding of the experimental observation is possible. With the CPM in the liquid, the permeation is essentially just a diffusion process, while without CPM, the permeation flux is enhanced by the natural convection in the liquid metal. However, there are still some questions remaining unsolved. First, the deuterium permeation flux without CPM is unstable, as shown in Fig.5.8, which suggests the motion of the liquid may not be a steady flow. Second, the experimental data shows that the permeation flux is enhanced by one order of magnitude, while the simulation result shows the permeation flux is enhanced by three orders of magnitude. This large disparity may be due to the difficulty to simulate the precise motion of the liquid.

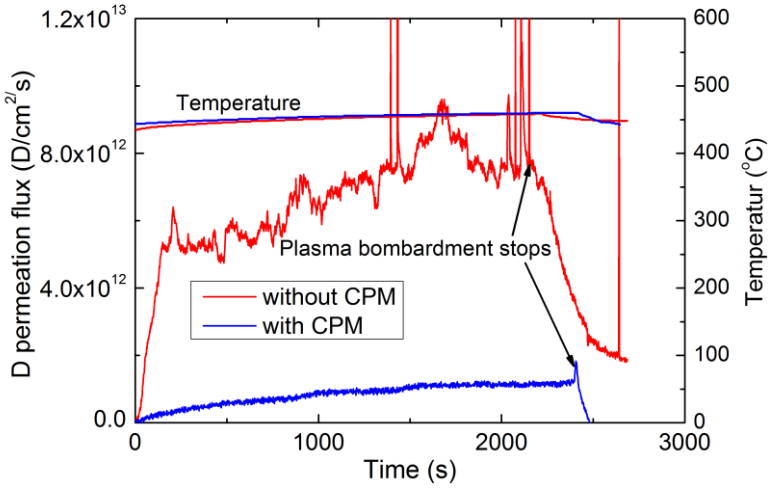

Figure 5.8 Deuterium plasma-driven permeation fluxes through 15mm GaInSn with and without CPM at ~450°C.

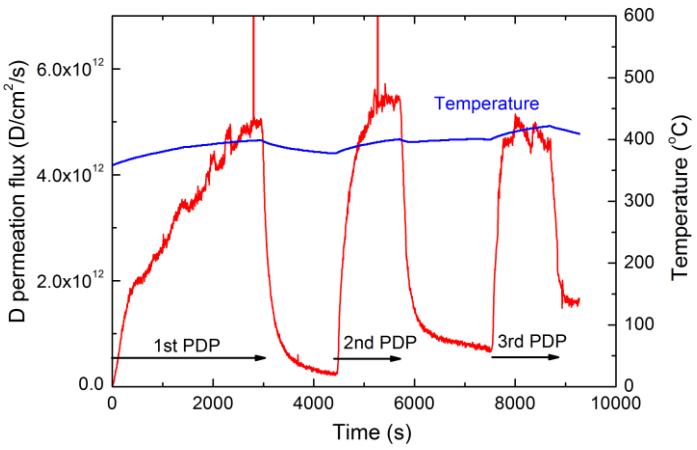

Figrue 5.9 Three sets of deuterium plasma-driven permeation fluxes through 15mm GaInSn without CPM.

5.4. Summary

Two cases of experiments on deuterium plasma-driven permeation through a liquid metal GaInSn have been conducted. One of the liquid samples is under natural convection, and the other one is standing. It has been found that deuterium permeation through the liquid is enhanced by the natural convection. And this behavior has been demonstrated by both analytical and simulation results.

In the present experiments, a temperature difference of only 5.8 K would cause natural convection, which in turn affects the deuterium transport and heat transport in the liquid metal. This suggests that natural convention should be seriously considered for liquid metals when they are applied as plasma facing components. The convection preventing mesh has shown significant effects on preventing the natural convection, which can be utilized to suppress the natural convection in a corresponding case.

Chapter 6 J×B-forced convection effects on particle recycling

6.1. Introduction

In Chapter 5, it is shown that particle transport in a liquid can be enhanced by natural convection. However natural convection will not easily take place in a divertor situation, where the liquid is warmer at the top due to extensive heat load. In order to get actively controlled liquid convection, the use of the J×B force has been proposed to be applied in a liquid divertor, which is referred to as the ACLMD (for the Actively Convected Liquid Metal Divertor) concept [116]. The basic proposal is to replace the divertor plates with a liquid metal like Ga, Sn with a low melting point and low chemical activity (Fig.6.1). The electrodes, placed in the middle of the liquid metal, can be biased positively or negatively with respect to the module. The J ×B force due to the current between the electrodes and the container wall actively drives a poloidal motion of the liquid metal in such a way that the temperature rise at the separatrix strike point is kept at an acceptable level.

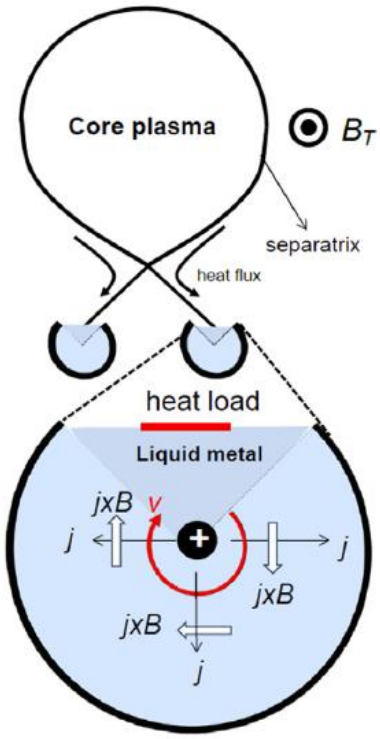

Figure 6.1 Basic scheme of ACLMD (Actively Convected Liquid Metal Divertor) [116].

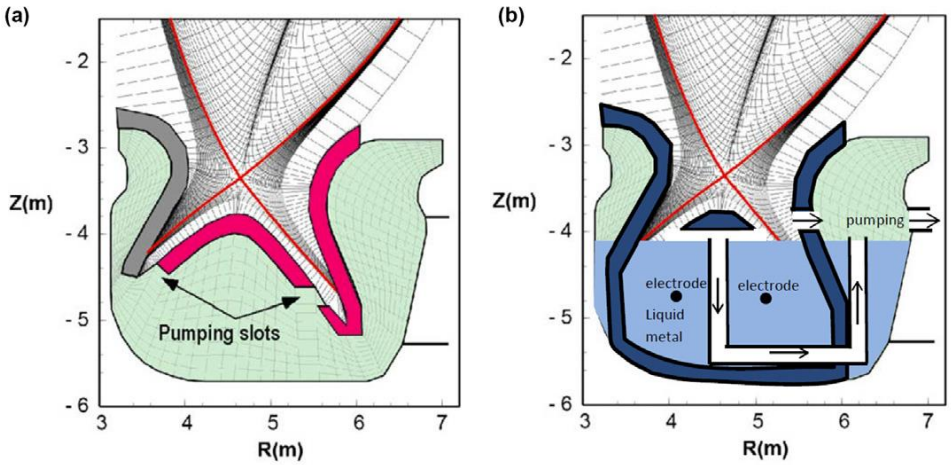

Figure 6.2 (*a*) cross-section of original SlimCS[117]. (*b*) Cross-section of SlimCS with ACLMD[116].

The scheme depicted in figure 6.1 may be adequate for an experiment in a non-nuclear device, but is not feasible for a reactor due to the difficulty for maintenance (linked structure). Figure 6.2(*a*) shows the cross-section of the original SlimCS [117] and Figure 6.2(*b*) shows a schematic view of ACLMD without a toroidally linked structure, which facilitates the maintenance. The lower part of the vacuum vessel is filled with Sn or Ga or other liquid metals with low chemical activities. The toroidally separated divertor modules, equipped with electrodes, pumping channels and cooling pipes (not shown; attached to the inner wall of the divertor module), are immersed in the liquid metal. In addition, an insulating plate immersed in the liquid metal is probably required between the divertor modules to prevent a short circuit along the field line. These insulating plates are also useful to reduce the toroidal current induced in the liquid metal at the discharge start-up. The poloidal motion of the liquid metal warrants the poloidal uniformity of temperature.

Since the liquid metal moves freely along the magnetic field line between the insulating plates, the temperature of the liquid metal is expected to be toroidally uniform. If the temperature of the liquid metal can be made uniform, the inner surface ($\sim$150m^2) of the divertor module can be fully available for cooling. The heat load onto the divertor module is 200 MW/150m^2 $\sim$ 1.3MW/m^2, which is about the same as the first wall heat load of SlimCS [117]. The heat handling technology of this level of heat load is already established.

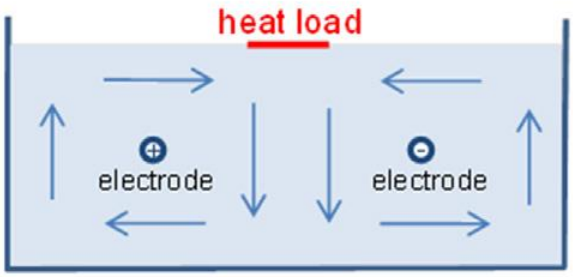

Figure 6.3 In vertical movement case, the heated liquid metal sinks vertically into the body of liquid metal. The magnetic field is normal to the paper directed towards the reader[116].

Both vertical movement and horizontal movement have been discussed By M. Shimada [116]. And it is pointed out that downward movement near the strike point is preferred to horizontal movement. Figure 6.3 shows a schematic of the vertical movement case, in which the heated liquid metal sinks vertically into the body of liquid metal. The magnetic field is normal to the paper directed towards the reader. The fluid velocityv_θ near the surface required to limit the temperature rise to an acceptable level is estimated for the case of tin (Sn) as follows:

$$v_\theta = \frac{P_{\text{div}}}{\rho C \Delta T A} \sim 0.3\,\text{m s}^{-1} \tag{6.1}$$

where P_{div} (divertor heat load) = 200MW, ρ (mass density) =7 × 10^3 kgm^{-3}, C (heat capacity) = 228 J kg^{-1} K^{-1}, ΔT (temperature rise on contact of the plasma) = 200◦C (e.g.300 → 500 ◦C: compatible with F82H), A (plasma-wetted surface area) = 2 m^2.

To fulfill this ACLMD concept, three issues have been put forward:

(1) Experimental demonstration of the rotating mechanism, especially with the opening above the liquid metal.

(2) Measurement of particle trapping efficiency at relevant temperature.

(3) Investigation of divertor characteristics with ACLMD.

In this chapter, a series of proof-of-principle experiments are conducted for the ACLMD concept, using a linearly magnetized steady state ECR plasma facility: VEHICLE-1. The deuterium recycling behavior over a liquid metal $Ga_{67}In_{20.5}Sn_{12.5}$ under JxB convection by different currents are experimentally investigated. In addition,

the motion of the liquid and the deuterium transport process in the liquid are simulated by finite element analysis.

6.2. Experimental setup

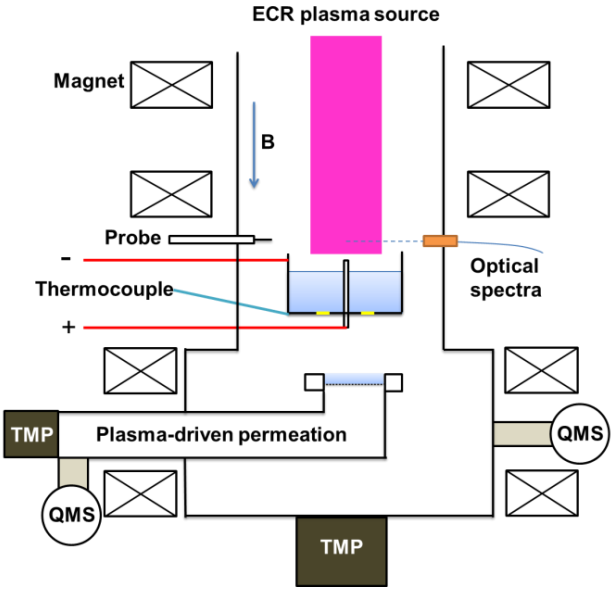

Figure 6.4 A schematic diagram of the mini-ACLMD setup in VEHICLE-1.

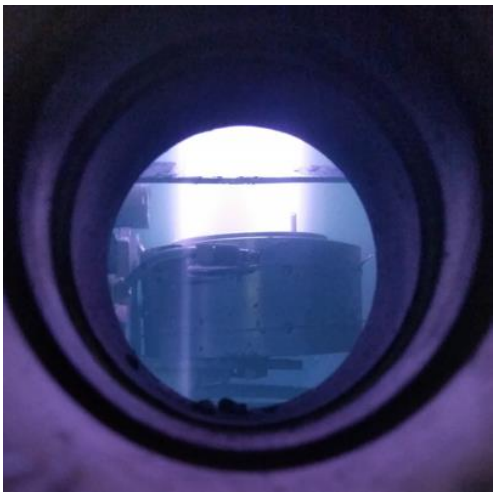

Figure 6.5 A photo of the liquid metal exposed to the deuterium plasma.

Shown in Fig.6.4 is the schematic diagram of the mini-ACLMD setup in the linear plasma device, VEHICLE-1. The plasma is generated by a 2.45GHz ECR source with the resonant magnetic field of 875 Gauss. Liquid metal GaInSn is put in a stainless steel cup with an inner diameter of 50mm and a depth of 25mm. The depth of the liquid metal is set at 13mm. A central electrode made of stainless steel is isolated from the sidewall by a ceramic ring. The bottom side of the central electrode is connected to the anode of a DC power supply, and the side wall is connected to the cathode. A "water wheel" made of stainless steel is installed on the central electrode as an indicator for the motion of the liquid metal during plasma operation, as shown in Fig.6.5. The temperature is measured by a thermocouple attached to the bottom of the cup. The neutral deuterium gas pressure during plasma operation is typically ~0.1 Pa. The deuterium plasma parameters measured by a moveable Langmuir probe positioned in the immediate upstream of the mini-ACLMD setup are: the electron temperature is ~3eV and the plasma density is ~10^{10} cm^{-3}, whereby the ion bombarding flux is ~10^{16} $H^{+}/cm^{2}s$.

During the plasma experiments, visible spectroscopy measurements are performed, taking the intensity of Hα signal as the measurement of hydrogen recycling over the liquid metal mini-ACLMD setup. The line radiation intensities of Ga-I at 780.00 nm, In-I at 451.13nm and Sn-I at 380.0nm are monitored in parallel with the Hα intensity.

Shown in Fig. 6.6 is the ex-situ J x B setup put together with a pair of permanent magnets, providing a magnetic field of about 900 Gauss, and an LED rotation marker lamp attached on a rotatable "waterwheel" put in the liquid. The DC current is conducted through the liquid metal from the center electrode to the periphery of the cup made of SUS304 with a diameter of about 50 mm. For the ex-situ liquid rotation tests, the DC current is varied from 0 to 100 A, the rotation speed of which will later be presented. The in-situ J×B setup meant for plasma interaction experiments is essentially the same as the ex-situ setup, except that the permanent magnets are removed, instead of which the axial magnets of VEHCLE-1 are utilized to generate the J × B force for liquid convection. Also, the LED lamp is detached from the waterwheel to avoid any unwanted damage by plasma bombardment.

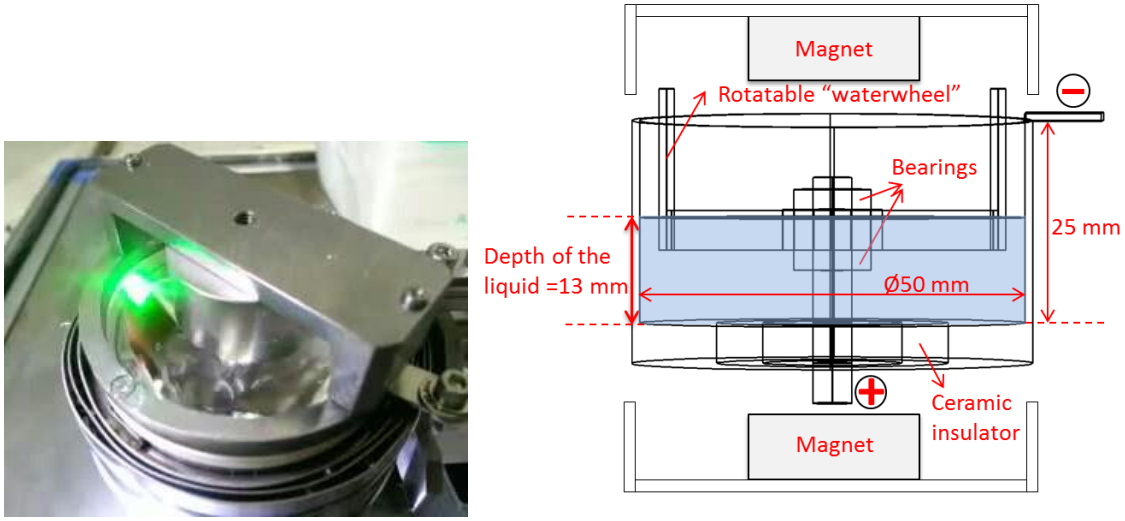

Figure 6.6 The ex-situ J x B liquid metal convection setup: (a) a photo with the LED marker on; and (b) a schematic drawing.

6.3. Simulation result

6.3.1 Liquid convection by Lorentz-force

By using the electrical conductivity $3.1\times10^{6}\Omega^{-1}m^{-1}$ for GaInSn [118], and $1.4\times10^{6}\Omega^{-1}m^{-1}$ for stainless steel, the current density in the liquid have been obtained by using a finite element analysis software COMSOL, as shown in Fig. 6.7, where the total DC current is 70A. And the current data are saved in the form of a vector $\mathbf{J}= [J_x, J_y, J_z]$.

The magnetic field at the liquid target position in VEHICLE-1 has been measured to be about 350 Gauss, i.e. B = [0, 0, -0.035] T. When the DC current is applied in the liquid, a J×B-force $\mathbf{F} = [F_x, F_y, F_z]$ is generated in the bulk of the liquid metal, as shown in Fig. 6.8, where

$$F_x = -J_y \times 0.035[\mathrm{T}],\ F_y = J_x \times 0.035[\mathrm{T}],\ F_z = 0 \qquad (6.2)$$

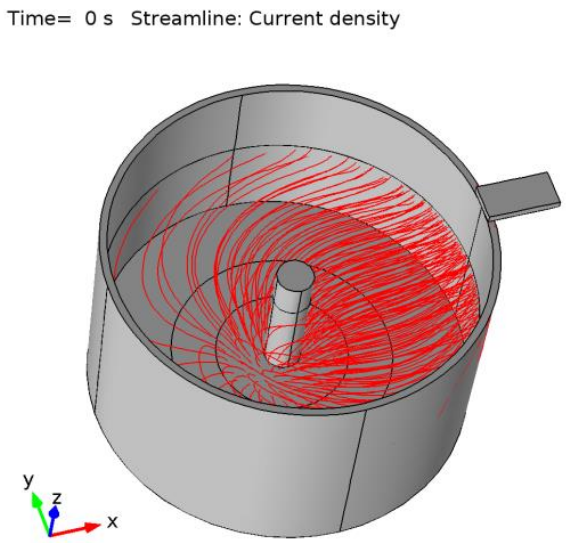

Figure 6.7 Current density in the liquid metal.

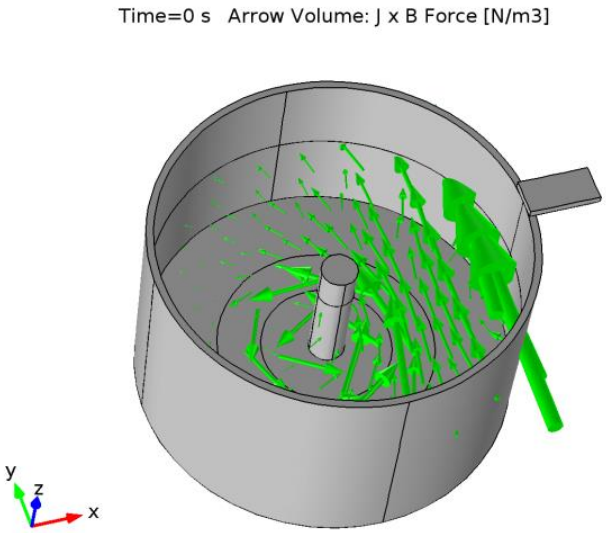

Figure 6.8 J×B force distribution in the liquid metal.

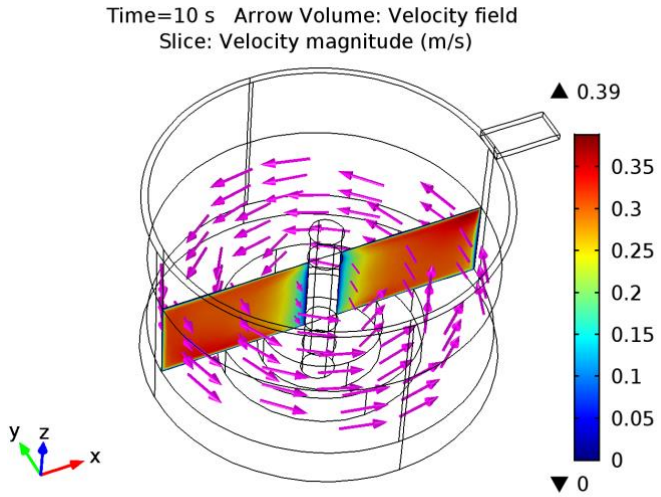

Figure 6.9 Velocity field of the liquid metal at time t=10s.

The convection motion of the liquid metal have been obtained by solving the Navier-Stokes equations with the CFD (Computational Fluid Dynamic) module, with the viscosity 2.98×10^{-7} m^2/s for GaInSn and the volume force $\mathbf{F} = [F_x, F_y, F_z]$. All the boundary conditions are set as no sliding wall, although the top surface is a free surface in the experiment. As a result, the velocity field vector $\mathbf{u} = [u_x, u_y, u_z]$ has been obtained, as shown in Fig.6.8, where the maximum velocity of the liquid is 0.39m/s, i.e. about 149 rad/min. This is higher than the rotation speed of ~100 rad/min, measured by the motion of the "water wheel'' in the liquid. The discrepancy may be ascribed to the flow resistance by the "water wheel'', which however is not considered in the simulation.

6.3.2 Current effects on deuterium transport

The deuterium transport behavior in the liquid metal has been simulated with the finite element analysis method by solving the basic mass balance Eq.(2.15), which is described in Chapter 2. The diffusivity of deuterium in liquid GaInSn is estimated to be $1\text{-}3\times10^{-4}$ cm^2/s at 489°C. Here, a constant diffusivity $D = 1\times10^{-4}$ cm^2/s is used for the calculation. And the time dependent velocity vector **u** is taken from the CFD module in Section 6.3.1. The boundary condition for the deuterium concentration at the top surface is normalized to be a constant $C_0 = 1$ mol/m^3, although it is a recombination limited

process at the front surface. The source term G is set as 0, and the initial concentration of the deuterium in the liquid is set as C = 0.

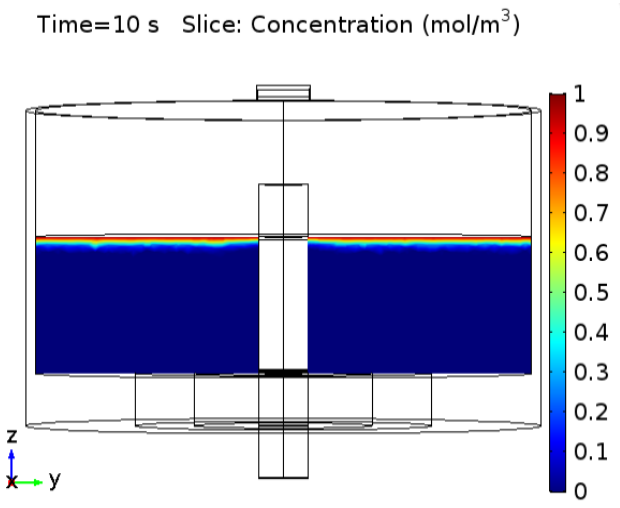

Figure 6.10 Deuterium concentration profile in the liquid metal at time t=10s with current J = 0A. (Diffusion only)

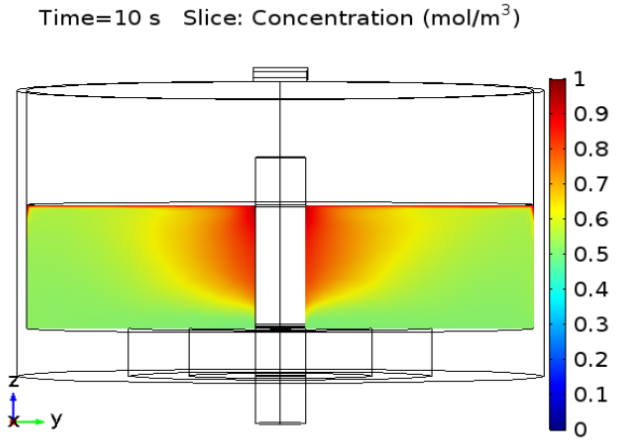

Figure 6.11 Deuterium concentration profile in the liquid metal at time t=10s with current J = 70A. (Diffusion + Convection)

Shown in Fig. 6.10 and Fig. 6.11 are the results on deuterium concentration profile on the center section at time t=10s. In Fig. 6.10, the current is J= 0 A, i.e. velocity vector **u**=0, where only diffusion dominates the deuterium transport. It is shown that deuterium transport to the zone only near the front surface within 10 seconds. And the diffusion distance could also be estimated by the equation d =$2\sqrt{Dt}$ = 0.63mm. For a comparison, the concentration profile with the current J= 70 A is shown is in Fig. 6.11. At time t=10s, deuterium atoms have already transported into the bottom of the liquid, where the depth is 13mm. It is found that the z component of the velocity $\mathbf{u}_z$ is downward in the center area at the velocity ramping up phase. As a result, deuterium transport downward is faster in the center, which makes the concentration of deuterium higher in the center at time t=10s.

Shown in Fig. 6.12 is a comparison of time evolution of total retained deuterium in the liquid metal at different currents. Shown in Fig. 6.13 is a comparison of the deuterium concentration profiles along the direction of the depth at time t=10s with different currents. It is found that the amount of deuterium retained in the liquid with convection (J=50A/ 70A/ 90A) is more than the amount in the case without convection (J = 0A). Also, more deuterium is retained in the liquid as the current increases.

Shown in Fig. 6.14 is a comparison of time evolution of the hydrogen recycling coefficient for different currents. Generally, for implanted deuterium atoms in a material, they will either be retained in the material, or release as molecules. The more deuterium being retained in the liquid would reduce the molecules being released from the liquid. It is found that hydrogen recycling is reduced during the transient phase when the JxB-forced convection is applied. And particle recycling is reduced more as the current increases.

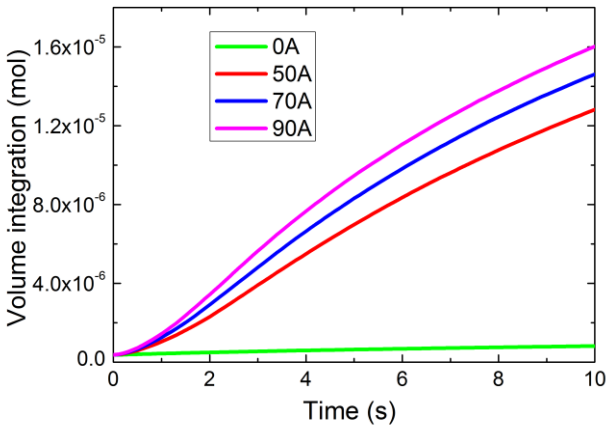

Figure 6.12 Time evolution of total retained deuterium in the liquid metal with different currents.

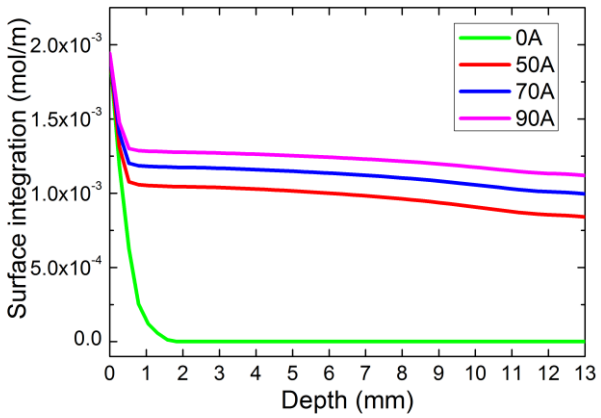

Figure 6.13 Deuterium concentration profiles along direction of depth at time t=10s with different currents.

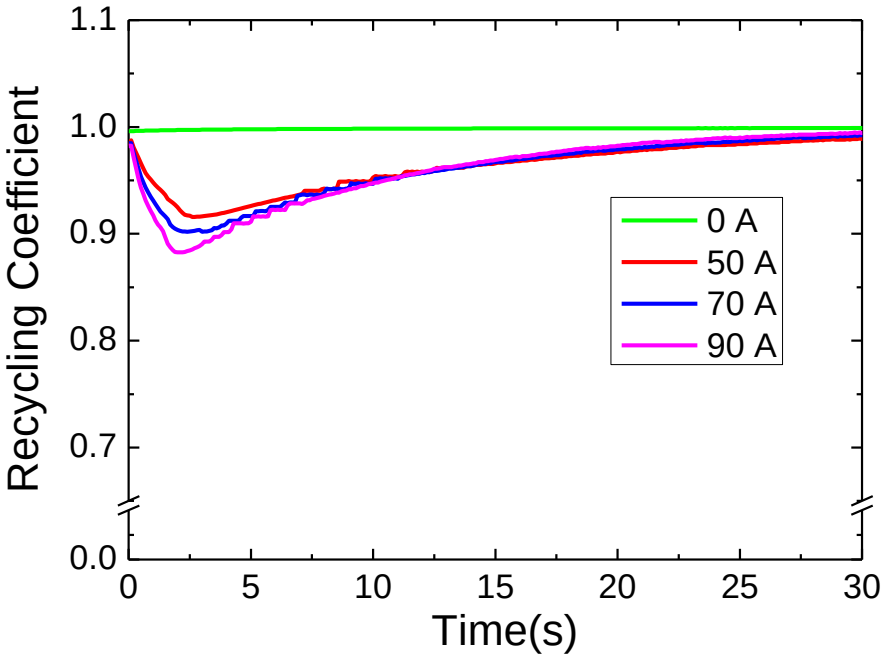

Figure 6.14 Time evolution of hydrogen recycling coefficient for different DC currents.

6.4. Experimental results and discussion

6.4.1 Ex-situ JxB liquid rotation tests

For the ex-situ setup, the rotation speed of the liquid metal has been measured while the DC current is varied. Although the liquid surface starts billowing at DC currents around 40 A, the actual liquid rotation indicated by the LED lamp has been observed only at DC currents larger than around 50 A, presumably due to the flow resistance by the waterwheel. The relation between the waterwheel rotation speed and the DC current is shown in Fig. 6.15. In our preliminary experiments, due to the limited capacity of the DC power supply, the waterwheel must be removed for the in-situ J x B setup for plasma interaction experiments to avoid the flow resistance described above. In the present work, the waterwheel is kept in the liquid metal, intended for more complete convection, even as it slows down the rotation speed for a given JxB force.

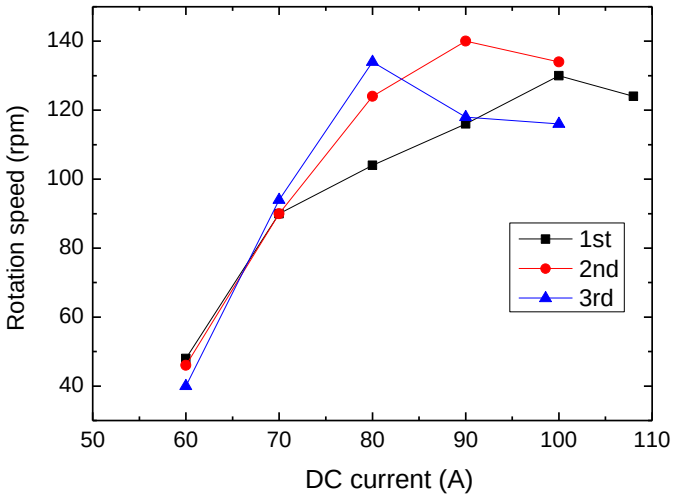

Figure 6.15 The relation between the JxB-forced rotation speed indicated by the LED lamp and the DC current through the liquid metal.

6.4.2. Particle recycling measurements for GaInSn

For particle recycling experiments, the liquid metal target has been bombarded with steady state hydrogen and deuterium plasmas. The magnetic field at the liquid target position in VEHICLE-1 has actually been measured to be about 350 Gauss. The initial temperature of the liquid metal is room temperature, typically ~30 °C. Shown in Fig. 6.16 (a) and (b) are the visible spectroscopy data taken for hydrogen and deuterium recycling measurements under plasma bombardment, respectively. For hydrogen recycling experiments, the application of JxB-forced convection has been repeated three times with a DC current of 65 A at an ion bombarding energy of 50 V, as indicated in Fig. 6.16 (a). Hydrogen recycling has been found to be reduced reproducibly by 5–10% while JxB forced convection applied. Similarly, as indicated in Fig. 6.16 (b), deuterium recycling from GaInSn has been observed to be reduced by 5–10% with the JxB-forced convection generated by a DC current of 60 A. As to the behavior of eutectic alloy constituents under hydrogen and deuterium plasma bombardment, no drastic change in line radiation intensity for Ga-I, In-I, and Sn-I has been observed with JxB-forced convection although the application of a DC-bias tends to increase these intensities.

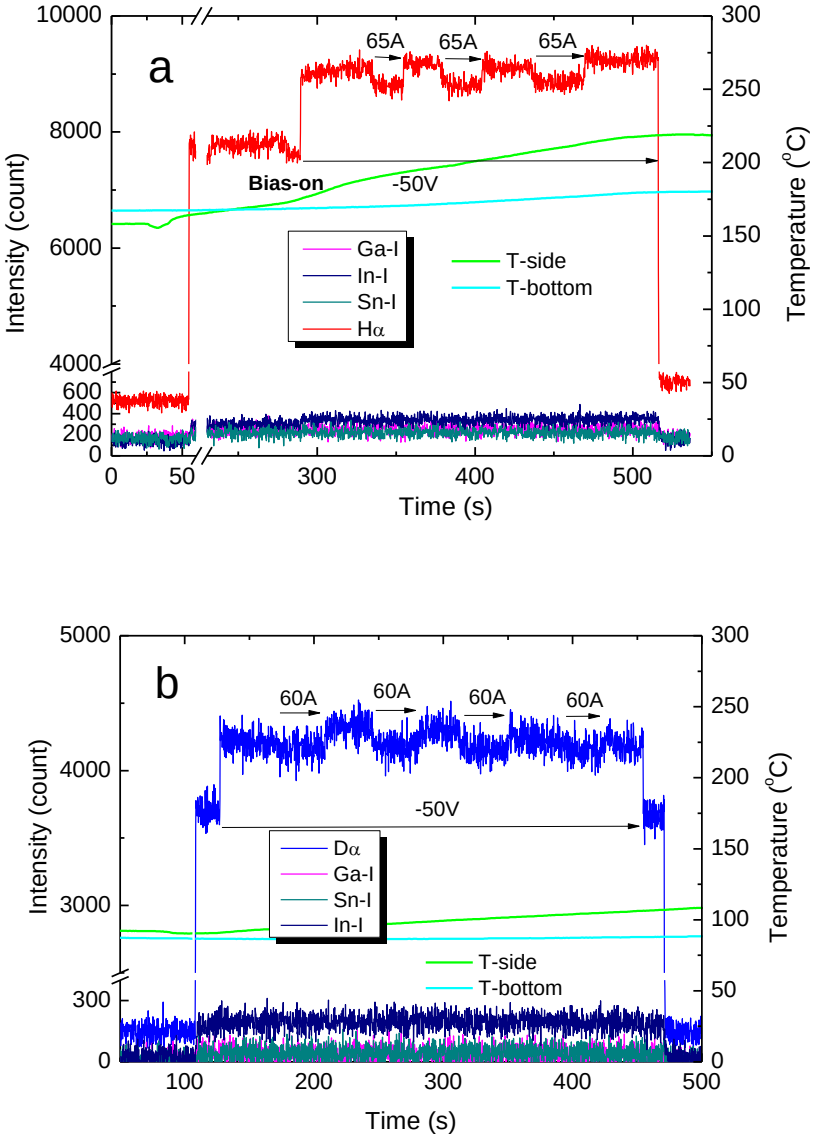

Figure 6.16 Hydrogen (a) and deuterium (b) recycling from a eutectic alloy liquid $Ga_{67}In_{20.5}Sn_{12.5}$ under steady state plasma bombardment with JxB-forced convection.

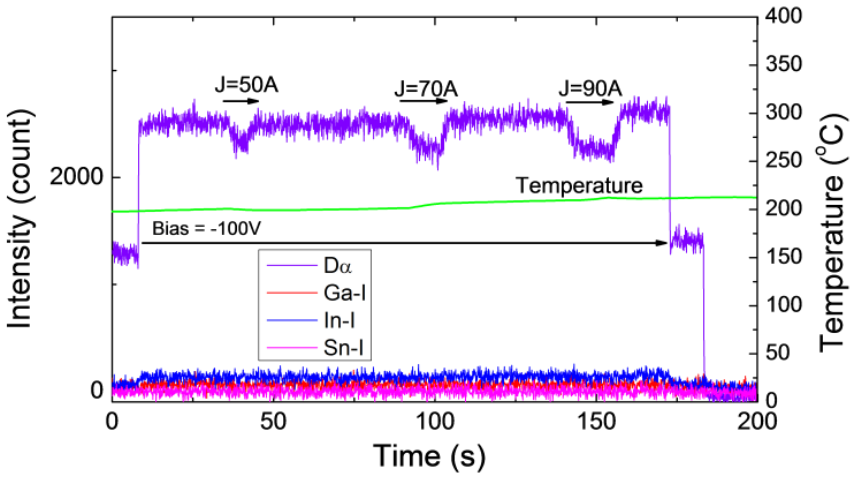

Figure 6.17 Current effects on deuterium recycling from J×B-force convected GaInSn

Shown in Fig.6.17 is the visible spectroscopy data taken for deuterium recycling measurements under plasma bombardment. In this experiment, the J×B-force convection effect on deuterium recycling has been observed with different currents. The total DC currents have been set at J = 50A, 70A, 90A. The duration time for 50A/70A/90A are 8s/10s/13s respectively. At t=8s, the intensity signal of Dα, i.e. deuterium recycling is reduced by ~7%, 10%, 12% relative to the quasi-steady state level, as shown in Fig. 6.17. The corresponding rotation speeds of the "water wheel" are found to be ~80rpm, ~100rpm, ~120rpm. This observation is consistent with the simulation result in Section 6.32.

Also observed is that the liquid temperature gradually increases during the course of these experiments, due to the Joule heating effect. Here, one would raise a question in what form hydrogen and deuterium are retained in GaInSn during the period recycling is reduced. It has been reported in the literature that gallium, indium and tin form their respective hydrides which tend to become thermally unstable to be decomposed even at relatively low temperatures [119-121]. To the best of our knowledge, there have been no reported data on the complex hydride formation with GaInSn. Nonetheless, it is possible that an alloy can form hydrides whereby its constituents form individual hydrides as known for those in the case of Ti-Zr-H [122]. One can also speculate that hydrogen and deuterium are retained in the liquid metal in microscopic bubbles, as

suggested in Ref. [123]. In addition to these possibilities, a hypothesis is proposed here that gas retention in GaInSn be limited to a certain level due to the saturation, perhaps related to the liquid temperature.

This leads us to predict that the Hα and Dα intensities would probably increase with increasing liquid temperature along with Joule heating. This hypothesis has been proven qualitatively, as illustrated in Fig.6.18. In this series of experiments, JxB-forced convection is applied three times for an elapsed time between 50 and 64 minutes, each about 5 minutes, at a DC current of 70 A while the ion bombardment energy is set at 150eV. Meanwhile the liquid temperature has increased by about 100^{o}C, measured by two thermocouples attached to the liquid cup: one on the side wall and the other on the bottom. As can be seen, the intensity of Dα decreases as soon as the JxB-force is applied, but gradually increases along with the increase in liquid temperature. Towards the end of measurements at an elapsed time of 64 minutes, deuterium recycling does not appear to be affected by JxB-forced convection, indicating a sign of saturation. After the saturation in the second set of measurements for an elapsed time between 65 and 70 minutes. In Fig.6.18, the intensity of Dα appears to remain constant or to increase rather than decrease, indicative of enhanced recycling, i.e. reemission, when the JxB-force is applied twice at the same DC current of 70 A as that for the earlier stage.

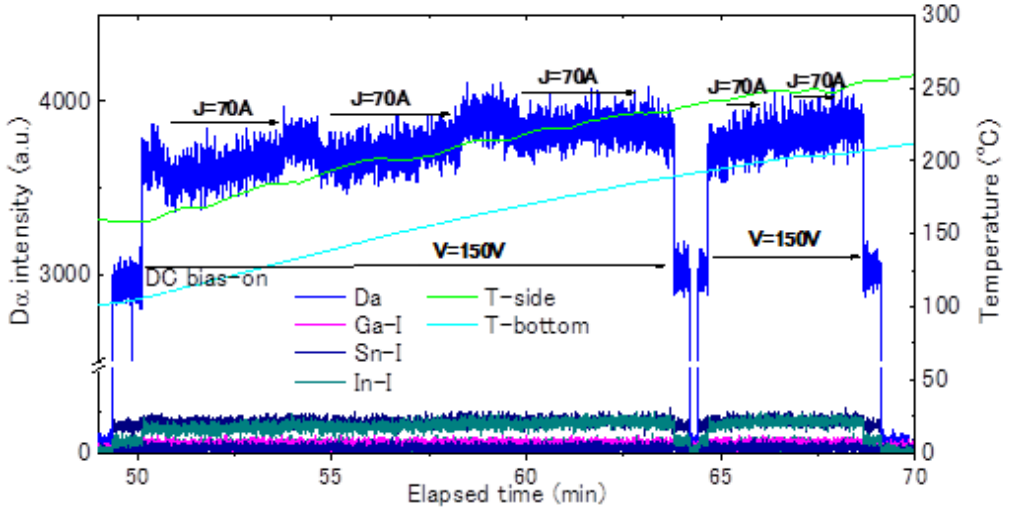

Figure 6.18 Joule heating effects on deuterium recycling from JxB-force convected $Ga_{67}In_{20.5}Sn_{12.5}$.

6.4.3. Surface analysis

Shown in Fig.6.19 (a) and (b) are the photos of $Ga_{67}In_{20.5}Sn_{12.5}$ before and after plasma exposure, respectively. Notice that there is a thin film floating over the liquid. In Table 6.1, the compositional analysis of this film indicates: 65.3wt% Ga, 23.4wt% In, 9.7wt% Sn, 0.8wt% C and 0.8wt% O, suggesting the formation of some chemical compounds in part during plasma bombardment but mostly during air exposure. Interestingly, even if they are formed, these surface films can readily be swept off by the rotating waterwheel as soon as the JxB-forced convection is applied, which has been seen during the ex-situ liquid rotation speed measurements described in Section 6.4.1. It is thus believed that there would be no significant effect of surface films on the observed behavior of particle recycling under plasma bombardment in VEHICLE-1.

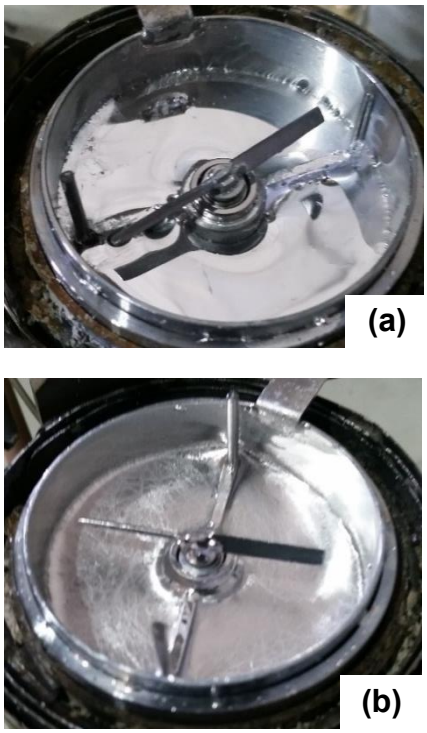

Table 6.1. The EDS analysis result of the composition

Element	w.t%			
	1	2	3	average
C	0.95	0.77	0.57	0.76
O	1.11	0.71	0.77	0.86
Ga	63.68	67.92	64.28	65.29
In	23.74	21.58	24.92	23.41
Sn	10.52	9.03	9.47	9.67

Figure 6.19 (a) The surface of liquid GaInSn before JxB-forced convection experiments. The Original compositions are 67% Ga, 20.5% In, and 12.5% Sn in w.t%.; (b) The surface of liquid GaInSn after JxB-forced convection experiments. EDS (Energy Dispersive Spectroscopy) is used for the elemental analysis.

6.5. Heat transfer in liquid metals under forced convection

To investigate the behavior of heat transfer in liquid metals under forced convection, a primary experiment is proposed. Shown in Figure 6.20 is the primary design of the experimental setup. A liquid GaInSn is set in a cup made of stainless steel. The depth of the liquid is 50mm and the diameter is 30mm. The top surface of the liquid can be heated by infrared introduced from a quartz tube, which is similar to the TDS facility shown in Figure 3.8. The heat power is ~1 MW/m^2. The temperatures of the liquid at the top and bottom are measured by two thermocouples, respectively. A horizontal direction magnetic field is generated by two external magnetic coils. Two electrodes are set in the middle of the liquid. It is expected that the liquid can be convected by the JxB force, when a proper a DC current is applied between the two electrodes.

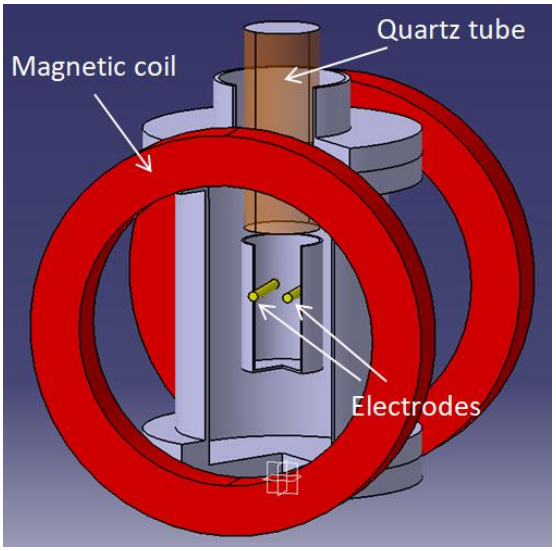

Figure 6.20 A primary design for the experiment on heat transfer in liquid metals under JxB-forced convection.

To predict the temperature profile in the liquid with and without forced convection. A 3-D model is established and the simulation work is conducted by using the COMSOL. The magnetic field is 0.035 T, and the total current is 70A. The way to get the velocity field of the liquid is same as the case described in Section 6.2. The first step is to get the current density distribution. The next step is to get the JxB force distribution. Then the convection motion of the liquid is obtained by solving the Navier-Stokes equations with the CFD (Computational Fluid Dynamic) module. Shown in Figure 6.21 is the simulation result on the velocity field **u**. It is found that it flows down between the electrodes and flows up along the edge. Taking the velocity field $\mathbf{u}\ [u_x, u_y, u_z]$ and the heat load Q=1 MW/m^2 on the top surface, the following equation of the heat transfer in a liquid is solved:

$$\rho C_p \frac{\partial T}{\partial t} + \rho C_p u \cdot \nabla T = \nabla \cdot (k \nabla T) + Q \tag{6.3}$$

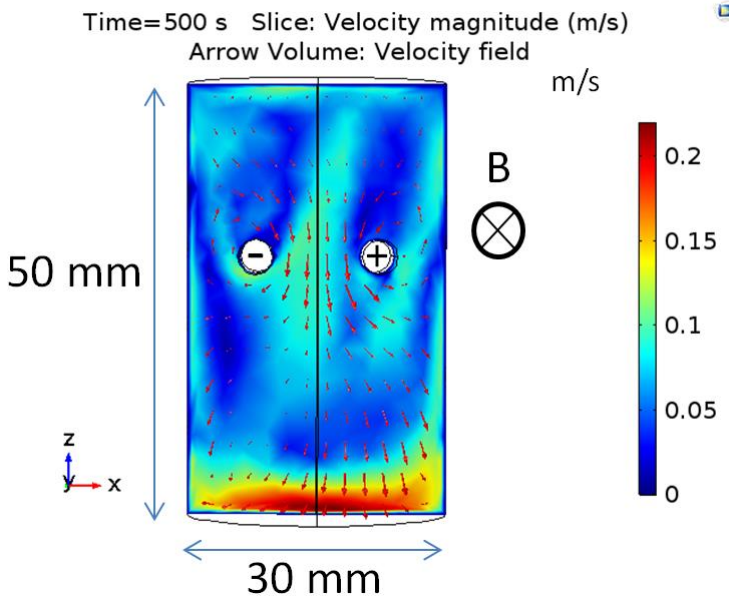

Figure 6.21 Velocity vector of the liquid under JxB- forced convection.

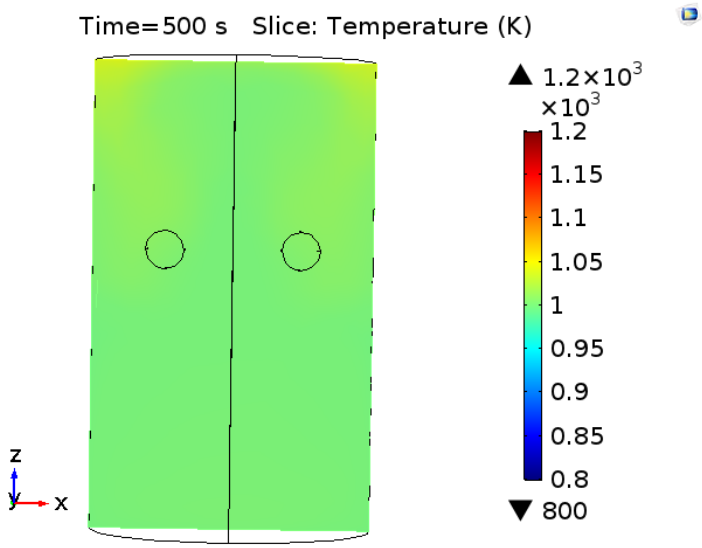

Figure 6.22 Temperature profile of the convected liquid at t=500s, with 1 MW/m^2 heat load on the top surface.

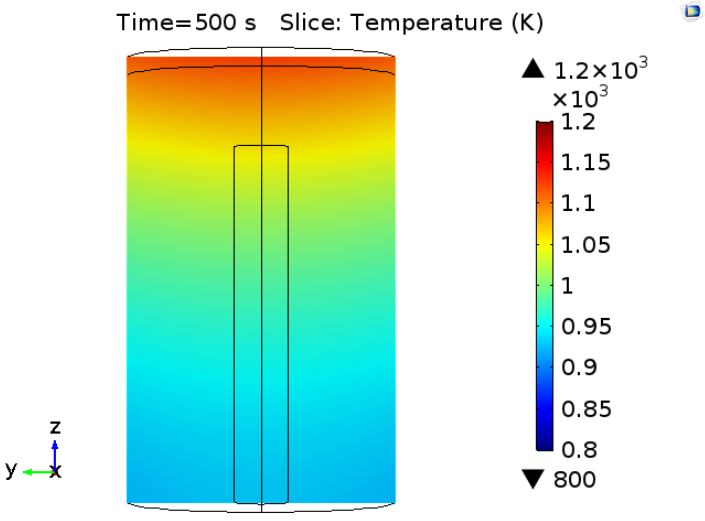

Figure 6.23 Temperature profile of the standing liquid at t=500s, with 1 MW/m^2 heat load on the top surface.

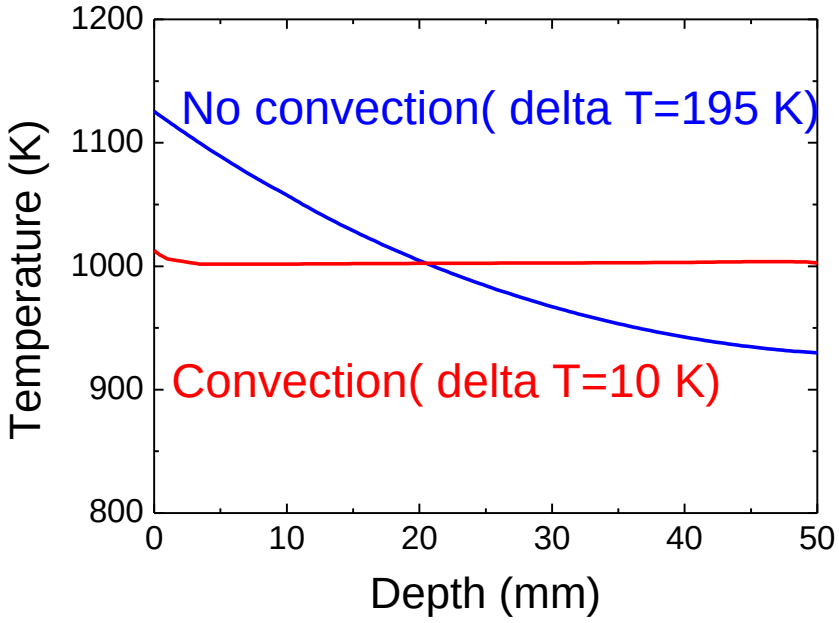

Figure 6.24 Temperature distributions in vertical direction with and without convection.

Shown in Fig.6.22 is the simulation result on the temperature profile of the convected liquid at t=500s. And the temperature distribution in the vertical direction is shown in Figure 6.24. It is found that the temperature profile in the liquid under convection is close to uniform, the temperature at the top is 1012K, while the temperature is 1002K at the bottom. For the case without convection, the velocity field **u**=0 is used in the simulation. Shown in Figrure 6.23 is the simulation result on the temperature profile of the standing liquid at t=500s. It is found that the temperature at the top is 1125K, while the temperature is 930K at the bottom.

The simulation results predict that the heat transfer in a liquid can be enhanced by JxB-forced convection. Due to the enhanced heat transfer, the surface temperature of the liquid can be reduced, which will advantageously to reduce the evaporation rate of the liquid metal. In the simulation, the top surface is set as a fixed sliding wall because little information is available on the surface behavior under the experimental conditions. So further study on the experimental work is necessary to demonstrate the simulation results.

6.6. Summary

A series of Proof-of-Principle experiments on the concept of an Actively Convected Liquid Metal Divertor has been conducted. Liquid convection motion by the JxB force has been realized under the condition of plasma bombardment. It has been found that deuterium recycling from the liquid is reduced, when forced convection is applied to the liquid. And particle recycling is reduced more as the current increases. Deuterium transport behavior in the liquid has been simulated by using a finite element analysis software. It is found that deuterium transport in the liquid is accelerated by convection, leading to more retained deuterium in the liquid before saturation.

A primary experiment on heat transfer in liquid under forced convection has been proposed and the simulation work has been conducted. It is found that the surface temperature of the liquid can be reduced due to the enhanced heat transfer by the JxB force. Further study with experimental work is necessary to demonstrate the simulation results.

Chapter 7 Summary and outlook

7.1. Summary

The application of liquid metals for plasma facing components has been proposed to resolve the technical issues related to power exhaust and particle handing in fusion reactors. The understanding of hydrogen isotopes properties in liquid metals is essential for studying particle control in the edge plasma. In this PhD thesis work, hydrogen isotopes transport behavior in liquid metals under steady state plasma bombardment has been studied.

An innovative method of holding a liquid metal on a mesh sheet by means of surface tension has been developed for plasma-driven permeation experiments. Hydrogen isotopes plasma-driven permeation through liquid metals, including lithium, GaInSn and gallium have been investigated by using a steady state laboratory-scale plasma device: VEHICLE-1. Hydrogen and deuterium PDP have been found to be recombination-limited for liquid lithium, and diffusion-limited for GaInSn, gallium and tin.

Hydrogen isotopes transport parameters such as the diffusivity and the recombination coefficient for lithium, GaInSn, gallium, tin and titanium have been measured. The temperature dependence of deuterium dynamic and static retention for gallium and tin have been evaluated. The hydrogen and deuterium transport parameter data taken for liquid lithium have been found to be in good agreement with the literature data, which validates the mesh-surface tension method.

Natural convection effects on deuterium permeation through a liquid metal have been investigated. Two cases of experiments on deuterium plasma-driven permeation through a liquid metal GaInSn have been conducted. One of the liquid samples is under natural convection, and the other one is standing. It has been found that deuterium permeation through the liquid is enhanced by the natural convection. And this behavior has been demonstrated by both analytical and simulation results.

A series of Proof-of-Principle experiments on the concept of an Actively Convected Liquid Metal Divertor have been conducted. Liquid convection motion by the JxB force has been realized under the conditions of plasma bombardment. It has been found that deuterium recycling from the liquid is reduced, when forced convection is

applied to the liquid. And this behavior is consistent with the simulation results by using a finite element solver. A primary experiment on heat transfer in liquid under forced convection has been proposed and the simulation work has shown that the surface temperature of the liquid can be reduced due to the enhanced heat transfer by the JxB force.

7.2. Outlook

This PhD thesis work has established some fundamental knowledge database for the applications of liquid metals as plasma facing components, which makes a contribution to magnetic fusion research in the field of fusion engineering. Using forced convection in the liquid to enhance the particle transport and heat transfer can be a possible idea for the engineering design.

Using the hydrogen transport parameters and the CFD solver, it is possible to calculate hydrogen isotopes dynamic retention in the liquid PFCs, and hydrogen isotopes recycling flux back to the edge plasma. More efforts are still required to investigate hydrogen isotopes transport behavior in liquid metals under reactor relevant conditions. Experimental proof of enhanced heat transfer by convection also warrants further investigation.

References

[1] J. A. Wesson, Tokamaks, Clarendon Press, Oxford, 3rd edition, 2004.

[2] M. Kikuchi, Frontiers in fusion research, Springer-Verlag, London, 2011.

[3] K. Miyamoto, Plasma physics and controlled nuclear fusion, Springer-Verlag, Berlin, 2005.

[4] J. D. Lawson, Some criteria for a power producing thermonuclear reactor. Proc. Phys. Soc. B 70 (1957) 6.

[5] http://www.efda.org/jet/.

[6] http://www-jt60.naka.jaea.go.jp/.

[7] http://www.lhd.nifs.ac.jp/.

[8] https://fusion.gat.com/global/DIII-D.

[9] http://www.ipp.mpg.de/16195/asdex.

[10] http://english.hf.cas.cn/ic/ip/east/.

[11] G.S. Lee et al.,Design and construction of the KSTAR tokamak, Nuclear Fusion 41 (2001)1515.

[12] K. Hanada et al., Steady-State Operation Scenario and the First Experimental Result on QUEST, Plasma Fusion Research 5 (2010) S1007.

[13] http://www.iter.org.

[14] Y. Shimomura, ITER towards the construction, Fusion Engineering and Design 74 (2005) 9.

[15] K. Tobita et al., Compact DEMO, SlimCS: design progress and issues, Nuclear Fusion 49 (2009) 075029.

[16] D. Maisonnier et al., DEMO and fusion power plant conceptual studies in Europe, Fusion Engineering and Design 81 (2006) 1123.

[17] F. Najmabadi et al., The ARIES-AT advanced tokamak, Advanced technology fusion power plant, Fusion Engineering and Design 80 (2006) 3.

[18] Sagara et al., Conceptual design activities and key issues on LHD-type reactor FFHR, Fusion Engineering and Design 81 (2006) 2703.

[19] Y. Wang et al., Overview of fusion energy science research in China, Paper presented at the 16th International Conference on Fusion Reactor Materials, Beijing, China, Oct. 20th -26th, 2013.

[20] Y. K. M. Peng et al.,Fusion Nuclear Science Facility (FNSF) Before Upgrade to Component Test Facility (CTF), Fusion Science and Technology 60 (2011) 441.

[21] S. Pfalzner, An introduction to inertial confinement fusion, Taylor & Francis, New York, 2006.

[22] https://lasers.llnl.gov.

[23] Hurricane et al., Fuel gain exceeding unity in an inertially confined fusion implosion, Nature 506 (2014) 343.

[24] P. C. Stangeby, The plasma boundary of magnetic fusion devices, Institute of Physics Publishing Bristol, 2000; Vol. 224.

[25] R.A. Pitts, Buring plasma diagnostics workshop, Varenna, Italy,24-28/09/2007

[26] R.A. Pitts et al. Status and Physics Basis of the ITER Divertor, Phys. Scr. T138, 014001 (2009).

[27] A. Loarte et al. MHD Stability of the ITER Pedestal and SOL Plasma and its Influence on the Heat Flux Width, Paper presented at PSI-conf. Kanazawa, May 26th-30th, 2014.

[28] S. TAMURA, K. TOKUNAGA, N. YOSHIDA, “High Heat Load Properties of High Purity CVD Tungsten”, Nucl. Mater. 307-311, 735 (2002).

[29] J. W. DAVIS V. R. BARABASH, A.MAKHANKOV, L. PLOCHL, K. T. SLATTERY, “Assessment of Tungsten for Use in the ITER Plasma Facing Components”, Nucl. Mater. 258-263, 308 (1998).

[30] S. TAMURA, K. TOKUNAGA, N. YOSHIDA et al. “Damage Process of High Purity Tungsten Coatings by Hydrogen Beam Heat Loads”, Nucl. Mater. 337-339, 1043 (2005).

[31] M. R. GILBERT and J. -Ch. SUBLET, “Neutron-Induced Transmutation Effects in W and W-alloys in a Fusion Environment”, Nucl. Fusion 51, 043005 (2011).

[32] J. D. STRACHAN, “Studies of Global Energy Confinement in TFTR Supershots”, Nucl. Fusion 34, 1017(1994).

[33] H.W. Kugel et al., The effect of lithium surface coatings on plasma performance in the National Spherical Torus Experiment, PHYSICS OF PLASMAS 15, 056118 (2008)

[34] G.Z. Zuo et al., Lithium coating for H-mode and high performance plasmas on EAST in ASIPP, J. Nucl. Mater. S90-S95, 438 (2013).

[35] B. BADGER, M. A. ABDOU, R. W. BOOM et al. "UWMAK-I A Wisconsin Toroidal Fusion Reactor Design", Univ. Wisconsin Rept. UWFDM-68 (1974).

[36] T. Iida, The physical properties of liquid metals, 1988

[37] Lyublinski I. E., A.V. Vertkov, and Evtikhin V. A., 2009 Plasma Devices and Operations 17 265

[38] Stangeby P. C., 2011 J. Nucl. Mater. 415 S278

[39] Badger B. et al 1974 UWMAK-I—A Wisconsin Toroidal Fusion Reactor Design' UWFDM-68, http://fti.neep.wisc.edu/pdf/fdm68.pdf

[40] Mirnov S.V. et al 1992 J. Nucl. Mater. 196–198 45

[41] Mirnov S.V. et al 2006 Fusion Eng. Des. 81 113

[42] M. A. ABDOU and the APEX TEAM, "On the Exploration of Innovative Concepts for Fusion Chamber Technology", Fusion Eng. Des. 54, 181 (2001).

[43] R.E. Nygren, Liquid surfaces for fusion plasma facing components—A critical review. Part I: Physics and PSI, Nuclear Materials and Energy 9 (2016) 6–21

[44] H. W. KUGEL, J. P. ALLAIN, M. G. BELL et al. "NSTX Plasma Operation with a Liquid Lithium Divertor", Fusion Eng. Des. 87 1724 (2012).

[45] J.S. Hu et al., First results of the use of a continuously flowing lithium limiter in high performance discharges, Nucl. Fusion 56 (2016) 046011 (14pp)

[46] Z.G. Zuo et al., Mitigation of plasma-material interactions via passive Li efflux from the surface of a flowing liquid lithium limiter in EAST, Nuclear Fusion, 57 (2017) 046017 (11pp)

[47] Jaworski M.A. et al 2010 Phys. Rev. Lett. 104 094503

[48] D. N. RUZIC, W. XU, D. ANDRUCZYK and M. A. JAWORSKI, "Lithium-Metal Infused Trenches (LiMIT) for Heat Removal in Fusion Devices", Nucl. Fusion 51, 102002 (2011).

[49] G. Z. ZUO, J. REN, J. S. HU, Z. SUN, Q. X. YANG et al. “Liquid Lithium Surface Control and its Effect on Plasma Performance in the HT-7 Tokamak”, Fusion Eng. Des. 89, 2845 (2014).

[50] Ren J. et al 2014 Phys. Scr.T 159 5

[51] Rion A. Causey, Hydrogen isotope retention and recycling in fusion reactor plasma-facing components, J. Nucl. Mater. 300 (2002) 91-117.

[52] H. Moriyama, K. Iwasaki, Y. Ito, J. Nucl. Mater. 191–194(1992) 190.

[53] E.E. Shpil’rain et al., High Temp. 3 (1965) 870.

[54] R.E. Buxbaum, E.F. Johnson, Ind. Eng. Chem. Fundam. 24 (1985) 180.

[55] R.M. Alire, J. Chem. Phys. 65 (1976) 1134.

[56] G.R. Longhurst et al., TMAP user’s manual, EFF-FSP 10315, Idaho National Engineering and Environmental Laboratory, 12 June 1992.

[57] S. Fukada et al, J. Nucl. Mater. 346 (2005)293–297.

[58] E.L. Cussler, Multicomponent Diffusion, Elsevier, New York, 1976 (p. 308).

[59] M. Hoch, J. Nucl. Mater. 120 (9184) 102.

[60] H. Katsuta, T. Ishigai, K. Furukawa, Nucl. Technol. 32 (1977) 297.

[61] E. Veleckis et al., J. Phys. Chem. 78 (1974) 1933.

[62] K. Iwase, Sci. Rep. Tohoku Univ., First Ser. 15 (1926)531.

[63] W.M. Mueller, J.P. Blackledge, G.G. Libowitz, Metal Hydrides, Academic Press, New York, 1968, p. 573.

[64] S.K. Erents, G.M. McCracken, P. Goldsmith, J. Phys. D (1971) 672.

[65] M.J. Baldwin, R.P. Doerner, et al., J. Nucl. Mater. 290–293 (2001) 166.

[66] B.Behrish and W. Eckstein, Physics of plasma-wall interaction in controlled fusion devices, Plenum Press, New York, 1986, p. 413–438.

[67] R.A. Langley et al., Data compendium for plasma-surface interactions, Nuclear Fusion 24 (1984) S9.

[68] Möller and J. Roth, Physics of Plasma-Wall Interaction in Controlled Fusion Devices, Plenum Press, New York, 1986, p. 439–494.

[69] M.T. Robinson and I. M. Torrens, Computer simulation of atomic-displacement cascades in solids in the binary-collision approximation, Physical Review, B9 (1974) 5008.

[70] W. Eckstein, IPP-Report, IPP 9/132, 2002.

[71] Y. Yamamura and Y. Mizuno, Low-energy sputterings with the Monte Carlo program ACAT, IIPJ-AM-40, Institute of Plasma Physics, Nagoya University, 1985.

[72] J. Kawata and K. Ohya, Ion backscattering and sputtering of plasma-irradiated carbon and tungsten surfaces in an oblique magnetic field, Japanese Journal of Applied Physics, 34 (1995) 6237.

[73] Haishan Zhou, A study on bi-direction hydrogen isotopes permeation through the first wall of a magnetic fusion power rector, PhD thesis, 2014.

[74] J. F. Ziegler et al., SRIM – The stopping and range of ions in matter (2010), Nuclear Instruments and Methods in Physics Research Section B, 268 (2010)1818.

[75] C.K. Gupta, Chemical metallurgy: principles and practice, Wiley-VCH, Weinheim, 2003.

[76] K. L. Wilson and M. I. Baskes, Deuterium trapping in irradiated 316 stainless steel, Journal of Nuclear Materials 76 & 77 (1978) 291.

[77] M.I. Baskes, A calculation of the surface recombination rate constant for hydrogen isotopes on metals, Journal of Nuclear Materials 92 (1980) 318.

[78] M. A. Pick and K. Sonnenberg, A model for atomic hydrogen-metal interactions - application to recycling, recombination and permeation, Journal of Nuclear Materials 131 (1985) 208.

[79] P. M. Richards, Surface-limited hydrogen release and uptake in metals, Journal of Nuclear Materials 152 (1988) 246.

[80] R.B. Bird, W.E. Stewart, and E.N. Lightfoot, Transport Phenomena, 2nd ed., John Wiley & Sons, 2005.

[81] J. Crank, The Mathematics of Diffusion, 2nd edition, Clarendon Press, Oxford, London, 1975.

[82] B. L. Doyle, A simple theory for maximum h inventory and release: A new transport parameter, Journal of Nuclear Materials 111&112 (1982) 628.

[83] D. K. Brice and B.L. Doyle, Steady state hydrogen transport in solids exposed to fusion reactor plasmas: part I: Theory, Journal of Nuclear Materials 120 (1984) 230.

[84] D. K. Brice, Steady state hydrogen transport in solids exposed to fusion reactor plasmas, part III: Isotope effects, Journal of Nuclear Materials 122&123 (1984) 1531.

[85] M. I. Baskes, DIFFUSE83, Sandia Report SAND83-8231.

[86] G.R. Longhurst, TMAP7: tritium migration analysis program, user manual, Idaho National Laboratory, INEEL/EXT-04-02352, 2004.

[87] Y. Hirooka et al., A new versatile facility: Vehicle-1 for innovative PFC concepts evaluation and its first experiments on hydrogen recycling from solid and liquid lithium, Journal of Nuclear Materials 337-339 (2005) 585.

[88] MICHAEL A. LIEBERMAN et al., Principles of plasma discharges and materials processing, second edition, 2005

[89] Lieberman, M. A., and R. A. Gottscho (1994), in Physics of Thin Films, Vol. 18

[90] R. L. Merlino, Understanding Langmuir probe current-voltage characteristics, American Journal of Physics 75 (2007) 1078-1085.

[91] F. F. Chen In Langmuir probe diagnostics, IEEE-ICOPS Meeting, Jeju, Korea, 2003.

[92] L. Conde, An introduction to Langmuir probe diagnostics of plasmas, Madrid: Dept. Física. ETSI Aeronáut ngenieros Aeronáuticos Universidad Politécnica de Madrid (2011) 1-28.

[93] Manual of quadrupole mass spectrometer, https://www.pfeiffer-vacuum.com

[94] L.C. Johnson et al., IONIZATION, RECOMBINATION, AND POPULATION OF EXCITED LEVELS IN HYDROGEN PLASMAS, J. Quonr. Specwosc. Radar. Transfer. Vol. 13, pp. 333-358

[95] Y. Hirooka, H. Fukushima, N. Ohno, S. Takamura, Proof-of-principle experiments on the concept of moving-surface plasma-facing components—hydrogen recycling over a titanium-gettered rotating drum, Fusion Engineering and Design 65 (2003) 413-421.

[96] P.A. Redhead, Thermal Desorption of Gases, Vacuum 12, 203 (1962).

[97] R. K. Janev et al., Elementary Processes in Hydrogen–Helium Plasmas, Springer-Verlag, Berlin Heidelberg (1987).

[98] H. Bi, Y. Hirooka, J. Yagi, Y. Xu, A study on hydrogen isotopes transport in a liquid metal GaInSn by plasma-driven permeation method, Nuclear Materials and Energy, 2017, in press.

[99] W.H. Cubberly, Metals Handbook, vol.2, 9th ed. (Metals Park, 1979).

[100] Y. Plevachuk et al., J. Chem. Eng. Data 59, 757 (2014).

[101] D. L. Johnson and H. G. Nelson: Met. Trans,, 1973, vol. 4, pp. 569-73.

[102] K. K. Shah and D. L. Johnson: Hydrogen in Metals, 1st ed., vol. 2, pp. 475-81,American Society for Metals, Cleveland, Ohio, 1974.

[103] I. Prigogine. Introduction to Thermodynamics of Irreversible Processes, 2nd ed. (Wiley. New York. 1961) Chaps. 1. 5 and 6.

[104] Y. Hirooka et al., J. Nucl. Mater. 135, 82 (1985).

[105] Y. Hirooka. Vacuum Sci. Technol. A2 (1984) 16.

[106] A. San-Martin et al., The H-Ti (Hydrogen-Titanium) System, Bulletin of Alloy Phase Diagrams Vol. 8 No. 1 1987

[107] H.U. Borgstedt et al., J. Phys. Chem. Ref. Data 30, No.4, 846 (2001).

[108] M.J. Baldwin et al., J. Nucl.Mater. 306, 15 (2002).

[109] X. Liu et al., First-principles molecular dynamics study of deuterium diffusion in liquid tin, Condensed Matter, July 27, 2017

[110] A.V. Getling, Rayleigh-Bénard Convection: Structures and Dynamics (World Scientific). (1998). ISBN 9810226578

[111] K. K. Tan et al., The onset of convection driven by buoyancy effects caused by various modes of transient heat conduction: Part I. Transient Rayleigh numbers, Chemical Engineering Science 54 (1999) 225-238

[112] D. S. Evans, A. Prince, Thermal analysis of Ga-In-Sn system, Metal science, Volume 12, Issue 9, 1978

[113] M. Flori, Using boussinesq approximation for CFD modeling of natural convection around a horizontal cylinder, ANNALS of Faculty Engineering Hunedoara, 2014(51)

[114] Scott A. Socolofsky & Gerhard H. Jirka, Special Topics in Mixing and Transport Processes in the Environment, 5th Edition, 2005

[115] H. Bi, Y. Hirooka, A study on hydrogen isotopes transport in a liquid metal GaInSn by plasma-driven permeation method, Nuclear Materials and Energy, 2017, https://doi.org/10.1016/j.nme.2017.02.004

[116] M. Shimada, Y. Hirooka, Actively convected liquid metal divertor, Nuclear Fusion 54 (2014) 122002(7pp).

[117] Tobita K. et al 2009 Nucl. Fusion 49 075029

[118] Yuriy Plevachuk, Vasyl Sklyarchuk, Thermophysical properties of the liquid Ga-In-Sn eutectic alloy, J. Chem. Eng. Data 2014, 59, 757-763

[119] A.J. Daons , M.J. Goode , C.R. Pulham , Gallane at Last! Synthesis and properties of binary gallium hydride, J. Am. Chem. Soc. 111 (1989) 1936–1937 .

[120] K. Inoue , A. Sawada , I. Shibata , A. Baba , Indium hydride: a novel radical initiator in the reduction of organic halides with tributyltin hydride, Tetrahedron Lett. 42 (2001) 4661–4663 .

[121] K. Tamaru , The thermal decomposition of tin hydride, J. Phys. Chem. 60 (1956) 610–612 .

[122] S.K. Dolukhanyan , et al. , Specifics of the formation of alloys and their hydrides in Ti-Zr-H system, Rus. J. Phy. Chem. B1 (2007) 563–569 .

[123] C. Liao , M.S. Kasimi , J.E. Meyer , On hydrogen transport and edge plasma modeling of liquid-metal divertors, Fusion Technol. 23 (1993) 208–217 .

List of publications:

[1] **H. Bi**, Y. Hirooka, J. Yagi, *A Study on Hydrogen Transport in Liquid Metals under Steady State Plasma Bombardment*, Plasma and Fusion Research, 11(2016)2405026.

[2] **H. Bi**, Y. Hirooka, J. Yagi, Y. Xu, *A study on hydrogen isotopes transport in a liquid metal GaInSn by plasma-driven permeation method*, Nuclear Materials and Energy, 2017, in press.

[3] **H. Bi**, Y. Hirooka, *Deuterium transport in a Lorentz-force convected liquid metal GaInSn under steady state plasma bombardment*, Fusion Engineering and Design, 2017, in press.

[4] **H. Bi**, Y. Hirooka, *Deuterium transport in a liquid metal GaInSn with natural convection under steady state plasma bombardment*, Fusion Engineering and Design, 2017, in press.

[5] **H. Bi**, Y. Hirooka, *Deuterium transport and retention in liquid Ga and Li under steady state plasma bombardment*, IEEE Transactions on Plasma Science, July 2017, under review.

[6] Y. Hirooka, **H. Bi**, M. Shimada, M.Ono, *Hydrogen and helium recycling from a JxB-force convected liquid metal $Ga_{67}In_{20.5}Sn_{12.5}$ under steady state plasma bombardment*, Fusion Engineering and Design, 117(2017)140-144

[7] Y. Hirooka, **H. Bi**, M. Shimada, M.Ono, *Steady state hydrogen, deuterium, helium and argon plasma interactions with a liquid metal: $Ga_{67}In_{20.5}Sn_{12.5}$ convected by Lorentz force*, Nuclear Materials and Energy, 2017, in press.